Photodoping of Colloidal Nanocrystals

Alicia W Cohn

A dissertation submitted in partial fulfillment of the
requirements for the degree of

Doctor of Philosophy

University of Washington
2014

Reading Committee:
Daniel Gamelin, Chair
James Mayer
Munira Khalil
Xiaosong Li

Program Authorized to Offer Degree:
Chemistry

University of Washington

Abstract

Photodoping of Colloidal Nanocrystals

Alicia W. Cohn

Chair of Supervisory Committee:
Professor Daniel R. Gamelin
Department of Chemistry

This dissertation addresses various aspects of photodoping colloidal nanocrystals. Photodoped ZnO nanocrystals were found to be versatile tuneable reducers using both quantum confinement and band-gap engineering with Mg^{2+} doping to change the conduction band potential. Using photoluminescence of the visible trap and magnetic circular dichroism spectroscopy of Mg^{2+} and Mn^{2+} co-doped ZnO, Mg^{2+} was shown to change the potential of both the conduction and valence band in a ratio of 0.68:0.32. The hole scavenging reaction using ethanol as the hole scavenger was investigated using continuous-wave and time resolved photoluminescence of the visible trap state of ZnO. The reaction was found to occur between the valence band hole and with a rate of > 15 ps^{-1}. Quenching of the ZnO visible trap luminescence upon photodoping was shown to be due to trap/electron Auger process while the concomitant enhancement of the UV band-gap emission was hypothesized to be due to a reduction in non-radiative processes due to extra electrons in the conduction-band. The trap/electron Auger process in ZnO nanocrystals was further characterized by a size-dependence and shown to scale

with R^2. Another previously unknown Auger size dependence was measured in CdSe/ZnS trions and shown to scale with $R^{4.3}$.

Table of Contents

List of Figures iii

List of Schemes iv

List of Abbreviations v

Chapter 1: *n*-Type Quantum Dots and Auger Processes 1

1.1 Introduction 1

1.2 Photodoping of ZnO and Other Semiconductor Nanocrystals 3

1.3 Auger Processes in Semiconductors 7

1.4 Summary 12

1.5 Notes to Chapter 1 13

Chapter 2: Mg^{2+} Doped in ZnO for Tunable Photdoped Electrons 16

2.1 Introduction 16

2.2 Experimental 18

2.2.A Synthesis 18

2.2.B Physical measurements 18

2.3 Results and Analysis 20

2.3.A Nanocrystal characterization 20

2.3.B Spectroscopic properties 21

2.3.C Charged $Zn_{1-x}Mg_xO$ nanocrystals 26

2.3.D Electron-transfer reactivity 28

2.4 Conclusion 30

2.5 Notes to Chapter 2 31

Chapter 3: Photodoping ZnO Nanocrystals: Picosecond Hole Capture, Electron Accumulation and Auger Recombination 34

3.1 Introduction 34

3.2 Experimental 36

3.2.A Synthesis and photochemical charging 36

3.2.B Physical measurements 37

3.3 Results and Analysis 38

3.3.A Nanocrystal charging under anaerobic conditions 38

3.3.B Photooxidation of ethanol under aerobic conditions 42

3.3.B.*i* CW photoluminescence 43

3.3.B.*ii* Time-resolved photoluminescence.......... 45
3.3.C Auger de-excitation.......... 48
3.4 Discussion.......... 52
3.4.A Hole scavenging by EtOH and electron accumulation.......... 52
3.4.B Auger processes and the changes in visible and UV photoluminescence with charging.......... 54
3.5 Conclusion.......... 57
3.6 Notes to Chapter 3.......... 58
Chapter 4: Size-Dependent Trap-Assisted Auger Recombination in ZnO Nanocrystals.......... 61
4.1 Introduction.......... 61
4.2 Experimental.......... 62
4.2.A Synthesis.......... 62
4.2.B Physical Measurements.......... 62
4.3 Results and Discussion.......... 62
4.4 Conclusion.......... 74
4.5 Notes to Chapter 4.......... 75
Chapter 5: Size Dependence of Negative Trion Auger Recombination in Photodoped CdSe Nanocrystals.......... 77
5.1 Introduction.......... 77
5.2 Experimental.......... 79
4.2.A Synthesis.......... 79
4.2.B Physical methods and photodoping.......... 79
5.3 Results and Discussion.......... 80
5.4 Conclusion.......... 92
5.1 Notes to Chapter 5.......... 92
Chapter 6: Summary and Outlook.......... 95
6.1 Summary.......... 95
6.2 Outlook.......... 96
6.3 Notes to Chapter 6.......... 98
Bibliography.......... 99

List of Figures

Figure 1.1. Absorption of neutral and charged ZnO nanocrystals 4

Figure 1.2. Absorption of neutral and charged CdSe nanocrystals 7

Figure 1.3. Calculated trion Auger rates versus confinement width 11

Figure 2.1 Powder XRD and TEM of Mg^{2+} doped and undoped ZnO 21

Figure 2.2 Absorption and visible PL spectra of various Mg^{2+} concentration in ZnO 22

Figure 2.3 Peak energy of visible trap PL versus band-gap energy for ZnO and $Zn_{1-x}Mg_xO$ 24

Figure 2.4 Room temp. 1 T MCD spectra of $Zn_{0.98-x}Mg_xMn_{0.02}O$ ($x = 0, 0.05, 0.10\ (\pm 0.01)$) and plot of ΔE_{CB} vs ΔE_g from the MCD 26

Figure 2.5 EPR spectra of colloidal *n*-type $Zn_{1-x}Mg_xO$ ($x = 0.05, 0.10, 0.13,$ and 0.17) nanocrystals and plot of g-value versus E_g 27

Figure 2.6 EPR spectra showing electron transfer from ZnO to $Zn_{0.75}Mg_{0.25}O$ nanocrystals 30

Figure 3.1 CW PL and EPR spectra of ZnO nanocrystals at various charging levels, TEM 39

Figure 3.2 TR PL decays of visible trap emission before and after charging 41

Figure 3.3 TR PL decays of UV band-edge emission at various charging levels 42

Figure 3.4 CW PL spectra of visible trap emission as a function of added EtOH 44

Figure 3.5 TR PL decays of visible trap emission as a function of added EtOH 46

Figure 3.6 Picosecond timescale TR PL decays of visible trap emission as a function of added EtOH..... 47

Figure 3.7 TR PL decays of visible trap and UV emission for a stirred and not stirred cuvette 49

Figure 3.8 Power dependence visible trap emission TR PL decays 51

Figure 4.1 CW PL spectra and TR PL decays of ZnO in air and airfree 66

Figure 4.2 Size dependent TR PL decays of trap Auger process and Auger lifetime versus nanocrystal radius 67

Figure 4.3 Plot of Auger lifetime versus nanocrystal radius for ZnO trap-assisted , CdSe trion, and CdSe biexciton recombination 69

Figure 4.4 Transient absorption and TR PL decays of ZnO nanocrystals 72

Figure 5.1 Absorption and CW PL of CdSe and CdSe/ZnS nanocrystals 81

Figure 5.2 Absorption and TR PL decays of CdSe/ZnS as prepared, photodoped, re-oxidized 83

Figure 5.3 Size dependent TR PL decays of photodoped CdSe/ZnS nanocrystals and plot of trion Auger lifetime versus nanocrystal radius 87

Figure 5.4 Plot of CdSe Auger lifetimes versus nanocrystal radius for negative trions, biexcitons, and calculated positive trions 89

List of Schemes

Scheme 1.1. Methods for electronic doping of nanocrystals 2

Scheme 1.2. Common Auger recombination processes 8

Scheme 3.1. Hole quenching and trapping in ZnO nanocrystals 54

Scheme 3.2. Mechanisms for suppression of k_{trap} upon charging 57

Scheme 4.1. Auger processes for exciton/ electron-hole trap combination 73

List of Abbreviations

AZO	Al^{3+} doped ZnO
CW	continuous wave
CB	conduction band
D	diameter
d	diameter
DPPH	2,2-diphenyl-1-picrylhydrazyl radical
EPR	electron paramagnetic resonance
EtOH	ethanol
H^+	proton
ICP-MS/AES	inductively coupled plasma – mass spectrometry/atomic emission spectroscopy
IR	infrared
LED	light emitting diode
MCD	magnetic circular dichroism
$ML_{CB}CT$	metal to ligand charge transfer
Na[biphen]	sodium biphenyl
NC	nanocrystal
PL	photoluminescence
PLD	pulsed laser deposition
QD	quantum dot
R	radius
TA	transient absorption
TEM	transmission electron microscopy
TR	time resolved
UV	ultraviolet
$V_O^{\bullet}$	oxygen vacancy
VB	valence band
XPS	X-ray photoelectron spectroscopy
XRD	X-ray diffraction

ACKNOWLEDGEMENTS

I would like to thank those who helped and supported me during my graduate career. I would like to especially thank my advisor Daniel Gamelin for his encouragement and mentorship. This would not have been possible without the additional support of all of the chemistry department staff. Last but not least, I would like to thank all past and present Gamelin group members for being at least the one reason why I look forward to going into work.

Prof. Daniel R. Gamelin
Prof. Victor Z. Polinger
Dr. Pradip Chakraborth
Dr. Kathryn Knowles
Dr. Jeffrey Rinehart
Dr. Emily McLaurin
Dr. Jillian Dempsey
Dr. Stefan Ochsenbein
Dr. Nils Janßen
Dr. Kevin Kittilstved
Dr. Jianwei Sun
Dr. Diane K. Zhong
Dr. Michael White
Dr. Claire A. Johnson
Dr. Kelly Whitaker
Liam Bradshaw
Alina Schimpf
Vlad Vlaskin
Amanda Weaver
Charlie Barrows
Mike Carroll
Kimberly Hartsein
Heidi Nelson
Patrick Whitham
Katherine Bryant
Ashley Bissell
Curtis Deer
Troy Kilburn
Brigit Miller
Michael DeSiena

Chapter 1: *n*-Type Quantum Dots and Auger Processes

1.1 Introduction

The ability to study electronically doped quantum dots is important to many emerging areas of quantum dot (QD) technology. Electronic doping of QDs (also called “charging”) consists of adding additional charge carriers (electrons or holes) to the conduction or valence band respectively so that they are considered delocalized throughout the QD. Increased carrier density can hinder device performance in many areas by causing, for example, efficiency droop in QD-LEDs[1-3] and decreased charge injection efficiency in QD sensitized solar cells.[4,5] Alternatively, new properties that emerge in electronically doped QDs can enhance the function of QDs for quantum computing[6,7], tunable chemical reactivity[8], controlling magnetism[9] and boosting the voltage of absorbed photons in a solar cell.[10]

There are four different general strategies to add extra charge carriers to QDs: (*i*) aliovalently, (*ii*) chemically, (*iii*) electrochemically, and (*iv*) through photodoping. Scheme 1.1 illustrates these processes for addition of extra electrons (*n*-type doping), which is the primary focus of this thesis. Aliovalent doping adds charge carriers to the nanocrystal by substituting a lattice site with a dopant of different oxidation state. This charge imbalance introduces an additional electron or hole to achieve overall neutrality. For example, Al^{3+} doped ZnO (AZO) gains conduction band electrons to balance the excess positive charge resulting from Al^{3+} ions substituting for Zn^{2+} ions.[11,12] Removing an ion from the lattice (i.e. creating a vacancy) can produce the same effect as aliovalent doping.[13] Often, *n*-type nanocrystals lose their excess electrons to air oxidation however, AZO nanocrystals and other aliovalently doped nanocrystals are often air-stable.[14-16] Unfortunately, this method of electronic doping is hampered by the tendency of the compensating charge to be localized near the dopant instead of delocalized throughout the nanocrystal.[14] A second method for introducing *p*- or *n*-type character to a quantum dot is through chemical charging. This method adds charge carriers to the QD through the addition of a chemical agent that has a redox potential such that electrons or holes will be transferred spontaneously to the QD. Decamethylcobaltocene is a popular one electron reductant that has been used to chemically charge PbS, PbSe,[17] and ZnO.[18] A third method, electrochemical charging, involves anchoring QDs to a conducting substrate and applying a potential in order to flow electrons or holes through the substrate into the conduction or valence band, respectively, of the QDs.[19-21] A final standard method, photodoping uses photoexcitation to create an electron-hole pair (exciton) in a QD in the presence of a hole scavenger that reduces the hole before the exciton recombines and, consequently leaves the electron stranded in the conduction band. Presently, photodoping has only been employed to introduce extra electrons and not holes.[22] Photodoping is the primary method used to create the *n*-type ZnO and CdSe nanocrystals discussed in this thesis.

Scheme 1.1

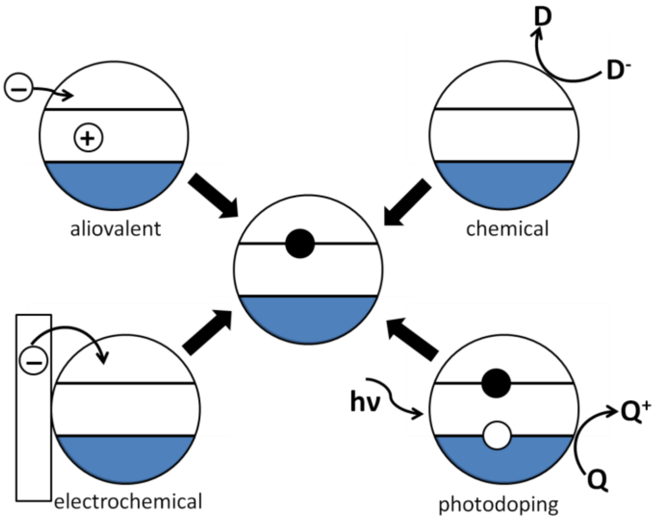

1.2 Photodoping ZnO and Other Semiconductor Nanocrystals

ZnO was first studied in the quantum confinement size regime as a transparent sol by Koch, *et al* in 1985.[23] They observed a decrease in the intensity of both the band-gap absorption at ~ 360 nm and the trap emission at ~ 540 nm when they exposed the ZnO sol to 330 nm light from a xenon arc lamp for 1 min. Koch, *et al.* attributed these observations to a dissolution and reformation of the ZnO nanoparticles, but Bahnemann, *et al*. later proposed that the bleaching of the band-gap absorption and quenching of the trap emission under UV irradiation was due to the presence of extra electrons in the conduction band of ZnO.[24] Both groups prepared and characterized the ZnO nanoparticles as a colloidal suspension in 2-propanol, which can reduce the hole in the valence band of ZnO formed upon excitation with UV light leaving the electron in the conduction band, where it is stable indefinitely under anaerobic conditions. Exposure to air, causes the removal of the electrons from the conduction band of ZnO via oxidation, which enables the entire process to be completely reversible. This work by Koch, *et al.* and Bahnemann, *et al.* is thus one of the first demonstrations of nanocrystal photodoping and was referred to at the time as “electron storage.”[24]

Since these first papers demonstrating photodoping, electrons have been added to ZnO nanoparticles electrons both electrochemically and chemically as well.[25-27] A bleach of the band gap transition, as observed by Koch, *et al.*, is one signature of electron accumulation in the conduction band. The appearance of intraband transitions of the conduction band electrons in the in the absorption spectrum (typically in the infrared [IR] region) is further evidence of electron accumulation in the conduction band of ZnO or other semiconductor nanocrystals (Figure 1.1). Shim, *et al*. first observed these transitions in *n*-type ZnO and CdSe nanocrystals by injecting electrons chemically using sodium biphenyl as a reducing agent.[27] Since this initial work, the electron intraband transitions in ZnO have also been observed in photochemically, aliovalently and electrochemically charged QDs.[11,25,26,28] Lastly, the presence of unpaired electrons in the conduction band of an *n*-doped semiconductor QD can be confirmed by electron paramagnetic resonance (EPR) spectroscopy.[28] The delocalized nature of the electrons in these systems is evident by the dependence of the electron g-value on the QD radius.[29] In addition, the integrated intensity of the EPR signal scales, although not linearly, with the number of conduction band electrons.[30] The trend of increasing EPR intensity with increasing number of electrons can be modeled using a Poissonian shell filling scheme for the conduction band electrons for up to an average of 6 electrons per QD.[30]

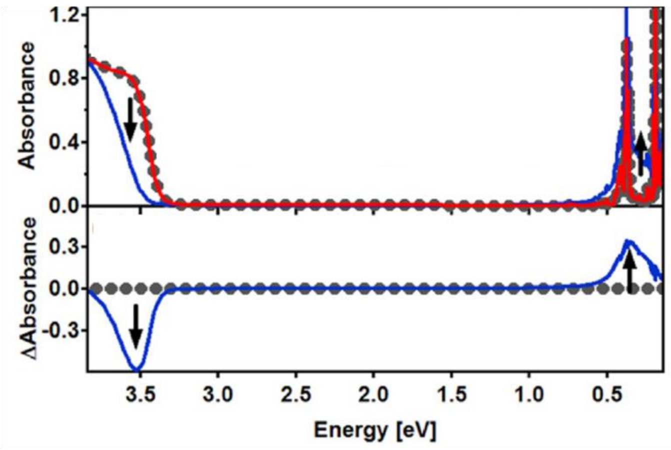

Figure 1.1 Absorption and change in absorption spectra of D = 4.6 nm ZnO nanocrystals upon photodoping. The band gap bleach occurs at ~ 3.5 eV and the increase in the intraband transition occurs at ~ 0.4 eV. The arrows emphasize the direction of change upon charging. Adapted from Ref 30.

In addition to absorption and EPR spectra, luminescence spectra can also probe the presence of extra electrons in the conduction band, although the interpretation of luminescence changes is not straight-forward due to the numerous additional factors that can affect luminescence. In the case of uncharged ZnO QDs, the typical luminescence spectrum consists of two emission features: band-gap emission in the UV region and trap emission in the visible region.[23,24,31] Band-gap emission arises from the recombination of a conduction band electron with a valence band hole. The visible trap emission in ZnO QDs is generally agreed to be due to a conduction band electron recombining with a deeply trapped hole.[32] Upon ZnO charging, both Bahneann, *et al.* and Koch, *et al.* observed the quenching of the trap emission and enhancement of the band-gap emission.[23,24] van Dijken, *et al.* studied the dynamics of trap quenching and recovery in ZnO QDs in N_2 purged solutions and used the dynamics as a probe of the ZnO QD charging and decharging.[33] The visible trap emission has also been shown to recover quantitatively with addition of molecular electron scavengers and was thus used as a probe of electron transfer from ZnO nanocrystals to gold nanoparticles.[34] Despite numerous studies correlating the trap quenching to the charging of ZnO nanocrystals [33-36] , the mechanism of the trap emission quench (and the related enhancement of band-gap emission) is still a subject of debate and will be further discussed in chapter 3.

The ability to reversibly add electrons to the conduction band of ZnO nanoparticles has been important to the exploration of many physical properties of ZnO nanoparticles. Ochsenbein, *et al.* observed the interaction between extra electrons and localized unpaired spins of magnetic dopants by EPR and magnetic susceptibility of photodoped Mn^{2+}: ZnO.[9] They showed that the presence of an extra electron in the conduction band mediates magnetic exchange between all of the Mn^{2+} in the ZnO, and creates a magnetic field strong enough to align ferromagnetically all of Mn^{2+} spins in the QD including the normally antiferromagnetically coupled Mn^{2+} ions at adjacent lattice sites. Negatively charged ZnO was also used to explore the electron transfer dynamics between colloidal ZnO nanocrystals in solution.[37] EPR and UV/Vis absorption measurements demonstrated that negatively charged small ZnO QDs will transfer excess conduction band electrons to the conduction band of large ZnO QDs. These measurements indicated that the difference in the conduction band energies of the two sizes of nanocrystals provided enough of a driving force for electron transfer to occur with a bimolecular rate constant greater than 10^7 M^{-1} s^{-1}.

The band structure of ZnO lends itself to photochemical charging due to the ability of the holes in the valence band to oxidize even poor reductants like ethanol and 2-propanol. Expanding the photodoping method to other semiconductor nanocrystals with more stable holes, like CdSe or PbS, requires a stronger hole scavenger. In addition, the hole scavenger must not form a stable cation radical that can accept the conduction band, and must be compatible with nonpolar solvents commonly used to disperse nanocrystals. Lithium triethylborohydride ($Li[Et_3BH]$) meets these requirements of a hole scavenger needed to photodope semiconductor nanocrystals other than ZnO, such as: CdS, CdSe, and CdTe.[38]

Previously, these chalcogenide materials had only been charged using electrochemical or chemical methods.[17,19,21,27,39] Photodoping, however, provides some advantages over electrochemical and chemical doping. Photodoping is less destructive to QDs than harsh chemical reductants. Chemically reducing CdSe with sodium biphenyl radical causes an increase in absorption just below the band gap that is attributed to transitions of electrons trapped in sub-band gap levels (Figure 1.2a).[40] Growing a passivating ZnS shell before charging diminished this feature. Photodoping, however, can add electrons to the conduction band (as seen by bleach in the band gap transition (Figure 1.2b) without introducing electrons into traps, as evidenced by the absence of the sub-band gap absorption (Figure 1.2b) without a shell present.[38] When thicker shells are needed to avoid populating electron traps upon addition of biphenyl radical, comparison of the absorption spectra upon charging makes it clear that photodoping is a less destructive method of introducing electrons to the conduction band than addition of sodium biphenyl radical.[38] In addition, photodoping has the advantage of being a completely solution-phase method as opposed to the film architecture required for electrochemical charging, where electron transfer between nanocrystals in the complicates analysis.[21]

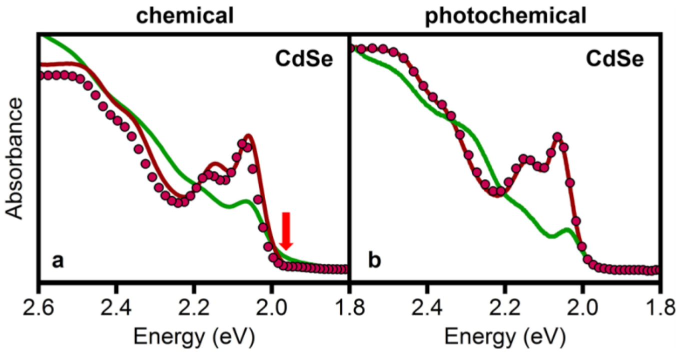

Figure 1.2 Absorption of $D = 4.6$ nm CdSe as prepared (red line), charged (green line), and reoxidized (red circles). Chemical reduction was accomplished with sodium biphenyl radical and photochemical charging was achieved with $Li[Et_3BH]$ as a hole scavenger. The absorption feature in the charged nanocrystals indicative of electrons in traps is marked by the red arrow in the left panel. Adapted from Ref 38.

1.3 Auger Processes in Semiconductors

One consequence of extra charge carriers in nanocrystals is the activation of Auger recombination. In general, Auger recombination is a nonradiative process in which the energy of an electron and hole recombining is transferred to a third carrier, which is promoted to an excited final state in an energy-conserving process. The two types of Auger processes most discussed in the literature are shown in Scheme 1.2. Biexciton Auger recombination (Scheme 1.2 left) occurs when two excitons are formed, one of which recombines nonradiatively and transfers its energy to either the hole or electron of the second exciton. Triexcitons or greater (multiexcitons) can also be formed in which more than two excitons are generated in the nanocrystal. In this case, the multiexcitons decay by Auger recombination sequentially until only one exciton remains.[41] The rate of Auger recombination increases with each additional exciton.[41] The second type of Auger recombination is trion Auger recombination (Scheme 1.2 right) in which recombination of the exciton promotes the third charge carrier to a higher energy level. Trions can be positively charged (an exciton and an extra hole) or negatively charged (an exciton and an extra electron). Related to Auger recombination, Auger ionization can occur when the extra carrier can be excited to an energy level outside the nanocrystal.

Scheme 1.2

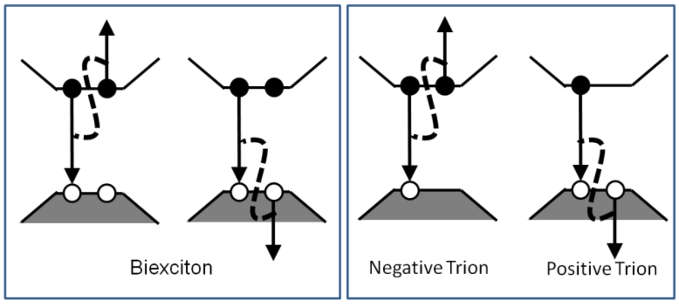

High carrier densities, which lead to the increased probability of multi-carrier Auger recombination in semiconductors, are needed in many device applications such as LEDs[1-3], quantum dot lasers[42,43], and quantum dot solar cells.[4,5] In order to optimize the performance of these devices it is important to understand the mechanisms of multi-carrier recombination that occur in these systems. In bulk semiconductors, Auger recombination is not a very efficient process and requires an activation energy proportional to E_g/k_bT, where E_g is the energy of the band gap and k_b is Boltzmann's constant, due to the requirement that the electron or hole excited in the Auger process conserve both the energy and momentum of the excitonic transition.[44] However, in the quantum confinement regime, conservation of momentum breaks down and the activation energy no longer applies.[45] Instead, conservation of angular momentum becomes important, and the steep confinement potential energy barrier at the surface of colloidal nanocrystals plays a large role in matching the large angular momentum in the ground and excited states.[46] In addition, the Auger recombination rate becomes orders of magnitude faster in nanocrystals than in bulk materials. For this reason, Auger processes become much more significant when replacing bulk semiconductors with QDs in devices where high carrier densities are used.

Biexciton Auger recombination is the most studied Auger process in nanocrystals. Typically, biexcitons are formed by a high power laser pulse incident on a sample of nanocrystals such that each nanocrystal absorbs more than one photon and forms multiple excitons. Biexciton Auger lifetimes are usually measured by transient absorption spectroscopy that probes the recovery of the band-gap bleach after the exciton or biexciton is formed. The biexciton component of the excited state decay is determined by a subtractive process based on the average number of photons absorbed by the nanocrystals per pulse.[41] The size dependence of biexciton Auger recombination has been studied in many different semiconductor QDs. Some experimental reports maintain that the biexciton Auger recombination rate decreases linearly with volume (R^3)[47,48] as a universal property of all semiconductors regardless of electronic structure or nature of the excitonic transition (direct or indirect)[45], even though some other experimental reports conclude that the size dependence of the biexciton Auger recombination ranges from R^4 to R^6.[49-51] A physical explanation for the size dependence of Auger processes has not yet been fully developed. Additionally, the biexciton Auger recombination rate is insensitive to the nature of ligands or surface traps on the nanocrystal.[41,48,50]

Experimental measurements of trion Auger processes are less common than biexciton Auger processes. Most notably, Guyot-Sionnest and co-workers first used electrochemical charging to measure the trion Auger lifetimes of CdSe/CdS quantum dot films with dots ranging from D = 5.3 nm to 6.7 nm.[21] This work showed that the rate of trion Auger recombination is too slow to be responsible for the off states observed in single quantum dot blinking measurements.

Additionally, the ratio of the radiative rate of the exciton and trion were determined experimentally for the first time to be close to 2. Size dependent measurements of trion Auger rates analogous to the biexciton measurements will be presented in chapter 4 of this thesis.

While there are few experimental observations of trion Auger processes, theoretical models of the trion Auger process can predict the rate of trion Auger recombination. These models approximate the biexciton process as the sum of the positive and negative trion rates.[52] Calculations of the Auger rates start with Fermi's golden rule and use a Coulomb or exchange interaction to describe the coupling between the initial and final states.[53,54] These calculations are difficult because of the complex nature of the highly excited final state in an Auger process. It is especially difficult to model size dependences because of quantum interference terms (if final states are modeled as a continuum) or jumps in the energy of an appropriate final state that make the predicted Auger time constants discontinuous as function of size.[46,49,55,56] Experimentally, the discontinuities are not seen because they are masked by the unavoidable size distribution of experimental nanocrystal solutions. Chepic *et al* were able to theoretically address size dependence of Auger ionization rates and achieved good agreement between their model and the experimental size dependence of the Auger ionization process observed in CdS nanocrystals embedded in a glass matrix.[49] Wang, *et al.* calculated both negative and positive trion Auger rates for two sizes of CdSe and used these to predict a biexciton Auger rate that agreed well with experiment, yet there were no experimental values to compare to for the trion calculations.[52]

The most recent development in suppressing Auger effects came from theoretical predictions. Cragg and Efros predicted that Auger ionization rates will be sensitive not only to the width of the confining potential, but also to the shape (Figure 1.3).[46,56] As mentioned previously, the confinement potential is thought to play a large part in the acceleration of Auger processes in nanocrystals relative to bulk materials. Their calculations confirmed the role of confinement potential and predicted that a less steep potential barrier would result in slower Auger recombination. Bae, *et al.* and Javaux, *et al.* showed that alloying core/shell materials decreases the slope of the confinement potential felt by the carriers and significantly slowed Auger recombination.[57,58]

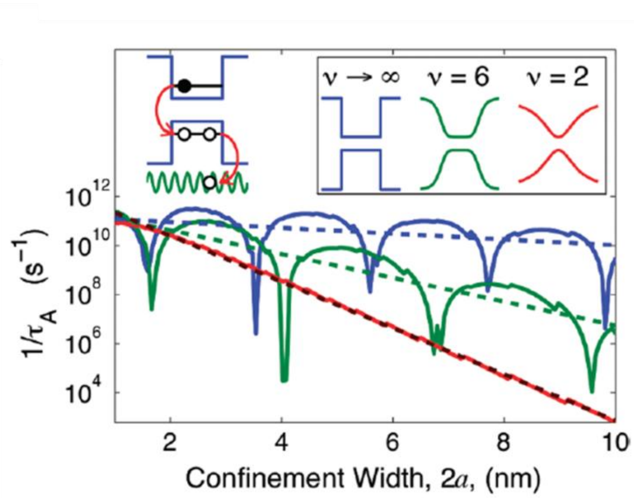

Figure 1.3 Semi-log plot of calculated positive trion Auger ionization rates versus confinement width calculated for different 1D potentials shown in right inset. The left inset schematically shows the Auger ionization process. Adapted from Ref 46.

Auger processes most commonly occur between all delocalized carriers (multi-excitons, and trions) but can also occur when one of the charge carriers is localized either at a trap or on a dopant. This case has been modeled theoretically and observed in bulk semiconductors and quantum wells.[54,59,60] Only recently has its prevalence been observed in nanocrystals. White, *et al.* observed Auger quenching of Mn^{2+} luminescence in Mn^{2+}-doped, electrochemically charged CdS nanocrystals. Due to the long lifetime on Mn^{2+} emission in this system, Auger quenching of Mn^{2+} luminescence was extremely efficient, and a charging level of less than one electron per QD quenched almost all of the Mn^{2+} emission.[20] Auger quenching of trap emission in ZnO nanocrystals will be described in chapters 3 and 4 of this thesis. Electron-trap Auger processes are also surprisingly efficient and the related process of biexciton Auger recombination in the presence of trapped electron has been predicted to be as fast as the biexciton Auger process with all carriers delocalized. This process is important to understand as it is suspected to play a role in QD blinking and in false multi-exciton generation observations in CdSe nanocrystals.[55,61,62]

1.4 Summary

Photodoped semiconductor nanocrystals are an important class of materials for studying new photophysical properties. While ZnO has been studied extensively there are still new areas to study and the photodoping of narrower band gap materials opens up many new exciting possibilities. Auger processes are one of many important aspects of semiconductor nanocrystals that can be studied with photodoped nanocrystals. Some of these aspects of charged semiconductor nanocrystals will be addressed in the following chapters. Chapter 2 explores band-gap engineering of ZnO nanocrystals with Mg^{2+} doping and the applications of this system as a tunable reducing agent. Chapter 3 discusses two aspects of charged ZnO nanocrystals: (*i*) the chemistry and reactivity of the hole scavenging reaction, and (*ii*) a new hypothesis regarding the mechanism of the quench of the visible trap emission and enhancement of the band-gap emission upon introduction of extra electrons to the conduction band of ZnO nanocrystals. Chapter 4 explores the size dependence of trap-electron recombination in ZnO nanocrystals. Chapter 5 uses photodoping to prepare trions in a series of CdSe/ZnS nanocrystals to examine the size dependence of the trion Auger recombination. In Chapter 6, discusses the outlook for future experiments with photodoped nanocrystals.

1.5 Notes to Chapter 1

(1) Anikeeva, P. O.; Madigan, C. F.; Halpert, J. E.; Bawendi, M. G.; Bulović, V. *Phys. Rev. B: Condens. Matter* **2008**, *78*.
(2) Zhang, M.; Bhattacharya, P.; Singh, J.; Hinckley, J. *Appl. Phys. Lett.* **2009**, *95*, 201108.
(3) Bae, W. K.; Park, Y.-S.; Lim, J.; Lee, D.; Padilha, L. A.; McDaniel, H.; Robel, I.; Lee, C.; Pietryga, J. M.; Klimov, V. I. *Nature Comm.* **2013**, *4*, 2661.
(4) Nozik, A. J.; Beard, M. C.; Luther, J. M.; Law, M.; Ellingson, R. J.; Johnson, J. C. *Chem. Rev.* **2010**, *110*, 6873.
(5) Mora-Seró, I.; Giménez, S.; Fabregat-Santiago, F.; Gómez, R.; Shen, Q.; Toyoda, T.; Bisquert, J. *Acc. Chem. Res.* **2009**, *42*, 1848.
(6) Awschalom, D. D.; Bassett, L. C.; Dzurak, A. S.; Hu, E. L.; Petta, J. R. *Science* **2013**, *339*, 1174.
(7) Awschalom, D. D.; Flatte, M. E. *Nature* **2007**, *3*, 153
(8) Cohn, A. W.; Kittilstved, K. R.; Gamelin, D. R. *J. Am. Chem. Soc.* **2012**, *134*, 7938.
(9) Ochsenbein, S. T.; Feng, Y.; Whitaker, K. M.; Badaeva, E.; Liu, W. K.; Li, X.; Gamelin, D. R. *Nature Nanotech.* **2009**, *4*, 681.
(10) White, M. A. Ph.D Thesis, University of Washington, 2012.
(11) Buonsanti, R.; Llordes, A.; Aloni, S.; Helms, B. A.; Milliron, D. J. *Nano Lett.* **2011**, *11*, 4706.
(12) Thu, T. V.; Maenosono, S. *J. Appl. Phys.* **2010**, *107*, 014308.
(13) Luther, J. M.; Jain, P. K.; Ewers, T.; Alivisatos, A. P. *Nat. Matter.* **2011**, *10*, 361.
(14) Schimpf, A. M.; Ochsenbein, S. T.; Buonsanti, R.; Milliron, D. J.; Gamelin, D. R. *Chem. Commun.* **2012**, *48*, 9352.
(15) Wang, T.; Radovanovic, P. V. *J. Phys. Chem. C.* **2011**, *115*, 406.
(16) De Trizio, L.; Buonsanti, R.; Schimpf, A. M.; Llordes, A.; Gamelin, D. R.; Simonutti, R.; Milliron, D. J. *Chem. Mater*. **2013**, *25*, 3383.
(17) Koh, W.-k.; Koposov, A. Y.; Stewart, J. T.; Pal, B. N.; Robel, I.; Pietryga, J. M.; Klimov, V. I. *Scientific Reports* **2013**, *3*, 2004.
(18) Valdez, C. N.; Braten, M.; Soria, A.; Gamelin, D. R.; Mayer, J. M. *J. Am. Chem. Soc.* **2013**, *135*, 8492.
(19) Wehrenberg, B. L.; Guyot-Sionnest, P. *J. Am. Chem. Soc.* **2003**, *125*.
(20) White, M. A.; Weaver, A. L.; Beaulac, R.; Gamelin, D. R. *ACS Nano* **2011**, *5*, 4158.
(21) Jha, P., P.; Guyot-Sionnest, P. *ACS Nano* **2009**, *3*, 1011.
(22) Haase, M.; Weller, H.; Henglein, A. *J. Phys. Chem.* **1988**, *92*, 482
(23) Koch, U.; Fojtik, A.; Weller, H.; Henglein, A. *Chem. Phys. Lett.* **1985**, *122*, 507.
(24) Bahnemann, D. W.; Kormann, C.; Hoffmann, M. R. *J. Phys. Chem.* **1987**, *91*, 3789.
(25) Shim, M.; Guyot-Sionnest, P. *J. Am. Chem. Soc.* **2001**, *123*, 11651.
(26) Germeau, A.; Roest, A. L.; Vanmaekelbergh, D.; Allan, G.; Delerue, C.; Meulenkamp, E. A. *Phys. Rev. Lett.* **2003**, *90*, 097401.
(27) Shim, M.; Guyot-Sionnest, P. *Nature* **2000**, *407*, 981
(28) Liu, W. K.; Whitaker, K. M.; Kittilstved, K. R.; Gamelin, D. R. *J. Am. Chem. Soc.* **2006**, *128*, 3910.
(29) Whitaker, K. M.; Ochsenbein, S. T.; Polinger, V. Z.; Gamelin, D. R. *J. Phys. Chem. C.* **2008**, *112*, 14331

(30) Liu, W. K.; Whitaker, K. M.; Smith, A. L.; Kittilstved, K. R.; Robinson, B. H.; Gamelin, D. R. *Phys. Rev. Lett.* **2007**, *98*.

(31) Norberg, N. S.; Gamelin, D. R. *J. Phys. Chem. B* **2005**, *109*, 20810.

(32) van Dijken, A.; Meulenkamp, E. A.; Vanmaekelbergh, D.; Meijerink, A. *J. Lumin.* **2000**, *90*, 123.

(33) van Dijken, A.; Mulenkamp, E. A.; Vanmaekelbergh, D.; Meijerink, A. *J. Phys. Chem. B* **2000**, *104*, 4355.

(34) Subramanian, V. W., E. E.; Kamat, P. V. *J. Phys. Chem. B* **2003**, *107*, 7479.

(35) Stroyuk, O. L.; Dzhagan, V. M.; Shvalagin, V. V.; Kuchmiy, S. Y. *J. Phys. Chem. C* **2010**, *114*, 220.

(36) Yamamoto, S. *J. Phys. Chem. C* **2011**, *115*, 21635.

(37) Hayoun, R.; Whitaker, K. M.; Gamelin, D. R.; Mayer, J. M. *J. Am. Chem. Soc.* **2011**, *133*, 4228.

(38) Rinehart, J. D.; Schimpf, A. M.; Weaver, A. L.; Cohn, A. W.; Gamelin, D. R. *J. Am. Chem. Soc.* **2013**, *134*, 16175.

(39) Wang, C.; Wehrenberg, B. L.; Woo, C. Y.; Guyot-Sionnest, P. *J. Phys. Chem. B* **2004**, *108*, 9027.

(40) Shim, M.; Wang, C. J.; Guyot-Sionnest, P. *J. Phys. Chem. B* **2001**, *105*, 2369.

(41) Klimov, V. I.; Mikhailovsky, A. A.; McBranch, D. W.; Leatherdale, C. A.; Bawendi, M. G. *Science* **2000**, *287*, 1011.

(42) Fathpour, S.; Mi, Z.; Bhattacharya, P.; Kovsh, A. R.; Mikhrin, S. S.; Krestnikov, I. L.; Kozhukhov, A. V.; Ledentsov, N. N. *Appl. Phys. Lett.* **2004**, *85*, 5164.

(43) Klimov, V. I. *J. Phys. Chem. B* **2006**, *110*, 16827.

(44) Haug, A. *J. Phys. Chem. Solids* **1988**, *49*, 599.

(45) Robel, I.; Gresback, R.; Kortshagen, U.; Schaller, R. D.; Klimov, V. I. *Phys. Rev. Lett.* **2009**, *102*, 1777404.

(46) Cragg, G. E.; Efros, A. L. *Nano Lett.* **2010**, *10*, 313.

(47) Achermann, M.; Hollingsworth, J. A.; Klimov, V. I. *Phys. Rev. B: Condens. Matter* **2003**, *68*, 245302.

(48) Pandey, A.; Guyot-Sionnest, P. *J. Chem. Phys.* **2007**, *127*, 111104.

(49) Chepic, D. I.; Efros, A. L.; Ekimov, A. I.; Ivanov, M. G.; Kharchenko, V. A.; Kudriavtsev, I. A.; Yazeva, T. V. *J. Lumin.* **1990**, *47*, 113.

(50) Kobayashi, Y.; Nishimura, T.; Yamaguchi, H.; Tamai, N. *J. Phys. Chem. Lett.* **2011**, *2*, 1051.

(51) Kobayashi, Y.; Tamai, N. *J. Phys. Chem. C.* **2010**, *114*, 17550.

(52) Wang, L.-W.; Califano, M.; Zunger, A.; Franceschetti, A. *Phys. Rev. Lett.* **2003**, *91*, 056404.

(53) Landsberg, P. T. *Recombination in Semiconductors*; Cambridge University Press: Cambridge, 1991.

(54) Landsberg, P. T.; Rhys-Roberts, C.; Lal, P. *P. Phys. Soc.* **1964**, *84*, 916.

(55) Califano, M. *ACS Nano* **2011**, *5*, 3614.

(56) Climente, J. I.; Movilla, J. L.; Planelles, J. *Small* **2012**, *8*, 754.

(57) Bae, W. K.; Padilha, L. A.; Park, Y.-S.; McDaniel, H.; Robel, I.; Pietryga, J. M.; Klimov, V. I. *ACS Nano* **2013**, *7*, 3411.

(58) Javaux, C.; Mahler, B.; Dubertret, B.; Shabaev, A.; Rodina, A. V.; Efros, A. L.; Yakovlev, D. R.; Liu, F.; Bayer, M.; Camps, G.; Biadala, L.; Buil, S.; Quelin, X.; Hermier, J.-P. *Nature Nanotech.* **2013**, *8*, 206.
(59) Robbins, D. J. *J. Phys. C. Solid State* **1983**, *16*, 3825.
(60) Allen, J. W. *J. Phys. C. Solid State* **1986**, *19*, 6287.
(61) Califano, M. *J. Phys. Chem. C* **2011**, *115*, 18051.
(62) Tyagi, P.; Kambhampati, P. *J. Chem. Phys.* **2011**, *134*, 094706.

Chapter 2: Mg^{2+} Doped in ZnO for Tunable Photodoped Electrons

Colloidal reduced ZnO nanocrystals are potent reductants for one-electron or multielectron redox chemistry, with reduction potentials tunable via the quantum confinement effect. Other methods for tuning the redox potentials of these unusual reagents are desired. Here, we describe synthesis and characterization of a series of colloidal $Zn_{1-x}Mg_xO$ and $Zn_{0.98-x}Mg_xMn_{0.02}O$ nanocrystals in which Mg^{2+} substitution is used to tune the nanocrystal reduction potential. The effect of Mg^{2+} doping on the band-edge potentials of ZnO was investigated using electronic absorption, photoluminescence, and magnetic circular dichroism spectroscopies. Mg^{2+} incorporation widens the ZnO gap by raising the conduction-band potential and lowering the valence-band potential at a ratio of 0.68:0.32. Mg^{2+} substitution is far more effective than Zn^{2+} removal in raising the conduction-band potential, and allows better reductants to be prepared from $Zn_{1-x}Mg_xO$ nanocrystals than can be achieved via quantum confinement of ZnO nanocrystals. The increased conduction-band potentials of $Zn_{1-x}Mg_xO$ nanocrystals compared to ZnO nanocrystals are confirmed by demonstration of spontaneous electron transfer from *n*-type $Zn_{1-x}Mg_xO$ nanocrystals to smaller (more strongly quantum confined) ZnO nanocrystals. This work was done in conjunction with Dr. Kevin Kittilstved (University of Massachusetts, Amherst) and was published in Ref. 1.

2.1 Introduction

Colloidal ZnO nanocrystals can be "charged" photochemically to give kinetically stable suspensions of powerful reductants.[2-8] The extra conduction-band electrons added by this process can be monitored by electronic absorption[2-5] or electron paramagnetic resonance (EPR) spectroscopies.[4-7] When exposed to air or mixed with suitable electron acceptors (*e.g.*, uncharged nanocrystals or molecules), these reduced nanocrystals are rapidly re-oxidized,[2-5,8-10] making charged ZnO nanocrystals attractive reagents for fundamental studies of interfacial electron transfer processes involving semiconductor nanostructures. The conduction band-edge potentials of colloidal ZnO nanocrystals can be tuned via quantum confinement to achieve a total range of ~150 mV, and multiple electrons can be introduced into a single nanocrystal,[5,10-13] making them unusually versatile reductants for one- or multi-electron redox chemistries.[14] For some reactions, even stronger reductants may be desired than can be achieved via quantum confinement. Here, we examine the use of Mg^{2+} substitution to tune ZnO nanocrystal reduction potentials. Isovalent cation substitution is known to alter the conduction-band potentials of many semiconductor nanocrystals,[15-18] and hence should provide an effective means of tuning the chemical reactivities of these unusual colloidal ZnO-based reagents, but this parameter has not yet been thoroughly examined.

Interest in $Zn_{1-x}Mg_xO$ frequently stems from its potential applications in optoelectronic devices, for example as a barrier layer in ZnO-based heterostructures,[17-20] in UV sensors,[21] and in ZnO-based lasing devices.[22] $Zn_{1-x}Mg_xO$ thin films have been prepared by a variety of techniques including pulsed laser deposition (PLD),[23] low-temperature chemical vapor deposition,[24] molecular beam epitaxy,[25] radio-frequency magnetron sputtering,[26] and sol-gel deposition.[27] Colloidal $Zn_{1-x}Mg_xO$ nanocrystals have been synthesized by high-temperature, air-free methods.[28,29] Mg^{2+} and Zn^{2+} have similar tetrahedral ionic radii (0.57 Å and 0.60 Å),[30] contributing to the relatively high solid solubility of Mg^{2+} in wurtzite ZnO. In epitaxial thin films made by PLD, for example, Mg^{2+} is incorporated into the wurtzite lattice structure up to $x \sim 0.33$ without detectable phase segregation.[23] Previous studies of $Zn_{1-x}Mg_xO$ thin films and nanocrystals have primarily focused on characterizing the change in band gap with x using electronic absorption and luminescence spectroscopies.[23,26,27,31,32] For many applications, however, the specific band offsets at $Zn_{1-x}Mg_xO$/ZnO interfaces are important,[17,18,25] but quantification of the shifts of individual bands with x is more challenging than quantification of the change in the energy gap.

We report here the synthesis of a series of colloidal wurtzite $Zn_{1-x}Mg_xO$ and $Zn_{1-x-y}Mg_xMn_yO$ nanocrystals using a simple room-temperature procedure developed previously for doping ZnO nanocrystals with Co^{2+}, Ni^{2+}, or Mn^{2+} ions.[33,34] We demonstrate that shifts of the individual band-edge potentials with x can be determined by measurement of trap photoluminescence energies, Mn^{2+} donor-type photoionization energies, and band-to-band transition energies. These data indicate that increasing x in these wurtzite $Zn_{1-x}Mg_xO$ nanocrystals increases the energy gap primarily by raising the conduction-band potential, but also by shifting the valence-band potential. Mg^{2+} substitution is found to be much more effective than quantum confinement in raising the conduction-band potentials of ZnO-based nanocrystals. The absolute increase in conduction-band potential with Mg^{2+} incorporation is unambiguously confirmed by demonstration of spontaneous inter-nanocrystal electron transfer from $Zn_{1-x}Mg_xO$ nanocrystals to more strongly quantum confined ZnO nanocrystals.

2.2 Experimental

2.2.A Synthesis. Colloidal ZnO and $Zn_{1-x-y}Mg_xMn_yO$ nanocrystals were synthesized using a base-initiated hydrolysis/condensation procedure described previously.[33,34] Briefly, 1.6 equivalents of 0.5 M tetramethylammonium hydroxide in ethanol were added dropwise to a 0.1 M solution of zinc acetate (+ manganese acetate and magnesium acetate as desired) in dimethylsulfoxide (DMSO). For $Zn_{1-x}Mg_xO$ nanocrystals, magnesium acetate was added to the DMSO solution along with the zinc acetate while keeping the cation-to-hydroxide ratio constant. To obtain nanocrystals of different diameters from a given synthesis, aliquots were removed from the growth solution at four different stages: immediately following the addition of the base, 30 minutes later, 2 hours later, and 1 to 3 days later. Between 2 hours and 3 days, the growth solution was heated at 50 °C. For each aliquot, the nanoparticles were washed by precipitating with heptane and resuspending in ethanol. Mg^{2+} addition inhibits nanocrystal growth, and to achieve the largest nanocrystals with high Mg^{2+} content, the nanocrystals were heated in neat dodecylamine at 160 °C for ~20 min before washing. The experiments here were performed on dodecylamine-ligated nanocrystals suspended in toluene, prepared by adding dodecylamine to an ethanolic suspension of nanocrystals until the nanocrystals precipitated (at ~200-700:1 mole ratio), followed by centrifugation and resuspension in toluene.

2.2.B Physical measurements. Electronic absorption spectra were collected at room temperature using a Cary 500 spectrometer. Photoluminescence spectra were collected at room temperature by exciting the colloidal nanocrystals with either 337 nm light from a nitrogen laser or 330 nm light from a 200 W tungsten-halogen lamp dispersed through a 0.3 m monochrometer, and detecting with a nitrogen-cooled CCD. Magnetic circular dichroism (MCD) spectra were collected using an Aviv 40DS spectropolarimeter with a water-cooled electromagnet. Mg^{2+} and Mn^{2+} concentrations ($x \pm 0.01$) were determined analytically using inductively coupled plasma mass spectrometry and atomic emission spectroscopy (ICP-MS/AES). In some cases, data are reported using nominal Mg^{2+} concentrations (x_n) rather than analytical concentrations (x), where x_n is the Mg^{2+} cation mole fraction of the initial reaction mixture. The two values are within 10% of one another in all cases where x was determined (with remaining cations removed by washing), making this representation acceptable for relative measurements. EPR spectra were collected using a Bruker Elexys E580 X-band spectrometer. EPR spectra were recorded under steady-state conditions achieved by continuously irradiating samples (with a Hg/Xe arc-lamp) open to air within the EPR cavity. These EPR signals decay in the dark with time constants of $\tau \approx$ 1 min, i.e., sufficiently slow for inter-nanocrystal electron transfer ($\tau < 5\ \mu s$) to reach equilibrium when mixtures of nanocrystals are used. EPR g values were measured using using diphenylpicrylhydrazyl (DPPH) as an internal reference. X-ray diffraction (XRD) data were collected using a Bruker F8 Focus instrument with a Cu Kα radiation source operating at 40kV and 40mA, with KCl as an internal reference.

Band gap energies (E_g) were approximated by the energies at which the optical density at the absorption edge reached half of its maximum value. Diameters of $Zn_{1-x}Mg_xO$ and $Zn_{1-x-y}Mg_xMn_yO$ nanocrystals were estimated from XRD data using the Scherrer equation.[35] Diameters of ZnO nanocrystals were estimated from electronic absorption spectra using empirical relationships.[36,37]

2.3 Results and Analysis

2.3.A Nanocrystal characterization. Figure 2.1a shows powder XRD data collected for $d = 4.3$ nm $Zn_{1-x}Mg_xO$ nanocrystals at $x = 0$ and 0.18, with x determined analytically (see section 2.2.A). The peaks between 30° and 38° are characteristic of the wurtzite lattice structure, and their broad peak widths confirm formation of nanocrystals, as seen previously with this synthetic method.[33,34,38] The sharp peak at 40.5° is from KCl that was added as an internal reference. Note the absence of any detectable rocksalt MgO peak at 42.5°. There are conflicting results in the literature concerning the direction of the changes in a and c lattice parameters with increasing Mg^{2+} incorporation,[23,32] but in all cases these changes are small. In our samples, a also does not shift significantly over the range $0 \leq x \leq 0.18$, but very small shifts would be obscured by the broad peak widths of these nanocrystals. Figure 2.1b shows transmission electron microscopy (TEM) images of $Zn_{1-x}Mg_xO$ nanocrystals at $x_n = 0.20$, confirming their quasi-spherical shapes and crystallinity. Overall, these data are consistent with formation of $Zn_{1-x}Mg_xO$ nanocrystals.

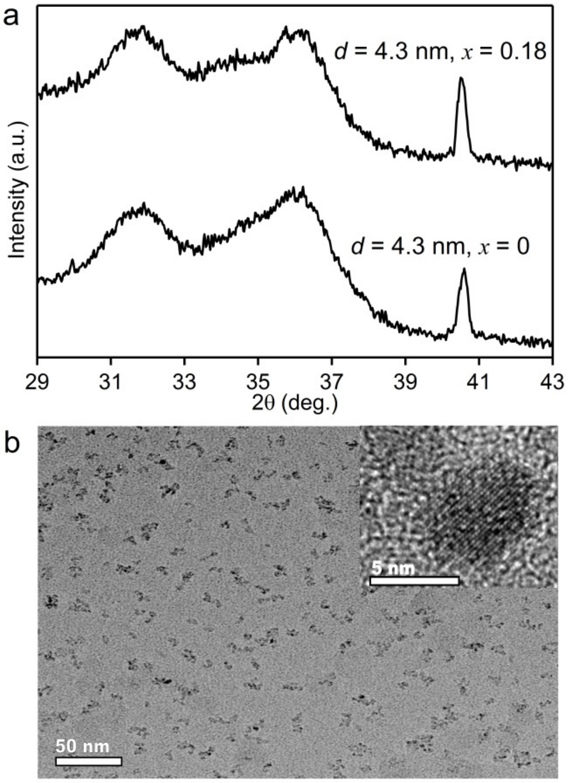

Figure 2.1. (a) Powder XRD data collected for $d = 4.3$ nm $Zn_{1-x}Mg_xO$ nanocrystals with $x = 0$ and $x = 0.18$. The Mg^{2+} contents (x) were determined analytically, with an estimated uncertainty of ±0.01. The peak at $2\theta = 40.5°$ comes from KCl, which was included as an internal reference. **(b)** TEM images of $Zn_{1-x}Mg_xO$ nanocrystals ($x_n = 0.20$).

2.3.B Spectroscopic properties. Figure 2.2a plots electronic absorption and photoluminescence spectra collected for a series of $Zn_{1-x}Mg_xO$ nanocrystals with $d >$ ~6.0 nm (where quantum confinement effects are minimal) and with different values of x. The absorption edge shifts to higher energy with increasing x, as summarized in Fig. 2.2b. The photoluminescence spectra are dominated by midgap trap luminescence centered at ~2.2 eV. This trap luminescence also shifts to higher energy with increasing x, as summarized in Fig. 2.2b.

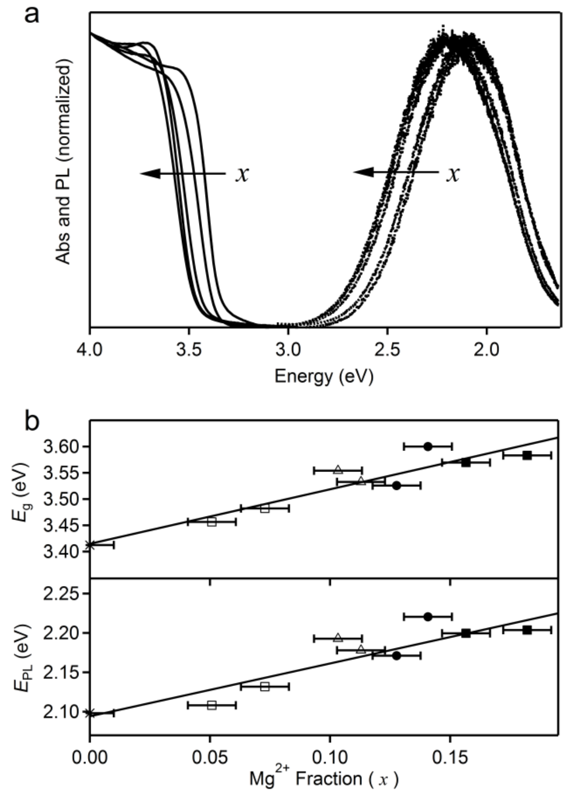

Figure 2.2. **(a)** Room-temperature electronic absorption (solid line) and luminescence (dotted line) spectra of colloidal $Zn_{1-x}Mg_xO$ ($0 \leq x \leq 0.18$) nanocrystals with diameters $d > 6.0$ nm, where quantum confinement is negligible. The arrows indicate direction of increasing x. **(b)** Band-gap energies (half-maxima of electronic absorption spectra) for ZnO and $Zn_{1-x}Mg_xO$ nanocrystals with $d > 5.0$ nm and trap emission energies for the same samples plotted vs x. To illustrate agreement between x and x_n, the data are marked using symbols corresponding to $x_n = 0$ (star), 0.05 (open square), 0.10 (open triangle), 0.15 (closed circle), 0.20 (closed square). The best-fit lines are described by $E_g = (3.41 + 1.04x)$ eV and $E_{PL} = (2.09 + 0.67x)$ eV.

A linear fit of the absorption data yields $E_g = (3.41 + 1.04x)$ eV. A linear fit of the PL data yields $E_{PL} = (2.09 + 0.67x)$ eV. The absorption and PL features thus both shift to higher energy with increasing x, but with different slopes. The dependence of E_g on x is only half as large as some that have been reported in the literature for bulk and nanocrystalline $Zn_{1-x}Mg_xO$ (~$2x$ eV),[23,26,28,39] but is approximately three times larger than others.[32] We tentatively attribute these discrepancies to inhomogeneous Mg^{2+} distributions, for example possible Mg^{2+} enrichment at the nanocrystal surfaces in our case. Importantly, these discrepancies illustrate the need for a method of assessing band potentials that is *independent* of detailed knowledge of the Mg^{2+} distribution. As shown below, photoluminescence and EPR spectroscopies are both effective in this capacity.

The visible trap luminescence of colloidal ZnO nanocrystals has been attributed to recombination of an electron in or near the conduction band with a deeply trapped hole.[40-44] Despite many years of investigation, the microscopic identities of the active traps remain poorly understood. Because of the large surface-to-volume ratios, surface chemistry strongly influences the luminescence of ZnO nanocrystals.[9,38,43,45-48] For example, in nanocrystals prepared by this and other synthetic methods, correlations have been observed between the presence of surface hydroxide moieties and visible trap luminescence intensity,[38,46] suggesting surface hole localization in this excited state. Surface modification with small cationic or anionic moieties strongly alters this trap PL.[48] Although the microscopic identities of the active traps remain unclear, the holes involved in this PL are deeply trapped and consequently insensitive to quantum confinement. The slope of a plot of E_{PL} vs E_g for a series of quantum confined ZnO nanocrystals simply reflects the dependence of the conduction band potential on electron quantum confinement.[42] Experimentally, this slope was found to be ~0.60 for ZnO nanocrystals,[42] in good agreement with expectations from the effective mass approximation (~0.64).

A similar analysis can now be applied to understanding the visible trap PL of $Zn_{1-x}Mg_xO$ nanocrystals. Figure 2.3 replots the data from Fig. 2.2 (along with data from samples where x was not determined analytically) as E_{PL} vs E_g. This representation allows shifts in the conduction band potentials to be assessed without explicit consideration of x and without any assumption about Mg^{2+} spatial distribution. Plotting the data in this way yields a straight line with slope $\Delta E_{PL}/\Delta E_g = 0.68$. The slope obtained here for ZnO nanocrystals due solely to quantum confinement is 0.67, in good agreement with previous observations.[42] If Mg^{2+} substitution only changed the conduction band potential as suggested by DOS calculations,[49,50] then $\Delta E_{PL}/\Delta E_g \approx 1$. Instead, the slope of 0.68 in Fig. 2.3 implies that Mg^{2+} incorporation into ZnO shifts *both* the conduction- and valence-band potentials in a ratio $\Delta E_{CB}:\Delta E_{VB}$ ~ 0.68:0.32. Whereas the shift in CB potential reflects the absence of resonance between Mg^{2+} and Zn^{2+} 4s orbitals, the shift in VB potential is likely due to the impact of the different Mg^{2+} and Zn^{2+} electronegativities on M^{2+}-O^{2-} bonding. Previous valence-band XPS measurements and modeling studies of ZnO quantum wells with $Zn_{1-x}Mg_xO$ barrier layers have estimated ratios of $\Delta E_{CB}:\Delta E_{VB}$ between 1:1 and 0.7:0.3,[17,18,25] in good agreement with the ratio found here for the colloidal $Zn_{1-x}Mg_xO$ nanocrystals.

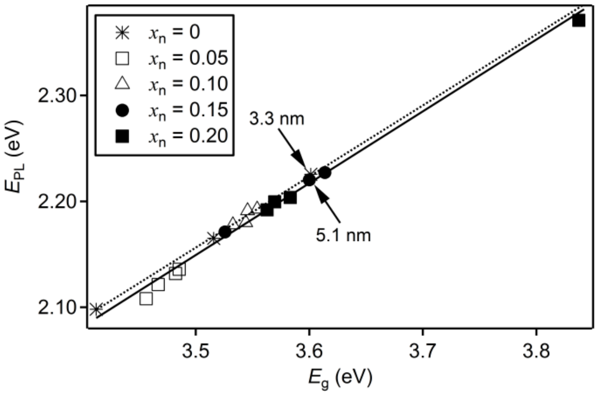

Figure 2.3. Peak energy of the visible trap luminescence plotted versus the band gap energy (half maxima of the electronic absorption spectra) for ZnO and $Zn_{1-x}Mg_xO$ nanocrystals of different diameters and values of x. A linear fit of the $Zn_{1-x}Mg_xO$ data yields a slope of 0.68 (solid). A linear fit of the ZnO data (*) yields a slope of 0.67 (dotted). The arrows highlight the fact that a d = 3.3 nm ZnO (*) nanocrystal and a d = 5.1 nm $Zn_{0.85}Mg_{0.15}O$ (•) nanocrystal have the same spectroscopic properties.

It is conceivable that the nature of the luminescent trap state is not independent of Mg^{2+} as assumed in the analysis above. As an independent crosscheck of the impact of Mg^{2+}

incorporation on the conduction-band potential, $Zn_{1-x}Mg_xO$ nanocrystals were therefore prepared with Mn^{2+} as a co-dopant. Mn^{2+} in ZnO possesses a midgap donor-type photoionization state formally involving a $Mn^{2+} \rightarrow$ conduction band charge transfer ($ML_{CB}CT$) excitation,[16,51,52] although some researchers favor a Zhang-Rice-like description of these excited states.[53,54] This $ML_{CB}CT$ transition appears as a broad structureless midgap band in electronic absorption spectra and as a derivative feature in MCD spectra of Mn^{2+}-doped ZnO.[16,34,55]

Figure 2.4 shows the 298 K electronic absorption and 298 K, 1 T MCD spectra of a series of colloidal $Zn_{0.98-x}Mg_xMn_{0.02}O$ nanocrystals with $x = 0.00$, 0.05, and 0.10. The $ML_{CB}CT$ transition is observed in the absorption spectra of all three samples as a broad band centered at ~3.0 eV, and as a derivative-shaped MCD feature over the same energies. The data show a clear shift of this $ML_{CB}CT$ transition to higher energy with increasing x, with $\Delta E_{CT} \sim 190$ meV at $x = 0.10$. Because Mn^{2+} is a deep donor in ZnO, its potential is pinned,[56-58] and this shift in the $ML_{CB}CT$ transition energy is predominantly attributable to the change in conduction band potential, ΔE_{CB}. All three samples are close to the bulk size regime, and quantum confinement cannot account for more than ~10 meV of the observed shift. Plotting the data from Fig. 2.4 as ΔE_{CB} vs ΔE_g allows direct comparison with the data from Fig. 2.3, and the results from the two experiments agree well. These data thus provide an independent demonstration that Mg^{2+} substitution raises the CB potential of the ZnO nanocrystals.

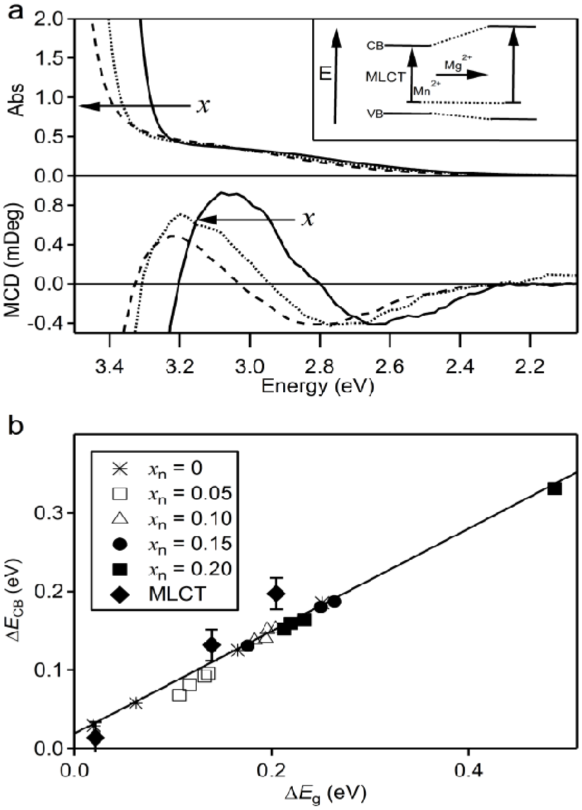

Figure 2.4. **(a)** 298 K electronic absorption and 298 K, 1 T MCD spectra of $Zn_{0.98-x}Mg_xMn_{0.02}O$ (x = 0, 0.05, 0.10 (±0.01)) colloidal nanocrystals, with diameters of 8.0, 5.0, and 4.6 nm (±0.5 nm), respectively, as determined by XRD analysis. The arrows indicate the direction of increasing x. Optical densities of the $ML_{CB}CT$ transition were below 0.60 for the MCD measurements. The y axes correspond to those of the $x = 0$ measurement. **(b)** Plot of ΔE_{CB} vs ΔE_g from the MCD data (diamonds) and from the PL data of Fig. 3. The inset to (a) describes the $ML_{CB}CT$ shift with x schematically.

2.3.C Charged $Zn_{1-x}Mg_xO$ nanocrystals. The motivation for preparing colloidal $Zn_{1-x}Mg_xO$ nanocrystals was to explore Mg^{2+} substitution as an approach to tuning ZnO nanocrystal reduction potentials relevant to actual electron-transfer reactions. To evaluate the properties of the CB electrons directly, these nanocrystals were photodoped to form colloidal *n*-type $Zn_{1-x}Mg_xO$ nanocrystals.[2-8] As demonstrated previously, EPR spectroscopy is a superb tool for probing the properties of the extra electrons in colloidal *n*-type ZnO nanocrystals[4-8] and in ZnO nanocrystalline powders.[59-61] This technique has demonstrated that these electrons are indeed conduction-band-like, and in particular are delocalized over the entire colloidal nanocrystal volume.[6,7,62] The EPR signals of a series of *n*-type $Zn_{1-x}Mg_xO$ nanocrystals of different *x* and the same diameter are shown in Fig. 2.5a. Figure 2.5b plots these *g* values vs E_g (determined by electronic absorption spectroscopy), along with data collected for nanocrystals of the same *x* but different diameters. For a given diameter, the electron *g* value increases with increasing *x*, ranging from 1.961 to 1.975 in a similar way as can be achieved through quantum confinement alone,[6] but spanning a broader range. A similar increase in electron *g* values with *x* has been observed recently in oriented epitaxial thin films of $Zn_{1-x}Mg_xO$ grown by MBE.[63]

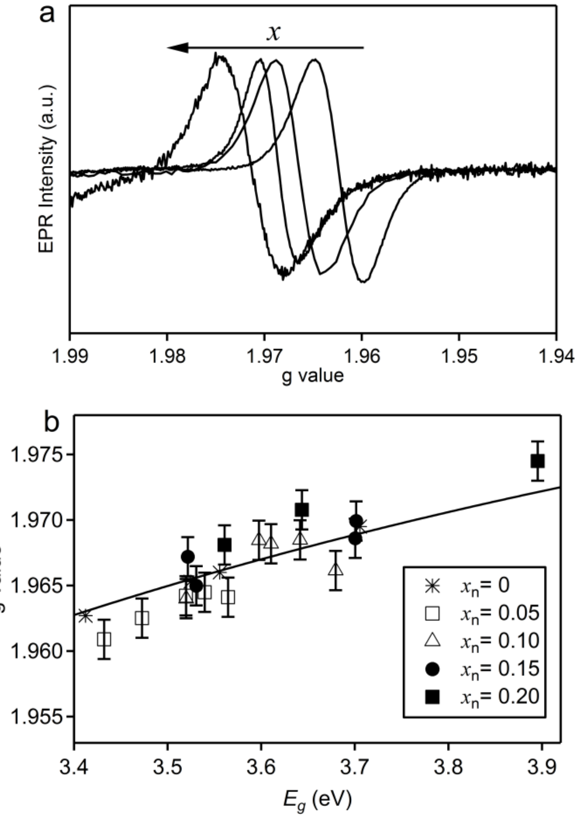

Figure 2.5. **(a)** Room-temperature EPR spectra of colloidal *n*-type $Zn_{1-x}Mg_xO$ ($x = 0.05$, 0.10, 0.13, and 0.17) nanocrystals with $d > 6$ nm. The arrow indicates direction of increasing *x*. **(b)** A plot of the EPR *g* values vs E_g for nanocrystals of different diameters and values of x_n. The solid line shows the best fit of the *n*-type ZnO nanocrystal data, obtained using eq 1 with $P^2 = 20$ eV and Δ_{SO} fitted to 35 meV.

From Fig. 2.5, Mg^{2+} substitution and quantum confinement yield indistinguishable relationships between *g* and E_g, in excellent agreement with the results shown in Fig. 2.3. A **k·p** perturbation model has been applied successfully to describe the trend in colloidal ZnO nanocrystal g values with quantum confinement (eq 2.1),[6] and as shown below this model applies well to colloidal $Zn_{1-x}Mg_xO$ nanocrystals, too. In eq 2.1, g_e is the free electron g value (2.0023), E_g is the band gap energy, P^2 is the interband mixing coefficient, and Δ_{SO} describes the valence-band spin-orbit splitting. The solid line in Fig. 2.5b plots the curve predicted by eq 2.1 using P^2 = 20 eV and a best-fit value of Δ_{SO} = 35 meV, which agrees with the value of Δ_{SO} = 40 meV determined for colloidal ZnO nanocrystals in ref. 6. These results indicate that the extra electrons remain CB-like in $Zn_{1-x}Mg_xO$ nanocrystals, with Mg^{2+} incorporation playing a role very similar to reduction of the electron's confinement volume. Interestingly, comparison of nanocrystals achieving the same g value via quantum confinement and via Mg^{2+} substitution reveals that Mg^{2+} incorporation is far more effective than Zn^{2+} removal in widening the energy gap, and hence in shifting the conduction-band potential and altering the g value of a conduction-band electron. For example, both d = 3.7 nm ZnO and d = 6.0 nm $Zn_{0.90}Mg_{0.10}O$ nanocrystals have g values of ~1.965, but the former has only ~1100 Zn^{2+} cations, whereas the latter has ~4270 Zn^{2+} and ~470 Mg^{2+} cations. This result highlights the efficacy of Mg^{2+} substitution in tuning the ZnO energy gap. Because Mg^{2+} is likely segregated toward the nanocrystal surfaces here, these results represent a lower limit for the tenability of nanocrystal potentials achievable using Mg^{2+} substitution.

$$g^* = g_e - \frac{2}{3}\left(\frac{P^2\Delta_{SO}}{E_g\left(E_g + \Delta_{SO}\right)}\right) \tag{2.1}$$

2.3.D Electron-transfer reactivity. The above data all suggest that Mg^{2+} substitution into ZnO nanocrystals is effective in raising the nanocrystal conduction band, which should make *n*-type $Zn_{1-x}Mg_xO$ nanocrystals more potent reductants than comparable *n*-type ZnO nanocrystals. We have previously demonstrated rapid (< 5 μs) spontaneous electron transfer between colloidal ZnO quantum dots, with driving forces derived from electron quantum confinement.[8] Here, we show that such electron transfer can be used to determine the relative conduction band potentials of ZnO and $Zn_{1-x}Mg_xO$ nanocrystals under equilibrium conditions.

Figure 2.6 plots the EPR spectrum collected after UV irradiation of an equimolar mixture of 2.9 nm ZnO ($g = 1.9695$, $E_g = 3.71$ eV) and ~4.0 nm $Zn_{0.75}Mg_{0.25}O$ ($g = 1.9745$, $E_g = 3.89$ eV) nanocrystals, conditions under which both nanocrystals are excited simultaneously at approximately the same rate. Because inter-nanocrystal electron transfer is fast ($\tau < 5$ μs),[8] relative to reoxidation ($\tau \approx 1$ min), photochemical reduction is followed by rapid equilibration of the electron population according to the relative conduction band potentials of the ZnO and $Zn_{0.75}Mg_{0.25}O$ nanocrystals. The EPR spectrum of the individual nanocrystals (phodoped) are also plotted in Figure 2.6 for comparison. Only the ZnO nanocrystals are observed in the EPR spectrum of the mixture, indicating that the electrons reside predominantly in the ZnO nanocrystals at equilibrium. This result demonstrates that $Zn_{0.75}Mg_{0.25}O$ nanocrystals are better reductants than even smaller ZnO nanocrystals, despite the greater quantum confinement in the latter. This finding agrees well with the difference in the trap luminescence energies of these two samples, from which a driving force of ~130 mV is deduced for electron transfer from the $Zn_{0.75}Mg_{0.25}O$ nanocrystals to the ZnO nanocrystals of Figure 2.6. The visible trap luminescence of ZnO-based nanocrystals can thus be used as a probe of the conduction-band reduction potentials of ZnO and related nanocrystals. Overall, the $Zn_{1-x}Mg_xO$ trap luminescence ranges from ~2.1 to ~2.4 eV (Fig. 2.3), corresponding to a ~300 mV range of tunability in nanocrystal reduction potentials. Importantly, this tunability is approximately twice as large as could be achieved from quantum confinement of ZnO nanocrystals alone (*i.e.*, without Mg^{2+}

incorporation), validating the original hypothesis that Mg^{2+} substitution is effective in this capacity.

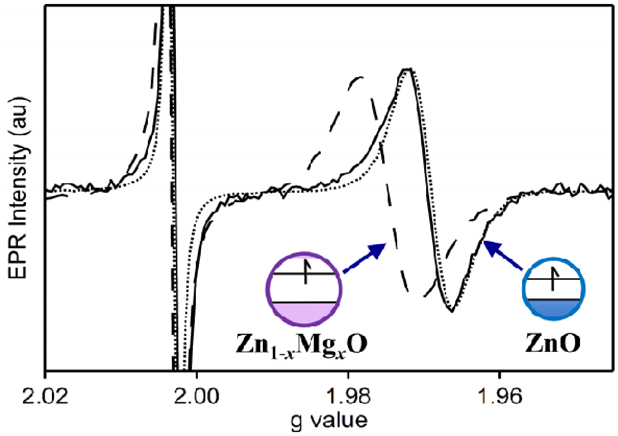

Figure 2.6. Room temperature EPR spectra of ZnO nanocrystals ($d \approx 2.9$ nm, dotted), $Zn_{0.75}Mg_{0.25}O$ nanocrystals ($d \approx 4.0$ nm, dashed), and an equimolar mixture of the two (solid), all following UV irradiation to introduce additional conduction-band electrons. The signal at $g = 2.0036$ is from DPPH. The observation of just ZnO electrons in the mixture spectrum indicates that the equilibrium distribution of electrons in this mixture strongly favors population of the ZnO subset of nanocrystals, confirming that the $Zn_{0.75}Mg_{0.25}O$ nanocrystals have more negative conduction-band potentials.

2.4 Conclusion

Colloidal $Zn_{1-x}Mg_xO$ nanocrystals were synthesized by a hydrolysis and condensation reaction performed at room temperature under aerobic conditions. Mg^{2+} incorporation widens the band gap of the ZnO colloids much more than quantum confinement does by removal of the equivalent number of Zn^{2+} cations. In all other regards, Mg^{2+} substitution appears to have very similar effects as quantum confinement on the physical properties of these nanocrystals. Analysis of the trap luminescence of $Zn_{1-x}Mg_xO$ nanocrystals and the midgap $ML_{CB}CT$ transitions of $Zn_{0.98-x}Mg_xMn_{0.02}O$ nanocrystals shows that band gap widening with x involves increasing the conduction band potential and lowering the valence-band potential in a ratio of $\Delta E_{CB}:\Delta E_{VB} = 0.68:0.32$. Photodoping yields colloidal *n*-type $Zn_{1-x}Mg_xO$ nanocrystals, whose EPR g values agree well with those of colloidal *n*-type ZnO nanocrystals having the same energy gap.

Charging mixtures of ZnO and $Zn_{1-x}Mg_xO$ nanocrystals under conditions where electron transfer can proceed to equilibrium was used to reveal which nanocrystals have more negative conduction-band potentials, and larger ($d \approx 4.0$ nm) *n*-type $Zn_{0.75}Mg_{0.25}O$ nanocrystals were demonstrated to be better reductants than smaller ($d \approx 2.9$ nm) *n*-type ZnO nanocrystals, despite less quantum confinement in the former. Finally, these data show that the visible trap luminescence can be used as a valuable probe of the conduction-band potentials of $Zn_{1-x}Mg_xO$ nanocrystals at various diameters and values of x. Collectively, these results demonstrate that Mg^{2+} substitution is valuable for tuning the physical and chemical properties of colloidal ZnO-based semiconductor nanocrystals, broadening the range of chemical properties accessible with these unusual colloidal reductants. Future studies of these colloidal *n*-type nanocrystals as chemical reductants can be expected to yield important fundamental insights into both inter-nanocrystal and nanocrystal-molecule spontaneous electron transfer reactions relevant to a broad variety of catalytic and energy conversion technologies.

2.5 Notes to Chapter 2

(1) Cohn, A. W.; Kittilstved, K. R.; Gamelin, D. R. *J. Am. Chem. Soc.* **2012**, *134*, 7938.
(2) Haase, M.; Weller, H.; Henglein, A. *J. Phys. Chem.* **1988**, *92*, 482.
(3) Shim, M.; Guyot-Sionnest, P. *J. Am. Chem. Soc.* **2001**, *123*, 11651.
(4) Liu, W. K.; Whitaker, K. M.; Kittilstved, K. R.; Gamelin, D. R. *J. Am. Chem. Soc.* **2006**, *128*, 3910.
(5) Liu, W. K.; Whitaker, K. M.; Smith, A. L.; Kittilstved, K. R.; Robinson, B. H.; Gamelin, D. R. *Phys. Rev. Lett.* **2007**, *98*, 186804.
(6) Whitaker, K. M.; Ochsenbein, S. T.; Polinger, V. Z.; Gamelin, D. R. *J. Phys. Chem. C.* **2008**, *112*, 14331
(7) Whitaker, K. M.; Ochsenbein, S. T.; Smith, A. L.; Echodu, D. C.; Robinson, B. H.; Gamelin, D. R. *J. Phys. Chem. C* **2010**, *114*, 14467.
(8) Hayoun, R.; Whitaker, K. M.; Gamelin, D. R.; Mayer, J. M. *J. Am. Chem. Soc.* **2011**, *133*, 4228.
(9) van Dijken, A.; Mulenkamp, E. A.; Vanmaekelbergh, D.; Meijerink, A. *J. Phys. Chem. B* **2000**, *104*, 4355.
(10) Wood, A.; Giersig, M.; Mulvaney, P. *J. Phys. Chem. B* **2001**, *105*, 8810.

(11) Subramanian, V.; Wolf, E. E.; Kamat, P. V. *J. Phys. Chem. B* **2003**, *107*, 7479.

(12) Germeau, A.; Roest, A. L.; Vanmaekelbergh, D.; Allan, G.; Delerue, C.; Meulenkamp, E. A. *Phys. Rev. Lett.* **2003**, *90*, 097401.

(13) Hoyer, P.; Weller, H. *J. Phys. Chem.* **1995**, *99*, 14096.

(14) Mohamed, H. H.; Mendive, C. B.; Dillert, R.; Bahnemann, D. W. *J. Phys. Chem. A* **2011**, *114*, 2139.

(15) Johnson, C. A.; Cohn, A.; Kaspar, T. C.; Chambers, S. A.; Salley, G. M.; Gamelin, D. R. *Phys. Rev. B: Condens. Matter* **2011**, *84*, 125203.

(16) Johnson, C. A.; Kittilstved, K. R.; Kaspar, T. C.; Droubay, T. C.; Chambers, S. A.; Salley, G. M.; Gamelin, D. R. *Phys. Rev. B: Condens. Matter* **2010**, *82*, 115202.

(17) Zippel, J.; Heitsch, S.; Stölzel, M.; Müller, A.; von Weckstern, H.; Benndorf, G.; Lorenz, M.; Hochmuth, H.; Grundmann, M. *J. Lumin.* **2010**, *130*, 520.

(18) Gruber, T.; Krichner, C.; Kling, R.; Reuss, F.; Waag, A. *Appl. Phys. Lett.* **2004**, *84*, 5359.

(19) Lange, M.; Dietrich, C. P.; Zuniga-Perez, J.; von Wenckstern, H.; Lorenz, M.; Grundmann, M. *J. Vac. Sci. Technol., A* **2011**, *29*, 03A104.

(20) Park, W. I.; Yi, G.-C.; Kim, M. Y.; Pennycook, S. J. *Adv. Mater.* **2003**, *15*, 526.

(21) Gimenez, A. J.; Yáñez-Limón, J. M.; Seminario, J. M. *J. Phys. Chem. C.* **2010**, *115*, 282.

(22) Yu, P.; Tang, Z. K.; Wong, G. K. L.; Kawasaki, M.; Ohtomo, A.; Koinuma, H.; Segawa, Y. *Solid State Commun.* **1997**, *103*, 459.

(23) Ohtomo, A.; Kawasaki, M.; Koida, T.; Masubuchi, K.; Koinuma, H.; Sakurai, Y.; Yoshida, Y.; Yasuda, T.; Segawa, Y. *Appl. Phys. Lett.* **1998**, *72*, 2466.

(24) Chiou, J. W.; Tsai, H. M.; Pao, C. W.; Krishna Kumar, K. P.; Ray, S. C.; Chien, F. Z.; Pong, W. F.; Tsai, M.-H.; Chen, C.-H.; Lin, H.-J.; Wu, J. J.; Yang, M.-H.; Liu, S. C.; Chiang, H. H.; Chen, C. W. *Appl. Phys. Lett.* **2006**, *89*, 043121.

(25) Su, S. C.; Lu, Y. M.; Zhang, Z. Z.; Shan, C. X.; Li, B. H.; Shen, D. Z.; Yao, B.; Zhang, J. Y.; X., Z. D.; Fan, X. W. *Appl. Phys. Lett.* **2008**, *93*, 082108.

(26) Minemoto, T.; Negami, T.; Nishiwaki, S.; Takakura, H.; Hamakawa, Y. *Thin Solid Films* **2000**, *372*, 173.

(27) Ding, R.; Xu, C.; Gu, B.; Shi, Z.; Wang, H.; Ba, L.; Xiao, Z. *J. Mater. Sci. Technol.* **2010**, *26*, 601.

(28) Wang, Y. S.; Thomas, P. J.; O'Brien, P. *J. Phys. Chem. B* **2006**, *110*, 21412.

(29) Yang, Y.; Jin, Y.; He, H.; Wang, Q.; Tu, Y.; Lu, H.; Ye, Z. *J. Am. Chem. Soc.* **2010**, *132*, 13381.

(30) Shannon, R. D. *Acta Crystallogr. Sect. A: Found. Crystallogr.* **1976**, *32*, 751.

(31) Heitsch, S.; Zimmerman, G.; Fritsch, D.; Sturm, C.; Schmidt-Grund, R.; Schulz, C.; Hochmuth, H.; Spermann, D.; Benndorf, G.; Rheinländer, B.; Nobis, T.; Lorenz, M.; Grundmann, M. *J. Appl. Phys.* **2007**, *101*, 083521.

(32) Shan, F. K.; Kim, B. I.; Liu, G. X.; Liu, Z. F.; Sohn, J. Y.; Lee, W. J.; Shin, B. C.; Yu, Y. S. *J. Appl. Phys.* **2004**, *95*, 4772.

(33) Schwartz, D. A.; Norberg, N. S.; Nguyen, Q. P.; Parker, J. M.; Gamelin, D. R. *J. Am. Chem. Soc.* **2003**, *125*, 13205.

(34) Norberg, N. S.; Kittilstved, K. R.; Amonette, J. E.; Kukkadapu, R. K.; Schwartz, D. A.; Gamelin, D. R. *J. Am. Chem. Soc.* **2004**, *126*, 9387.

(35) West, A. R. *Solid State Chemistry and Its Applications*; John Wiley and Sons: New York, 1992.

(36) Meulenkamp, E. A. *J. Phys. Chem. B* **1998**, *102*, 5566.

(37) Wood, A.; Giersig, M.; Hilgendorff, M.; Vilas-Campos, A.; Liz-Marzán, L. M.; Mulvaney, P. *Aust. J. Chem.* **2003**, *56*, 1051.
(38) Norberg, N. S.; Gamelin, D. R. *J. Phys. Chem. B* **2005**, *109*, 20810.
(39) Olson, D. C.; Shaheen, S. E.; White, M. S.; Mitchell, W. J.; van Hest, M. F. A. M.; Collins, R. T.; Ginley, D. S. *Adv. Funct. Mater.* **2007**, *17*, 264.
(40) Vanheusden, K.; Warren, W. L.; Seager, C. H.; Tallant, D. R.; Voigt, J. A.; Gnade, B. E. *J. Appl. Phys.* **1996**, *79*, 7983.
(41) Leiter, F. H.; Alves, H. R.; Hofstaetter, A.; Hofmann, D. M.; Meyer, B. K. *Phs. Stats Solidi B* **2001**, *226*, R4.
(42) van Dijken, A.; Meulenkamp, E. A.; Vanmaekelbergh, D.; Meijerink, A. *J. Lumin.* **2000**, *90*, 123.
(43) van Dijken, A.; Makkinje, J.; Meijerink, A. *J. Lumin.* **2001**, *92*, 323.
(44) Hsu, N. E.; Hun, W. K.; F., C. Y. *J. Appl. Phys.* **2004**, *96*, 4671.
(45) Matsumoto, T.; Kato, H.; Miyamoto, K.; Sano, M.; Zhukov, E. A.; Yao, T. *Appl. Phys. Lett.* **2002**, *81*, 1231.
(46) Zhou, H.; Alves, H.; Hofmann, D. M.; Kriegseis, W.; Meyer, B. K.; Kaczmarczyk, G.; Hoffmann, A. *App. Phys. Lett.* **2002**, *80*, 210.
(47) Bohle, D. S.; Spina, C. J. *J. Am. Chem. Soc.* **2007**, *129*, 12380.
(48) Bohle, D. S.; Spina, C. J. *J. Am. Chem. Soc.* **2009**, *131*, 4397.
(49) Qui, X.; Li, L.; Zheng, J.; Liu, J.; Sun, X.; Li, G. *J. Phys. Chem. C.* **2008**, *112*, 12242.
(50) Zhang, X. D.; Guo, M. L.; Liu, C. L.; Zhang, L. A.; Zhang, W. Y.; Ding, Y. Q.; Wu, Q.; Feng, X. *Eur. Phys. J. B.* **2008**, *62*, 417.
(51) Feng, Y.; Badaeva, E.; Gamelin, D. R.; Li, X. *J. Phys. Chem. Lett.* **2010**, *1*, 1927.
(52) Badaeva, E.; May, J. W.; Ma, J.; Gamelin, D. R.; Li, X. *J. Phys. Chem. C* **2011**, *115*, 20986.
(53) Dietl, T. *Phys. Rev. B* **2008**, *77*, 085208.
(54) Sokolov, V. I.; Druzhinin, A. V.; Gruzdev, N. B.; Dejneka, A.; Churpita, O.; Hubicka, Z.; Jastrabik, L.; Trepakov, V. *Phys. Rev. B* **2010**, *81*, 153104.
(55) Kittilstved, K. R.; Liu, W. K.; Gamelin, D. R. *Nature Materials* **2006**, *5*, 291.
(56) Norberg, N. S.; Dalpian, G. M.; Chelikowsky, J. R.; Gamelin, D. R. *Nano Lett.* **2006**, *6*, 2887.
(57) Langer, J. M.; Delerue, C.; Lannoo, M.; Heinrich, H. *Phys. Rev. B* **1988**, *38*, 7723.
(58) Caldas, M. J.; Fazzio, A.; Zunger, A. *App. Phys. Lett.* **1984**, *45*, 671.
(59) Orlinskii, S. B.; Schmidt, J.; Baranov, P. G.; Hofmann, D. M.; de Mello Donegá, C.; Meijerink, A. *Phys. Rev. Lett.* **2004**, *92*, 047603.
(60) Orlinskii, S. B.; Schmidt, J.; Groenen, E. J. J.; Baranov, P. G.; de Mello Donegá, C.; Meijerink, A. *Phys. Rev. Lett.* **2005**, *94*, 097602.
(61) Orlinskii, S. B.; Schmidt, J.; Baranov, P. G.; Lorrmann, V.; Riedel, I.; Rauh, D.; Dyakonov, V. *Phys. Rev. B* **2008**, *77*, 115334.
(62) Ochsenbein, S. T.; Feng, Y.; Whitaker, K. M.; Badaeva, E.; Liu, W. K.; Li, X.; Gamelin, D. R. *Nature Nanotech.* **2009**, *4*, 681.
(63) Wassner, T. A.; Laumer, B.; Althammer, M.; Goennenwein, S. T. B.; Stutzmann, M.; Eickhoff, M.; Brandt, M. S. *Appl. Phys. Lett.* **2010**, *97*, 092102.

Chapter 3: Photodoping ZnO Nanocrystals: Picosecond Hole Capture, Electron Accumulation, and Auger Recombination

Photodoping of colloidal ZnO nanocrystals has been studied using continuous-wave and time-resolved photoluminescence spectroscopies in conjunction with EPR spectroscopy. Experiments have been performed with and without addition of alcohols as hole quenchers, focusing on ethanol. Both aerobic and anaerobic conditions have been examined. We find that ethanol quenches valence-band holes within ~15 ps of photoexcitation, but does not quench the trapped holes responsible for the characteristic visible photoluminescence of ZnO nanocrystals. Hole quenching yields ”charged” nanocrystals containing excess conduction-band electrons. The extra conduction-band electrons quench visible trap-centered luminescence via a highly effective electron/trap-state Auger-type cross-relaxation process. This Auger process is prominent even under aerobic photoexcitation conditions, particularly when samples are not stirred. Charging also reduces exciton nonradiative decay rates, resulting in increased UV luminescence. The dependence of charging on ethanol concentration and the reduced exciton nonradiative decay rates of charged ZnO nanocrystals are discussed. Finally, the results here provide a kinetic basis for understanding photochemical electron accumulation in colloidal ZnO nanocrystals. This work was done with Dr. Nils Janßen and in collaboration with Dr. James Mayer and was previously published in Ref. 1

3.1 Introduction

The physical properties of colloidal semiconductor nanocrystals are radically transformed when "extra" electrons or holes are introduced into their band levels. In the optical spectroscopy, three characteristic changes typically result from nanocrystal photodoping:[2-9] (*i*) a bleach of the excitonic absorption, (*ii*) appearance of new near-IR absorption of comparable intensity, and (*iii*) a reduction of the excitonic photoluminescence (PL) quantum yield because of rapid non-radiative Auger recombination. In magnetic experiments, the spins of the extra charge carriers in colloidal nanocrystals give rise to new EPR features[10-13] and can be used to mediate long-range exchange coupling between distant magnetic impurity ions.[14] In transport measurements, carrier mobilities within quantum-dot films are extremely sensitive to the extent of level filling.[8,15] Reduced colloidal nanocrystals also constitute powerful chemical reductants with tunable potentials that may be useful for driving interesting redox reactions.[16-18]

Colloidal semiconductor nanocrystals of many types have been charged using electrochemical techniques,[5,6,8,9,19,20] chemical reductants,[2,4] and photodoping.[2,10-13,17,18,21-27] Among these, ZnO nanocrystals are exceptional in that charging *increases* rather than decreases their excitonic PL intensities.[21-23,27-29] Simultaneously, charging suppresses the prominent visible trap PL of ZnO nanocrystals.[23,24,26,29] The origins of these changes have not been concretely established, but have been postulated variously to involve a combination of increased radiative decay rates and electron trap filling with charging.[23,26,29] Although ethanol (EtOH) and related alcohols are frequently used as solvents in studies of ZnO nanocrystal PL, several groups have noted that photodoping is facilitated by use of such alcohols as hole scavengers.[2,10,11,21,23,26] Substantially more than one electron per ZnO nanocrystal can be introduced by UV irradiation in the presence of EtOH,[11,18,25] despite the anticipated fast Auger quenching,[24] and this apparent paradox has also not been explained.

Here, we describe the photophysics of colloidal ZnO nanocrystals related to the use of alcohols as hole scavengers, focusing on EtOH. Continuous-wave PL and EPR measurements following UV irradiation in the presence of EtOH allow correlation of the visible PL quenching with the appearance of the $g = 1.96$ EPR signal associated with delocalized conduction band electrons in colloidal ZnO nanocrystals,[11,12] *i.e.*, with nanocrystal charging. Time-resolved PL measurements reveal that EtOH does not quench the visible emissive trap state directly, but instead captures valence-band-like holes prior to formation of the emissive trap state. Hole capture by EtOH is extremely fast, taking place within 15 ps, implicating pre-adsorption of EtOH at the nanocrystal surfaces. Hole capture by EtOH is much faster than trion Auger recombination, allowing photochemical accumulation of multiple "extra" electrons.

We also describe the photophysics of the charged ZnO nanocrystals themselves. Time-resolved measurements reveal that the visible PL of the charged nanocrystals is quenched by electron/trap-state Auger de-excitation, a process that has not been identified previously in ZnO nanocrystals. Formation of charged ZnO nanocrystals by UV excitation is remarkably facile, such that sample stirring has a pronounced effect on the visible PL of even aerobic colloidal suspensions. Overall, these results clarify the photophysical processes leading to colloidal ZnO nanocrystal charging, as well as the spectroscopic properties of the charged ZnO nanocrystals themselves.

3.2 Experimental

3.2.A Synthesis and photochemical charging. Colloidal ZnO nanocrystals were synthesized using a base-initiated hydrolysis/condensation reaction introduced previously.[30] Briefly, 1.6 equivalents of 0.5 M tetramethylammonium hydroxide in EtOH were added dropwise to a 0.1 M solution of zinc acetate in dimethylsulfoxide. The reaction was stopped by precipitation of the nanocrystals with ethyl acetate. The nanocrystals were then suspended in EtOH and washed with heptane before being capped with dodecylamine (DDA).[31] The nanocrystals were capped by suspension in neat dodecylamine (DDA) and heating at 180 °C in air for 15 to 30 minutes, or suspended in neat DDA and degassed at 100 °C degrees before heating at 180 °C for 24 hours.

After capping, the nanocrystals were precipitated with EtOH and resuspended in toluene. All ZnO nanocrystals described here have diameters $d \geq \sim 6$ nm, as estimated from the empirical relationship between diameter and energy gap[32] or determined by transmission electron microscopy (TEM). Visible PL quantum yields measured with a Hammamatsu integrating sphere were typically 30-50% for these colloidal nanocrystals prior to photodoping. All experiments were performed on dodecylamine-capped ZnO nanocrystals suspended in toluene at nanocrystal concentrations in the μM range. Nanocrystal concentrations were estimated using a literature molar extinction coefficient for ZnO nanocrystals.[33] Anaerobic samples were prepared by loading degassed colloidal suspensions into a sealable luminescence cuvette or quartz EPR tube under the inert atmosphere of a glovebox. Photodoping of anaerobic samples was accomplished by irradiating the entire sample with the collimated output of a Xe arc photolysis lamp (~880 mW/cm^2), filtered by a concentrated aqueous solution of $CuSO_4 \cdot 4H_2O$ to avoid sample heating. For the data presented here, samples were charged by UV irradiation for up to ~45 min. Charging levels were estimated using the molar extinction coefficient of 8820 M^{-1} cm^{-1} per electron at 2000 nm obtained from similar nanocrystals (d = 10 nm) by titration against the oxidant $[FeCp^*_2][BAr_F]$ ($[FeCp^*_2]^+$ = decamethylferrocenium, $[BAr_F]^-$ = tetrakis[3,5-bis(trifluoromethyl)phenyl]borate).[34]

3.2B Physical measurements. Photoluminescence data were recorded in both continuous-wave (CW) and time-resolved (TR) modes. CW PL data were collected using the 330 nm output of a dispersed tungsten-halogen lamp for excitation and a 0.5 m single-grating monochromator equipped with a nitrogen-cooled CCD for detection. All luminescence spectra have been corrected for the response of the monochromator/CCD. TRPL data were collected using the 350 nm output of a frequency-doubled mode-locked Ti:Sapphire femptosecond oscillator with a repetition rate controlled using a pulse picker. For visible TRPL measurements, a 100 kHz repetition rate was used, and for UV PL measurements a 4 MHz repetition rate was used. TRPL data were recorded using a streak camera combined with a single-grating monochromator. The pulse duration and instrument response function were ~150 fs and ~15 ps, respectively. In some cases, quasi-CW PL spectra were measured concurrently with TR data using a second, perpendicular spectrometer. For PL measurements, average excitation power densities were kept low (typically <100 mW/cm^2 in pulsed measurements and <10 mW/cm^2 in CW measurements) and exposure times for anaerobic measurements were kept small (typically 4 seconds for CWPL and 3 minutes total integration time for TRPL) to minimize in-situ photodoping. EPR spectra were collected using a Bruker EMX X-band spectrometer. Electronic absorption spectra were collected using a Cary 500 (Varian) spectrophotometer. TEM data were collected using a FEI Tecnai G2 F20 at the University of Washington Center for Nanotechnology User Facility.

3.3 Results and Analysis

3.3.A. Nanocrystal charging under anaerobic conditions Figure 3.1a shows representative CW PL spectra of colloidal ZnO nanocrystals excited at 330 nm. Before UV photolysis, the PL spectrum shows almost exclusively the characteristic trap-centered visible PL of ZnO nanocrystals. Under anaerobic conditions, extended UV irradiation causes this visible PL intensity to decrease and a near-edge UV PL band to grow in, consistent with previous observations.[23,27,29] These effects have been interpreted as implicating nanocrystal charging with excess electrons following hole scavenging by the alcohol.[23,26,27,29,35]

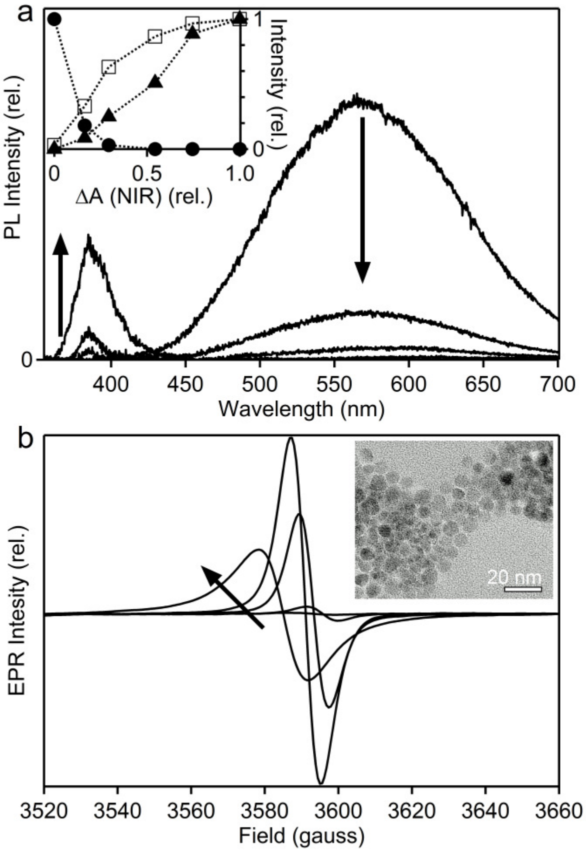

Figure 3.1. **(a)** CW PL spectra of an anaerobic toluene suspension of ZnO nanocrystals (2.1 μM, *d* = 9 nm) collected after various UV irradiation times in the presence of excess EtOH (0 to 45 minutes). The arrows show the direction of increased charging. **(b)** EPR spectra of the same sample at the same stages of UV irradiation as shown in (a). The inset to (a) plots relative EPR (open squares, double integrated), visible PL (closed circles), and UV PL (closed triangles) intensities as a function of nanocrystal charging as represented by the increase in near-IR absorbance (ΔA) integrated between 1940 nm and 2080 nm. The inset to (b) shows a TEM image of these nanocrystals.

Figure 3.1b plots EPR spectra collected at the same stages of irradiation. A $g \approx 1.96$ resonance is observed that increases in intensity and shifts to lower field (larger *g*) with continued irradiation, again consistent with previous reports.[11] This EPR signal has been identified as that of delocalized conduction-band electrons in colloidal ZnO nanocrystals.[11-13] The inset to Fig. 3.1a plots visible and UV PL intensities as well as EPR intensities vs relative change in near-IR absorbance (ΔA_{rel}). The highest charging level shown in Fig. 3.1 is estimated to correspond to an average of approximately 16 electrons/nanocrystal, albeit with some uncertainty because of the indirect method of determination (see Experimental). A detailed study of maximum photochemical charging levels is reported elsewhere.[36] As shown below, the quenching of all visible PL at ΔA_{rel} ~ 0.25 in Fig. 3.1a implies that essentially all nanocrystals possess at least one "extra" electron at this stage (see Discussion). The continued increase of the EPR intensity beyond this point is consistent with accumulation of multiple CB electrons per nanocrystal.[11,18,25] The UV PL intensity also continues to increase beyond ΔA_{rel} ~ 0.25, in approximately linear proportion with ΔA_{rel}.

Figure 3.2a shows time-resolved visible PL data collected from a stirred anaerobic suspension of ZnO nanocrystals as a function of UV excitation time. The uncharged nanocrystals show a multiexponential decay that is fitted reasonably well by two time constants, τ_1 ~ 200 ns and τ_2 ~ 1.8 μs, with the slow component constituting ~90% of the amplitude. Such biphasic decay is characteristic of ZnO nanocrystal trap emission.[37] Although charging reduces the visible PL intensities, normalizing these data at long times yields superimposable curves on the μs timescale (dashed), indicating that only the early decay dynamics are affected by the extra electrons. In these data, the early dynamics are masked by the instrument response function, so PL data were therefore collected on a faster timescale. Figure 3.2b plots visible PL intensities measured over the first 10 ns following a 150 fs excitation pulse. The uncharged nanocrystals show a simple decay curve with an initial time constant of ~4.5 ns. Upon photodoping, a faster decay process emerges with a time constant of ~0.3 ns (this feature is even already faintly evident before deliberate photodoping, as a result of in situ charging by the low-power PL excitation source). This fast process is attributed to Auger-like de-excitation of this emissive excited state, involving nonradiative energy transfer from the emissive trap state to the extra electron (Fig. 3.2a, inset). Whereas Auger recombination of trions in ZnO nanocrystals has been observed at cryogenic temperatures,[29] Auger processes involving the emissive midgap trap state have not previously been reported. This Auger process is discussed in more detail in Section 3.2.C.

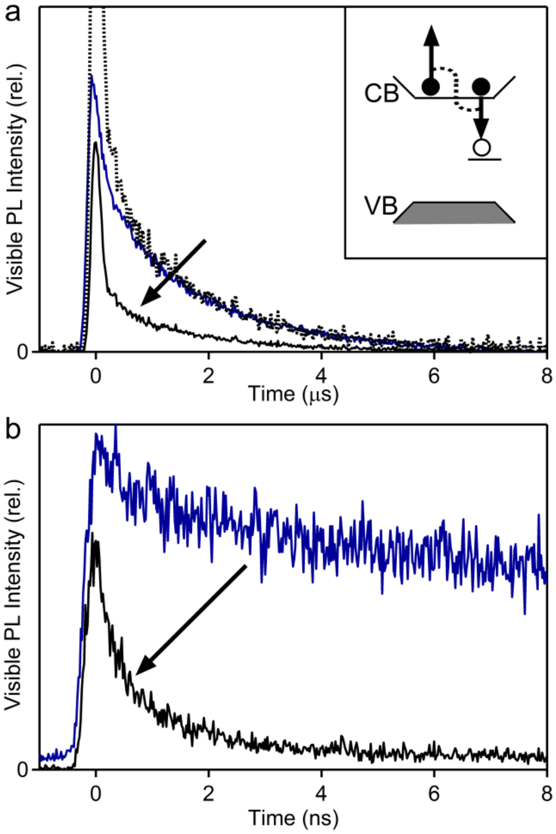

Figure 3.2. **(a)** Decay of the visible PL of a stirred anaerobic solution of ZnO nanocrystals (1.5 μM, *d* = 9 nm) in the presence of excess EtOH, measured before and after UV irradiation. The dotted curve shows the PL decay of the UV irradiated nanocrystals normalized to the PL intensity of the uncharged nanocrystals at 2 μs, illustrating that the slow decay component is unchanged. The inset illustrates the Auger de-excitation of visible trap luminescence schematically. **(b)** PL decay curves for the same solutions under the same excitation conditions as (a) but measured on a fast time scale. The arrows indicate the direction of increased photodoping.

Figure 3.3 shows time-resolved UV PL data at various stages of UV excitation. With UV irradiation, the average UV PL intensity increases (Fig. 3.1), and the time-resolved PL data reveal that the UV decay time increases, too, from ~20 to nearly 90 ps over this range (Fig. 3.3, inset). Charging ZnO nanocrystals with electrons thus elongates exciton recombination times, a change that can only arise from retardation of nonradiative decay of this excited state. Although the nanocrystals are charged, there is no evidence of any electron-exciton Auger recombination under these conditions. The UV PL decay times measured here are much shorter than typical trion Auger recombination times in colloidal semiconductor nanocrystals.[38] For ZnO nanocrystals, trion Auger recombination has only been reported at 20 K, where UV PL decay times decrease from ~260 ps to ~150 ps upon charging.[29] Auger recombination may govern trion decay rates at cryogenic temperatures, but other faster nonradiative processes evidently dominate at room temperature, and the data in Fig. 3.3 show that *these nonradiative processes become less effective with charging*.

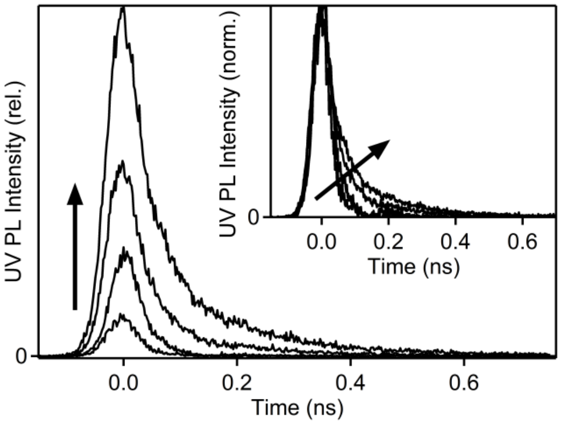

Figure 3.3. Time-resolved UV PL from a stirred anaerobic suspension of ZnO nanocrystals (0.05 μM, d = 9 nm) with excess EtOH at increasing charging levels (arrow). Inset: The same data, normalized at t = 0 ns to emphasize the increasing UV PL decay time with charging.

3.3.B. Photooxidation of ethanol under aerobic conditions Previous work has demonstrated quenching of photoexcited ZnO nanocrystal PL by many hole scavengers (*e.g.*, catechol, I^-, *etc.*,).[21,22,39,40] In those experiments, visible PL was quenched by stoichiometric quantities of the quencher (*e.g.*, PL from μM ZnO NCs quenched by μM quencher). To our knowledge, a similar analysis of the photochemical reaction of ZnO nanocrystals with EtOH (or related alcohols) has not been reported, despite widespread use of EtOH with ZnO nanocrystals as a hole scavenger or even a solvent. It is substantially more difficult to remove an electron from EtOH than from most quenchers examined previously, and similar reactivity therefore cannot be assumed.

The above experiments were all performed anaerobically in the presence of EtOH, and the major observations relate to nanocrystals containing at least one extra electron. To probe the reaction of the photoexcited ZnO nanocrystals with EtOH without interference from already charged nanocrystals, parallel experiments were performed under *aerobic* conditions. Here, electrons do not accumulate because of facile nanocrystal re-oxidation by O_2.[2,4,10,23,26]

3.3.B.i CW photoluminescence. Figure 3.4a plots the CW PL spectra of an aerobic suspension of colloidal ZnO nanocrystals as a function of added EtOH. The visible PL intensity decreases with increasing EtOH concentration, but cannot be diminished beyond around half of its original value. Similar saturation is seen in every ZnO sample, but with a spread in the precise saturation magnitude and EtOH concentration. Similar results are also obtained with butanol or hexanol, but not with catechol, for which PL quenching occurs at quencher concentrations that are ~10^6 times smaller, agreeing well with literature results.[40] Turning off the stirring reduces the visible PL even further and will be discussed in Section 3.3.C.

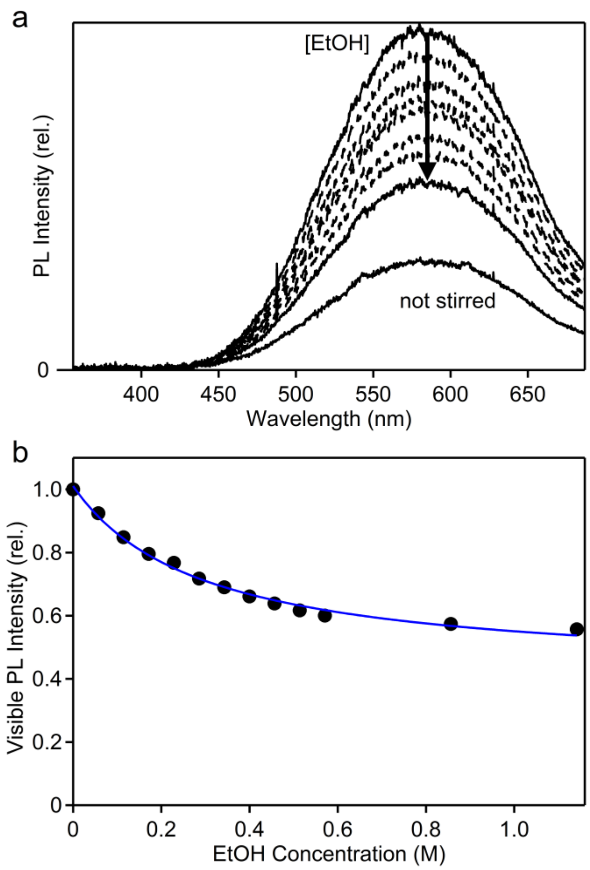

Figure 3.4. **(a)** CW photoluminescence spectra of a colloidal suspension of ZnO nanocrystals (0.04 µM, *d* = 6 nm) with constant stirring. This series of PL spectra was collected with sufficient EtOH added to make the solutions 0, 0.06, 0.11, 0.17, 0.23, 0.34, 0.46, and 1.1 M in EtOH. No correction was made for the 6% nanocrystal dilution over this series. The arrow indicates the direction of increasing EtOH concentration. Even at the highest EtOH concentration, the PL decreases further when sample stirring is stopped. **(b)** The integrated intensities from (a) plotted vs EtOH concentration. The solid curve shows the best fit to these data using the Langmuir isotherm model (eq 1), which yields $K = 3.4\ \mathrm{M}^{-1}$.

Figure 3.4b plots the relative visible PL intensities versus added EtOH. The PL decreases in proportion to added EtOH at small EtOH concentrations, but becomes independent of added EtOH at large concentrations. The asymptotic limit of ~50% quenching implies roughly equal hole-trapping (to form the luminescent state) and hole-quenching rates at saturation for this sample. These data suggest that the visible PL is not quenched by a simple diffusion-limited bimolecular reaction between this luminescent excited state and EtOH, but instead suggest pre-association of EtOH with ZnO, *i.e.*, EtOH behaves as a static quencher. Moreover, EtOH needs to be added in concentrations six orders of magnitude larger than the ZnO nanocrystal concentration to see appreciable quenching, or approximately three to six orders of magnitude larger than those of other quenchers that have been investigated. These data suggest that the photophysical mechanism by which EtOH quenches the trap PL is different from that operative with catechol (and likely also other substrates examined previously).[21,22,39,40]

Given the indications of pre-association, the data were analyzed using a simple Langmuir isotherm model.[41,42] For PL intensities I_0 and I_f at the initial and saturation limits of the EtOH titration, respectively, the PL intensity at an intermediate fractional surface coverage $0 \leq \theta \leq 1$ is described by I_θ in eq 3.1, assuming that PL quenching is proportional to adsorbed EtOH. A fit of the PL intensities from Fig. 3.4 to eq 3.1 is shown in Fig. 3.4b and yields a very small apparent association constant of K ~ 3.4 M^{-1}, confirming that EtOH interacts poorly with the ZnO nanocrystal surfaces. The microscopic nature of this adsorption remains unclear, but may possibly involve dissociative adsorption to form the surface-bound alkoxide.[43-46]

$$I_\theta = I_0 + \frac{K[Q](I_f - I_0)}{1 + K[Q]} \tag{3.1}$$

3.3.B.ii Time-resolved photoluminescence. Figure 3.5a shows the effect of EtOH on the visible PL decay dynamics under aerobic conditions. Prior to EtOH addition, the PL decay is multi-exponential over many decades, as described in section 3.3.A. EtOH reduces the visible PL intensity, but normalizing these data at any time point yields superimposable curves (Fig. 3.5b), indicating that the decay dynamics are not affected by EtOH on this timescale. This result rules out visible PL quenching by EtOH in a diffusion-limited bimolecular reaction, and supports the conclusion of quenching by adsorbed EtOH drawn above. In this result, EtOH clearly differs from catechol (and likely other quenchers that react at similar stoichiometric concentrations), which shows visible PL lifetime shortening in conjunction with visible PL intensity loss.[21,22,40,47-49]

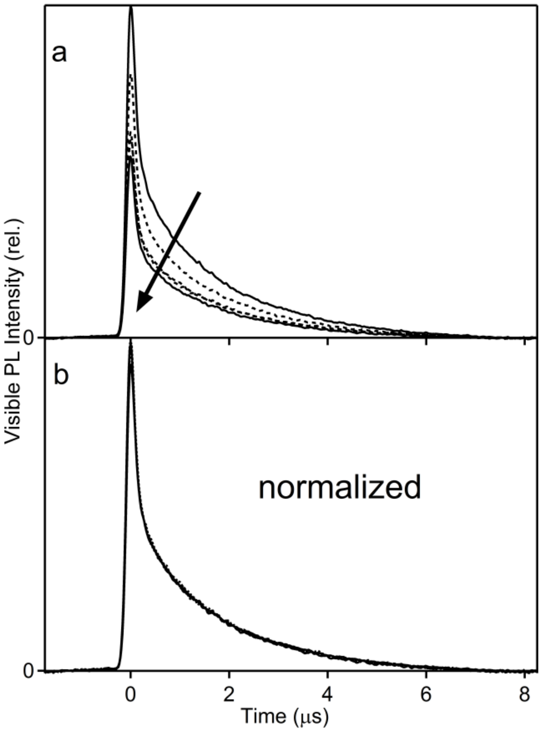

Figure 3.5. **(a)** Decay of the visible photoluminescence of a stirred suspension of ZnO nanocrystals (0.04 μM, *d* = 6 nm) as a function of added EtOH (0, 0.28, 0.57, 0.86, and 1.14 M). The arrow indicates the direction of increasing EtOH concentration. **(b)** The PL decay curves from (a), normalized at 2 μs.

Figure 3.6a shows time-resolved visible PL data measured on a faster timescale. The dashed curve represents the instrument response function. Although the PL does not noticeably decay over this short time window, EtOH addition diminishes its intensity. Figure 3.6b compares visible PL intensities from these data and quasi-CW spectra measured simultaneously. The good agreement between the two data sets confirms that visible PL quenching by EtOH occurs faster than our ~15 ps instrumental detection limit. A similarly fast rise time of near-IR transient absorption has been reported following UV photoexcitation of ZnO nanocrystals in the presence of EtOH, but was interpreted in terms of electron trapping times rather than hole scavenging times.[22] We believe those data are consistent with the present interpretation that holes are trapped within ~15 ps, whereas electrons remain delocalized and band-like.

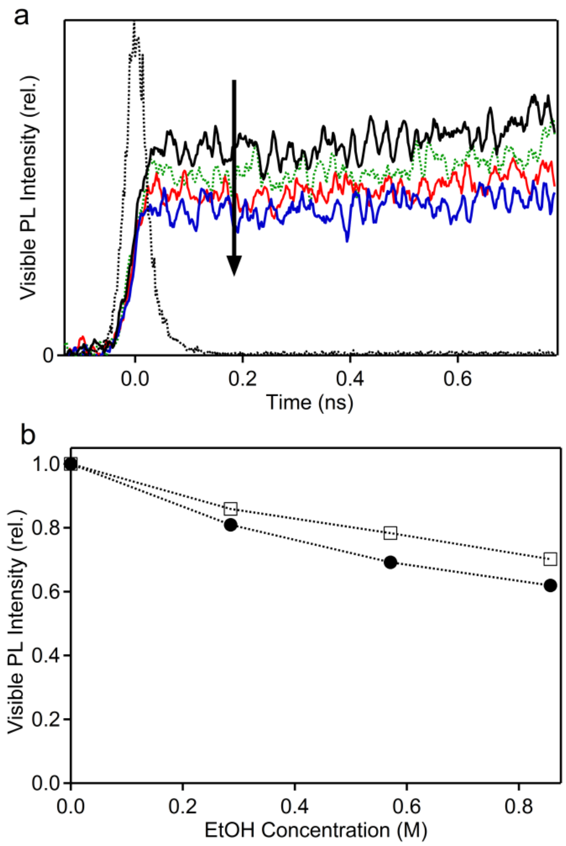

Figure 3.6. **(a)** Short-time visible-photoluminescence decay curves measured for a stirred suspension of ZnO nanocrystals (0.01 μM, *d* = 6.5 nm) as a function of added EtOH (0, 0.28, 0.57, and 0.86 M final EtOH concentrations). The arrow indicates the direction of increasing EtOH concentration. The dotted curve represents the instrument response function. **(b)** Relative PL intensities from the time traces in panel (a) (open squares) plotted vs solution EtOH concentration, compared with relative quasi-CW luminescence intensities measured simultaneously (closed circles).

From the data presented above, we conclude that (a) EtOH reacts with photoexcited ZnO nanocrystals to yield charged nanocrystals possessing CB-like electrons, (b) the reaction between photoexcited ZnO and EtOH is extremely fast (<15 ps) and therefore involves only adsorbed EtOH, and (c) the reaction takes place prior to formation of the luminescent midgap trap state, *i.e.*, EtOH quenches holes directly from the excitonic state.

3.3.C. Auger de-excitation. We now return to the observation in Fig. 3.4 that the visible trap PL of aerobic colloidal ZnO nanocrystals is sensitive to sample stirring, and specifically that its intensity decreases when stirring is stopped. In time-resolved PL measurements on the microsecond timescale (Fig. 3.7a), the intensity also decreases when stirring is stopped, but the shape of the decay curve does not change (Fig. 3.7b). Figure 3.7c plots parallel UV luminescence data collected with and without stirring. In contrast with the visible PL, the UV luminescence intensity *increases* when stirring is stopped. Figure 3.7d plots these data normalized at t = 0 ns, from which it is evident that the lifetime of the UV-emitting excited state increases when stirring is stopped, from ~17 to 30 ps. Figure 3.7e plots visible PL intensities of stirred and unstirred nanocrystal suspensions over the first 10 ns. For the stirred sample, a simple decay curve is observed with an initial time constant of ~7 ns. When the same sample is not stirred, a faster decay process emerges with a time constant of ~0.3 ns. The spectroscopic changes observed in aerobic ZnO suspensions without stirring closely resemble those observed upon nanocrystal charging (section 3.3.A), and we conclude that substantial transient charging still occurs even under these aerobic conditions.[50] Stirring sweeps these charged nanocrystals out of the excitation volume and accelerates mixing of solvated O_2. The precise effects of stirring depend on factors such as the excitation volume and its location within the cuvette, the excitation power density, the laser repetition rate, and of course the stirring parameters (dimensions of the stir bar, angular frequency, etc.).

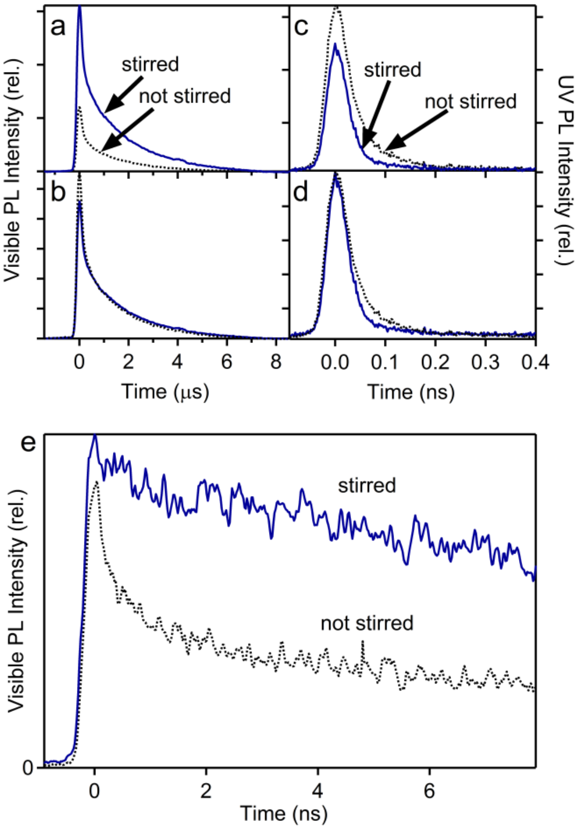

Figure 3.7. (a) Visible luminescence decay curves of an aerobic suspension of ZnO nanocrystals with (solid) and without (dotted) stirring (0.04 μM, *d* ~ 6.3 nm). **(b)** Curves from (a) normalized at 2 μs. **(c)** UV luminescence decay curves with and without stirring. **(d)** Curves from (c) normalized at 0 ns. **(e)** Visible PL decay curves from an aerobic suspension of ZnO nanocrystals, with (solid) and without (dotted) stirring.

As an independent test of this transient charging hypothesis, Fig. 3.8a plots visible PL decay curves measured for a stirred aerobic suspension of ZnO nanocrystals at various laser excitation powers up to 90 μW average power (0.9 nJ pulse energies). Increasing the excitation power leads to a rapid increase in the intensity of the same fast decay component seen in Fig. 3.7e. A global bi-exponential fit to these data yields $\tau_1 = 0.36$ ns and $\tau_2 = 4.0$ ns, where this τ_1 is very similar to the fast component observed upon charging ($\tau \sim 0.3$ ns, Fig. 3.2b). The fitting amplitudes are plotted vs laser power density in Fig. 3.8b. Both components can be fit to the power law in eq 3.2, where *A* is the amplitude, *c* is a scaling factor, *P* is the average excitation power density, and b describes the power of the relationship. The fast component shows an average $b = 1.35$ and the slower component shows an average $b = 0.71$. The super-linear power dependence of the fast component confirms its assignment to a two-photon process. The fact that $b < 2$ for this two-photon process reflects establishment of a sizable steady-state electron population within the excitation volume, and is analogous to the sub-quadratic power dependence observed in two-photon upconversion luminescence when intermediate-state decay rates are slow relative to excitation rates.[51,52] Importantly, the sum of the two components is linear with power ($b = 1$), demonstrating that the initial luminescent trap-state population is simply proportional to the number of excitation photons.

$$A = cP^{\mathrm{b}} \tag{3.2}$$

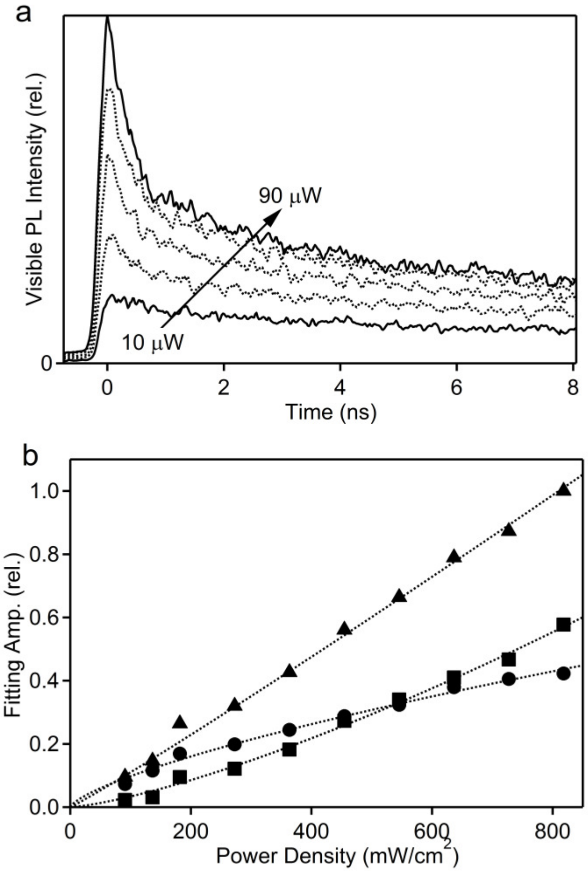

Figure 3.8. **(a)** Visible trap PL decay curves measured from a stirred aerobic suspension of ZnO nanocrystals without added ethanol (0.04 μM, *d* = 6 nm) as a function of laser excitation power. The arrow shows the direction of increasing laser power. **(b)** The fitting amplitudes from a global fit of the decay curves in (a) and additional powers not shown. The fitting amplitudes of the slow component (circles), fast component (squares), and the sum of fast and slow (triangles) are shown. This range of power densities corresponds to average powers of 0 - 90 μW, and pulse energies of 0 - 0.9 nJ.

Overall, we conclude a surprisingly high probability of exciting unintentionally charged ZnO nanocrystals, even under aerobic conditions and even without deliberate addition of hole scavengers. This probability is diminished with stirring. These observations are reminiscent of the effects of stirring on exciton recombination dynamics in colloidal chalcogenide nanocrystals investigated for multi-exciton generation,[53] except that in the present case the relevant process involves electron/trap-state Auger cross relaxation rather than trion Auger recombination.

3.4 Discussion

3.4.A Hole scavenging by EtOH and electron accumulation. Ethanol and related alcohols are common hole scavengers in oxide photochemistry. The photochemistry of UV-excited ZnO with aliphatic alcohols has been investigated extensively and is generally found to yield aldehyde (or ketone) photoproducts of selective alcohol oxidation,[54,55] as summarized in eq 3.3 for the reaction with EtOH,[25] where h^+ represents a photogenerated hole.

$$2h^+ + C_2H_5OH \rightarrow CH_3CHO + 2H^+ \tag{3.3}$$

Aldehyde formation has also been implicated in oxidative alcohol sensing by nanocrystalline ZnO.[56] Among aliphatic alcohols, primary alcohols have been reported as more readily photooxidized by ZnO than secondary or tertiary alcohols.[55] In addition to facile reversible adsorption, infrared and temperature programmed desorption studies have suggested that under some conditions such alcohols are capable of binding dissociatively at bare or hydroxylated ZnO surfaces to form OH and alkoxyl groups.[43-46] For the colloidal ZnO nanocrystals studied here, the surfaces are ligated by dodecylamine for compatibility with toluene, and EtOH is likely stabilized in this surfactant layer by the nanocrystal surface polarity. The protons liberated via eq 3.3 likely bind to the nanocrystal surfaces or intercalate into their internal volumes,[15,18,57,58] where they appear particularly effective at screening the charges of the excess electrons.[15,57,58] Imines have been detected as the major organic product resulting from photodoping of colloidal ZnO nanocrystals identical to the ones described here, attributed to condensation of the aldehydes with surface-capping amine ligands.[18] Here, we focus on clarifying the photodynamics of these ZnO nanocrystals in the presence of EtOH.

The key photophysical processes observed upon excitation of uncharged ZnO nanocrystals are summarized in Scheme 3.1. After photoexcitation, the photogenerated VB hole can localize at a deep trap (k_{trap}), be captured by EtOH (k_q), or recombine with the excited electron ($k_{ex} = k_{rad} + k_{nr}$, where k_{nr} represents nonradiative exciton recombination processes, omitted from Scheme 3.1 for clarity). Hole quenching by EtOH is faster than our experimental time-resolved PL detection limit of ~15 ps, yielding a lower-limit pseudo-first-order rate constant of $k_q \geq 0.07$ ps^{-1}. In contrast, the rate constant for ZnO visible-luminescence quenching by EtOH is negligibly small (Figs. 3.2 and 3.5). A major difference between EtOH and catechol is therefore that the former only reacts with the VB hole, whereas the latter can also be oxidized by the deeply trapped hole, which has a potential >1.0 V more negative than the VB edge. Nevertheless, hole capture by EtOH is sufficiently fast to compete with exciton decay (k_{ex} ~ 0.05 ps^{-1} at no charging in Figs. 3.3, 3.7), and charging is facile. In the saturation limit of high EtOH concentration, hole capture by EtOH and by the emissive trap site are approximately equally probable, resulting in only ~50% PL loss (Fig. 3.4), *i.e.*, $k_q = k_{trap} \geq 0.07$ ps^{-1} can be concluded.

Scheme 3.1

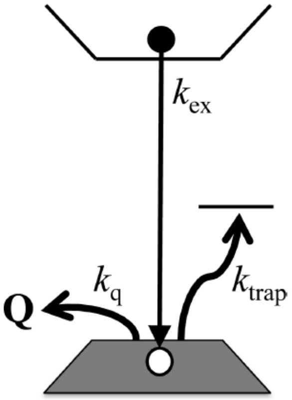

The rapidity of hole trapping by EtOH is significant in relation to the photochemical accumulation of multiple CB electrons per ZnO nanocrystal.[11,18,25] Generally, photodoped nanocrystals should be subject to rapid Auger recombination of the charged exciton, which should inhibit further photochemical charging.[4] Invoking the super-simple approximations of (*i*) additive Auger kinetics for each added electron (as found for quantum dot excitons, see ref. 59) and (*ii*) charge-independent k_q, the experimental trion Auger time of ~150 ps[29] and an upper-limit hole quenching time of k_q^{-1} ~ 15 ps would yield equivalent rates for photodoping and Auger recombination at ~10 electrons per ZnO nanocrystal. This analysis is clearly too simple to be quantitatively predictive; for example, the slowing of nonradiative exciton decay with charging (Fig. 3.2) also implies slower hole trapping by EtOH and hence actually disfavors electron accumulation (*vide infra*). Nevertheless, this analysis illustrates from a kinetic perspective how photochemical oxidation of EtOH can lead to multiple-electron accumulation in colloidal ZnO nanocrystals despite competing Auger processes.[55]

The rapidity of hole trapping by EtOH is also significant in that it allows photochemical charging of ZnO nanocrystals containing mid-gap electronic states from dopants (*e.g.*, Mn^{2+} or Co^{2+}), despite fast exciton localization at these dopants.[10,14] PL measurements at 20 K suggest an average exciton localization time of ~80 ps for ZnO nanocrystals containing a single Co^{2+} ion,[60] consistent with competitive hole trapping by EtOH even in such doped nanocrystals.

3.4.B Auger processes and the changes in visible and UV photoluminescence with charging.

Although visible PL quenching and UV PL enhancement in ZnO nanocrystals upon photochemical charging have been established,[21,23,29,61,62] the mechanistic details underpinning these phenomena have not been fully unraveled. Previous observations have suggested that the first photogenerated electrons are consumed by deep electron traps associated with oxygen vacancies, and only subsequent photogenerated electrons are delocalized in the CB.[23,29] Specifically, photodoping has been suggested to reduce $V_O^{\bullet}$ defects (likely at surfaces) to form doubly occupied V_O^{x} centers.[23] In this scenario, charging suppresses the visible PL by eliminating $V_O^{\bullet}$ centers, which participate in that PL by trapping photogenerated holes to form

$V_O^{\bullet\bullet}$. Here, $V_O^{\bullet\bullet}$ recombination with e^-_{CB} would be emissive, but $V_O^{\bullet}$ recombination with e^-_{CB} would not.

This scenario is not entirely consistent with the results of Fig. 3.1 and prior EPR measurements.[11,12,16] EPR spectra collected before photochemical charging show no evidence of paramagnetic $V_O^{\bullet}$ defects, despite the prominent visible PL of these nanocrystals. The *g* values of the unpaired electrons formed upon photochemical charging are sensitive to quantum confinement, and hence delocalized over the entire volumes of the ZnO nanocrystals, inconsistent with deeply trapped electrons.[12] Cooling to liquid helium temperatures does not cause electron trapping.[11] EPR spin quantitation following thermal electron transfer between photochemically reduced ZnO nanocrystals and ZnO nanocrystals that have not been reduced shows that the electrons are transferred quantitatively from CB to CB, without loss to traps.[16] Extensive EPR studies thus show no evidence of $V_O^{\bullet}$ deep electron traps in these colloidal ZnO nanocrystals. Moreover, the data in Fig. 3.8 demonstrate that charging does not alter the probability of forming the emissive trap state upon photoexcitation, only the probability of radiative decay of that state. We conclude that extra electrons do not suppress the visible trap luminescence of ZnO nanocrystals by elimination of $V_O^{\bullet}$ traps, but instead suppress it by effective Auger de-excitation of the emissive excited state, as illustrated in the inset of Fig. 3.2a.

This electron/trap-state Auger de-excitation is extremely efficient, aided by the long intrinsic lifetime of this trap state. At the lowest charging levels in Fig. 3.8, the Auger time constant of 350 ps can be associated with one-electron occupancy. From the ratio of this one-electron Auger time constant to that of the major component of the visible PL decay (1.8 μs), one electron in a ZnO nanocrystal suppresses the visible PL from that nanocrystal by essentially 100%. Even accounting for the multi-exponential decay of the visible PL (Fig. 3.2), we estimate that one electron quenches over ~99% of the visible PL via this Auger de-excitation. This electron/trap-state Auger de-excitation is thus far more effective than typical trion or bi-exciton Auger recombination processes in semiconductor nanocrystals, a difference attributable almost entirely to the far longer radiative decay times of this visible trap PL than of excitons. In this regard, this electron/trap-state Auger process is analogous to the Auger de-excitation of long-lived Mn^{2+} excited states described in Mn^{2+}-doped CdS quantum dots.[63,64]

We now address how charging increases UV PL intensities. From studies of other colloidal quantum dots, radiative decay rate constants can be anticipated to approximately double in the trion relative to the exciton,[38] and such an increase has therefore been considered a possible source of the increased UV PL intensities of charged ZnO nanocrystals.[23] From the short UV PL decay times observed here (Fig. 3.3), however, we suggest that this increase in radiative decay rate constants is far too small to be responsible. Two additional details must also be taken into account: First, the UV PL quantum yields of colloidal ZnO nanocrystals are very small (typically < ~1%),[31,65] indicating that the observed UV decay dynamics are determined primarily by *nonradiative* processes, and second, the UV PL decay times are *elongated* upon charging (Fig. 3.3). We propose that the primary cause of UV PL enhancement upon charging is a slowing of nonradiative decay, rather than an acceleration of radiative decay.

Two possible mechanisms by which trion formation may retard nonradiative exciton decay are (*i*) hole stabilization relative to traps (Scheme 3.2, center),[23] or (*ii*) hole contraction into the nanocrystal core (Scheme 3.2, right).[66] Both effects might be anticipated from the hole's Coulomb interaction with the excess electron density, and both have the same net effect on hole trapping kinetics. The former reduces the hole-transfer driving force and number of accessible hole traps relative to uncharged nanocrystals (Scheme 3.2, left), thereby reducing k_{trap}. The latter reduces electronic coupling with surface hole traps (or EtOH), also reducing k_{trap}. Either or both of these mechanisms could be responsible for the elongated UV PL decay times of charged ZnO nanocrystals observed here.

Scheme 3.2

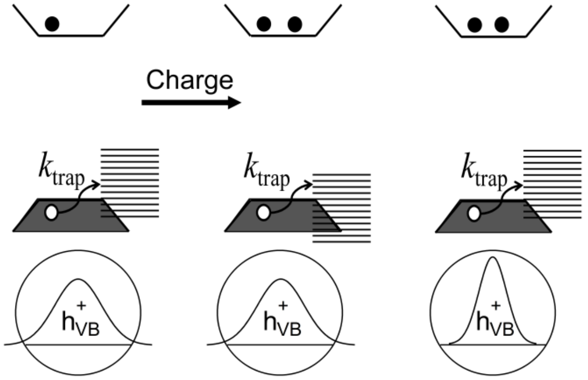

3.5 Conclusion

PL and EPR spectroscopies have been applied to elucidate the process of photodoping ZnO nanocrystals by UV irradiation in the presence of alcohol hole scavengers. EtOH reacts directly with VB holes within ~15 ps of photoexcitation, reducing visible PL intensities by intercepting the exciton prior to formation of the luminescent trap state. EtOH is unable to quench visible PL directly, and consequently shows quenching behavior qualitatively different from catechol and likely also other hole scavengers, which typically affect similar PL changes with 10^3 - 10^6 times smaller quencher concentrations.[21,22,39,40] Charged ZnO nanocrystals show reduced visible PL intensities because of Auger-type electron-trap cross relaxation. By this process, one electron is estimated to quench ~99% of the visible PL from a given nanocrystal. The increased UV PL with charging arises from retardation of nonradiative exciton decay, and two microscopic mechanisms have been described.

These results advance our understanding of the photophysics and photochemistry of ZnO nanocrystals in the presence of hole scavengers such as EtOH. They provide a kinetic basis for understanding how photodoping leads to electron accumulation,[11,18,25] and how photodoping of transition-metal-doped ZnO nanocrystals is successful.[10,14] They identify a new electron/trap-state Auger process that dominates the PL characteristics of charged nanocrystals. Finally, they show that transient charging can be observed even under aerobic conditions without deliberate addition of any hole scavenger, suggesting that Auger quenching of ZnO nanocrystal visible PL may be more prevalent than previously recognized.

3.6 Notes to Chapter 3

(1) Cohn, A. W.; Janssen, N.; Mayer, J. M.; Gamelin, D. R. *Journal of Physical Chemistry C* **2012**, *116*, 20633.
(2) Haase, M.; Weller, H.; Henglein, A. *J. Phys. Chem.* **1988**, *92*, 482.
(3) Hoyer, P.; Weller, H. *Chem. Phys. Letters* **1994**, *221*, 379.
(4) Shim, M.; Guyot-Sionnest, P. *Nature* **2000**, *407*, 981.
(5) Wang, C.; Shim, M.; Guyot-Sionnest, P. *Science* **2001**, *291*, 2390.
(6) Roest, A. L.; Kelly, J. J.; Vanmaekelbergh, D.; Meulenkamp, E. A. *Phys. Rev. Lett.* **2002**, *89*, 036801.
(7) Shim, M.; Guyot-Sionnest, P. *Phys. Rev. Lett.* **2003**, *91*, 169703.
(8) Yu, D.; Wang, C.; Guyot-Sionnest, P. *Science* **2003**, *300*, 1277.
(9) Guyot-Sionnest, P. *Microchim Acta* **2008**, *160*, 309.
(10) Liu, W. K.; Whitaker, K. M.; Kittilstved, K. R.; Gamelin, D. R. *J. Am. Chem. Soc.* **2006**, *128*, 3910.
(11) Liu, W. K.; Whitaker, K. M.; Smith, A. L.; Kittilstved, K. R.; Robinson, B. H.; Gamelin, D. R. *Phys. Rev. Lett.* **2007**, *98*, 186804.
(12) Whitaker, K. M.; Ochsenbein, S. T.; Polinger, V. Z.; Gamelin, D. R. *J. Phys. Chem. C* **2008**, *112*, 14331.
(13) Whitaker, K. M.; Ochsenbein, S. T.; Smith, A. L.; Echodu, D. C.; Robinson, B. H.; Gamelin, D. R. *J. Phys. Chem. C* **2010**, *114*, 14467.
(14) Ochsenbein, S. T.; Feng, Y.; Whitaker, K. M.; Badaeva, E.; Liu, W. K.; Li, X.; Gamelin, D. R. *Nature Nanotechnology* **2009**, *4*, 681.
(15) Roest, A. L.; Germeau, A.; Kelly, J. J.; Vanmaekelbergh, D.; Allan, G.; Meulenkamp, E. A. *Chem. Phys. Chem.* **2003**, *4*, 959.
(16) Hayoun, R.; Whitaker, K. M.; Gamelin, D. R.; Mayer, J. M. *J. Am. Chem. Soc.* **2011**, *133*, 4228.
(17) Cohn, A. W.; Kittilstved, K. R.; Gamelin, D. R. *J. Am. Chem. Soc.* **2012**, *134*, 7937.
(18) Schrauben, J. N.; Hayoun, R.; Valdez, C. N.; Braten, M.; Fridley, L.; Mayer, J. M. *Science* **2012**, *336*, 1298.
(19) Wehrenberg, B. L.; Guyot-Sionnest, P. *J. Am. Chem. Soc.* **2003**, *125*, 7806.
(20) Germeau, A.; Roest, A. L.; Vanmaekelbergh, D.; Allan, G.; Delerue, C.; Meulenkamp, E. A. *Physical Review Letters* **2003**, *90*, 097401.
(21) Bahnemann, D. W.; Kormann, C.; Hoffmann, M. R. *J. Phys. Chem.* **1987**, *91*, 3789.

(22) Kamat, P. V.; Patrick, B. *J. Phys. Chem.* **1992**, *96*, 6829.
(23) van Dijken, A.; Meulenkamp, E. A.; Vanmaekelbergh, D.; Meijerink, A. *Journal of Physical Chemistry B* **2000**, *104*, 4355.
(24) Shim, M.; Guyot-Sionnest, P. *J. Am. Chem. Soc.* **2001**, *123*, 11651.
(25) Wood, A.; Giersig, M.; Mulvaney, P. *Journal of Physical Chemistry B* **2001**, *105*, 8810.
(26) Subramanian, V.; Wolf, E. E.; Kamat, P. V. *Journal of Physical Chemistry B* **2003**, *107*, 7479.
(27) Stroyuk, O. L.; Dzhagan, V. M.; Shvalagin, V. V.; Kuchmiy, S. Y. *J. Phys. Chem. C* **2010**, *114*, 220.
(28) Hoyer, P.; Weller, H. *J. Phys. Chem.* **1995**, *99*, 14096.
(29) Yamamoto, S. *J. Phys. Chem. C* **2011**, *115*, 21635.
(30) Schwartz, D. A.; Norberg, N. S.; Nguyen, Q. P.; Parker, J. M.; Gamelin, D. R. *J. Am. Chem. Soc.* **2003**, *125*, 13205.
(31) Norberg, N. S.; Gamelin, D. R. *J. Phys. Chem. B* **2005**, *109*, 20810.
(32) Meulenkamp, E. A. *J. Phys. Chem. B* **1998**, *102*, 5566.
(33) Lommens, P.; Lambert, K.; Loncke, F.; Muynck, D. D.; Balkan, T.; Vanhaecke, F.; Vrielinck, H.; Callens, F.; Hens, Z. *Chem. Phys. Chem.* **2008**, *9*, 484.
(34) Schimpf, A. M.; Ochsenbein, S. T.; Buonsanti, R.; Milliron, D. J.; Gamelin, D. R. *Chem. Commun.* **2012**, in press.
(35) Lange, M.; Dietrich, C. P.; Zuniga-Perez, J.; von Wenckstern, H.; Lorenz, M.; Grundmann, M. *Journal of Vacuum Science and Technology* **2011**, *29*, 03A104.
(36) Schimpf, A. M.; Gunthardt, C., E.; Rinehart, J. D.; Mayer, J. M.; Gamelin, D. R. *Journal of the American Chemical Society* **2013**, *135*, 16569.
(37) van Dijken, A.; Meulenkamp, E. A.; Vanmaekelbergh, D.; Meijerink, A. *Journal of Physical Chemistry B* **2000**, *104*, 1715.
(38) Jha, P. P.; Guyot-Sionnest, P. *American Chemical Society Nano* **2009**, *3*, 1011.
(39) Kamat, P. V.; Huehn, R.; Nicolaescu, R. *J. Phys. Chem. B* **2002**, *106*, 788.
(40) Ramakrishna, G.; Ghosh, H. N. *Langmuir* **2003**, *19*, 3006.
(41) Bullen, C.; Mulvaney, P. *Langmuir* **2006**, *22*, 3007.
(42) Munro, A. M.; Ginger, D. S. *Nano Letters* **2008**, *8*, 2585.
(43) Nagao, M.; Morimoto, T. *J. Phys. Chem.* **1980**, *84*, 2054.
(44) Bowker, M.; Houghton, H.; Waugh, K. C. *J. Chem. Soc., Faraday Trans. 1* **1982**, *78*, 2573.
(45) Vohs, J. M.; Barteau, M. A. *Surf. Sci.* **1989**, *221*, 590.
(46) Kwak, G.; Yong, K. *J. Phys. Chem. C* **2008**, *112*, 3036.
(47) Yue, Q.; Cheng, J.; Li, G.; Zhang, K.; Zhai, Y.; Wang, L.; Liu, J. *Journal of Fluorescence* **2011**, *21*, 1131.
(48) Rabani, J.; Behar, D. *Journal of Physical Chemistry* **1989**, *93*, 2559.
(49) Bohle, D. S.; Spina, C. J. *J. Am. Chem. Soc.* **2009**, *131*, 4397.
(50) Shan, F. K.; Kim, B. I.; Liu, G. X.; Liu, Z. F.; Sohn, J. Y.; Lee, W. J.; Shin, B. C.; Yu, Y. S. *Journal of Applied Physics* **2004**, *95*, 4772.
(51) Pollnau, M.; Gamelin, D. R.; Lüthi, S. R.; Güdel, H. U.; Hehlen, M. P. *Phys. Rev. B* **2000**, *61*, 3337.
(52) Gamelin, D. R.; Güdel, H. U. *Topics in Current Chemistry* **2000**, *214*, 1.
(53) McGuire, J. A.; Sykora, M.; Joo, J.; Pietryga, J. M.; Klimov, V. I. *Nano Letters* **2010**, *10*, 2049.
(54) Cunningham, J.; Hodnett, B. K. *J. Chem. Soc., Faraday Trans. 1* **1981**, *77*, 2777.

(55) Markham, M. C.; Hannan, M. C.; Paternostro, R.; Rose, C. B. *J. Am. Chem. Soc.* **1958**, *80*, 5394.
(56) Xu, J.; Han, J.; Zhang, Y.; Sun, Y.; Xie, B. *Sens. Act. B* **2008**, *132*, 334.
(57) Roest, A. L.; Kelly, J. J.; Vanmaekelbergh, D. *Appl. Phys. Lett* **2003**, *83*, 5530.
(58) Roest, A. L.; Houtepen, A. J.; Kelly, J. J.; Vanmaekelbergh, D. *Faraday Discuss.* **2004**, *125*, 55.
(59) Klimov, V. I.; Mikhailovsky, A. A.; McBranch, D. W.; Leatherdale, C. A.; Bawendi, M. G. *Science* **2000**, *287*, 1011.
(60) Yamamoto, S. *J. Appl. Phys.* **2012**, *111*, 094310.
(61) Koch, U.; Fojtik, A.; Weller, H.; Henglein, A. *Chemical Physics Letters* **1985**, *122*, 507.
(62) Yamamoto, S.; Mishina, T. *J. Lumin.* **2011**, *131*, 620.
(63) White, M. A.; Weaver, A. L.; Beaulac, R.; Gamelin, D. R. *ACS Nano* **2011**, *5*, 4158.
(64) Peng, B.; Liang, W.; White, M. A.; Gamelin, D. R.; Li, X. *J. Phys. Chem. C* **2012**, *116*, 11223.
(65) Wood, A.; Giersig, M.; Hilgendorff, M.; Vilas-Campos, A.; Liz-Marzán, L. M.; Mulvaney, P. *Aust. J. Chem.* **2003**, *56*, 1051.
(66) Climente, J. I.; Bertoni, A.; Goldoni, G. *Phys. Rev. B* **2008**, *78*, 155316.

Chapter 4: Size-Dependent Trap-Assisted Auger Recombination in ZnO Nanocrystals

The acceleration of Auger-type multicarrier recombination in semiconductor nanocrystals impedes the development of many quantum-dot photonics, solar-cell, lighting, and lasing technologies. To date, only multiexciton and charged-exciton Auger recombination channels are known to show strong size dependence in nanocrystals. Here, we report the first observation of strongly accelerated "trap-assisted" Auger recombination rates in semiconductor nanocrystals. Trap-assisted Auger recombination in ZnO nanocrystals, involving the recombination of conduction-band electrons with deeply trapped holes via nonradiative energy transfer to extra conduction-band electrons, has been probed using time-resolved photoluminescence and transient absorption spectroscopies. We demonstrate that this trap-assisted Auger recombination accelerates dramatically with decreasing nanocrystal size, having recombination times of >1 ns in the largest nanocrystals but only ~80 ps in the smallest. These trap-assisted Auger recombination rates are shown to scale with inverse nanocrystal radius squared ($1/\tau_{\mathrm{Aug}} \sim R^{-2}$). Because surface carrier traps are ubiquitous in colloidal semiconductor nanocrystals, such fast trap-assisted Auger recombination is likely more prevalent in semiconductor nanocrystal photophysics than previously recognized. This work was previously published in ref.1 and was done in collaboration with Alina Schimpf and Carolyn Gunthardt.

4.1 Introduciton

Nonradiative Auger-type multicarrier recombination processes play prominent roles in the photophysics and device applications of semiconductors.[2,3] The acceleration of such processes in semiconductor nanocrystals has important ramifications for many nascent quantum-dot (QD) technologies.[4-6] Multicarrier Auger recombination is believed to determine threshold conditions of QD lasers[7,8] and charge-extraction efficiencies of QD solar cells involving multiexciton generation.[9-11] They have also been debated as participants in photoluminescence (PL) blinking.[4,12-16] To date, however, only two classes of size-dependent Auger recombination processes are documented in semiconductors: (*i*) multiexciton, and (*ii*) charged-exciton. Both share the common feature that all participating carriers are band-like. Here, we show that a third type of multicarrier Auger recombination is also strongly accelerated in semiconductor nanocrystals relative to bulk, namely trap-assisted Auger recombination. Whereas trap-assisted Auger recombination has long been investigated in bulk silicon photovoltaics and metal-insulator-semiconductor heterostructures,[2,17] its dependence on crystal size has never been examined. Because surface carrier traps are ubiquitous in semiconductor nanocrystals, the acceleration of trap-assisted Auger recombination may have broad implications in fundamental and applied QD research.

4.2 Experimental

4.2.A Synthesis Colloidal ZnO nanocrystals were synthesized by the room-temperature base hydrolysis/condensation reaction described in detail previously.[18,19] After washing with ethanol/heptane, the nanocrystals were heated in neat dodecylamine (DDA) to obtain the desired size. These DDA-capped nanocrystals were again washed with ethanol before suspending in toluene for optical measurements. Average nanocrystal radii were determined from their published empirical relationship with electronic absorption spectra (ref. 20, for $R < \sim 3.2$ nm) and from XRD line widths (for $R \geq \sim 3.2$ nm). Typical size distributions are ~±10-15% around the mean.

4.2.B Physical Measurements For all photoluminescence (PL) measurements (except as indicated), the nanocrystals were excited using the mode-locked frequency doubled output a

Ti:sapphire laser at 3.54 eV (350 nm, 150 fs pulse width, 0.4 nJ/pulse) limiting the smallest radius of ZnO nanocrystals that could be measured. For all measurements, the 76 MHz output of the Ti:sapphire laser was reduced to 100 kHz using a pulse picker. Time-resolved PL data were collected using a streak camera (instrument response time ~15 ps) mounted on a monochromator. Time-integrated measurements were collected simultaneously using a fiber optic and a second spectrometer. All spectra have been corrected for system response.

To ensure measurement of just the three-particle Auger rates, all Auger data were collected in the low-charging regime, where the average number of electrons per nanocrystal is near or below one. To achieve this regime, all Auger measurements of colloidal nanocrystals were performed without any deliberate photocharging, using just the in-situ UV excitation of the pulsed laser source and adventitious ethanol from the nanocrystal preparation procedure to charge the nanocrystals. As described previously,[21] even this weak 0.4 nJ/pulse, low-repetition-rate Ti:sapphire excitation without stirring allows detection of the Auger recombination resulting from a steady-state population of reduced ZnO nanocrystals within the excitation volume. The observation of substantial slow PL decay at long times after excitation (*e.g.*, Fig. 2) was used to confirm the presence of nanocrystals without any extra electrons, and hence that the samples were in the low-charging regime even within the experimental excitation volume. (Note that unlike biexciton Auger recombination, which generates single excitons that then luminesce with long lifetimes, the product of this trap-assisted Auger recombination is not luminescent, and the long-time PL thus derives only from uncharged nanocrystals.) Power-dependence measurements[21] show that in this regime, increasing the excitation pulse energy yields increasingly prominent Auger recombination with a constant Auger rate within experimental error. The R = 4.5 nm data point in Fig. 4.2b is taken from the universal fit of the power-dependence data in Fig. 3.8 in chapter 3. We note, too, that unlike the more common transient absorption experiment for measurement of Auger rates, the PL measurement is intrinsically biased toward observation of the singly reduced Auger recombination rates because multiply reduced nanocrystals undergo faster nonradiative Auger recombination and thus emit fewer photons.

To detect the Auger component with sufficient signal-to-noise ratios, small nanocrystals ($R <$ ~3.1 nm) needed to be measured under N_2 atmosphere to elongate the electron lifetime, whereas the Auger signal could be detected in larger nanocrystals ($R \geq$ ~3.1 nm) even under aerobic atmosphere.[22,23] In select cases, the average number of excess electrons per nanocrystal was quantified independently via the near-IR electronic absorption signal of the reduced nanocrystals and the Auger rate constants were confirmed to derive from singly reduced nanocrystals. Where specified, nanocrystal powder samples were made as pastes with ethanol and pressed between two quartz substrates for optical measurements. Similar to the colloid measurements, Auger measurements of the nanocrystal powders were performed with only in-situ charging and in the low-charging regime.

4.3 Results and Discussion

The PL of ZnO nanocrystals is dominated by visible luminescence involving recombination of a conduction-band-like electron with a deeply trapped hole (often associated with oxygen vacancy centers),[24] the latter most likely located at the nanocrystal surfaces[19] (left scheme in Figure 4.1a). Figure 4.1a shows a typical PL spectrum of colloidal dodecylamine-capped ZnO nanocrystals suspended in toluene and excited at 350 nm under aerobic conditions, illustrating trap PL centered ~2.25 eV. Under aerobic conditions, the trap PL shows a multi-exponential decay with components ranging from ns to μs (Figure 4.1b).[21,25] As reported previously,[21,25,26] this trap PL intensity decreases substantially when measured under anaerobic conditions (Figure 4.1a), attributed to the addition of "extra" delocalized conduction-band-like electrons into the nanocrystals, under our conditions via photochemical oxidation of residual ethanol from the nanocrystal synthesis (*i.e.*, the nanocrystals become reduced, or *n*-type, with H^+ charge compensation).[21,27] The long-standing explanation for this suppression is that excess electrons reduce oxygen vacancy centers and thereby eliminate their participation in the PL process.[25] Recently, PL and electron paramagnetic resonance measurements have revealed instead that visible PL in reduced ZnO nanocrystals is quenched by a trap-centered Auger recombination process,[21] but only one size of nanocrystals was examined and the phenomenon was not explored thoroughly. In this process, recombination of conduction-band electrons with deeply trapped holes proceeds via nonradiative energy transfer to the extra conduction-band electron (right scheme in Fig 4.1a). Figure 4.1b illustrates the PL signature of this trap-assisted Auger recombination: Under anaerobic conditions, the visible trap PL decay is dominated by a fast process with $\tau_{\text{Auger}} = 97$ ps.

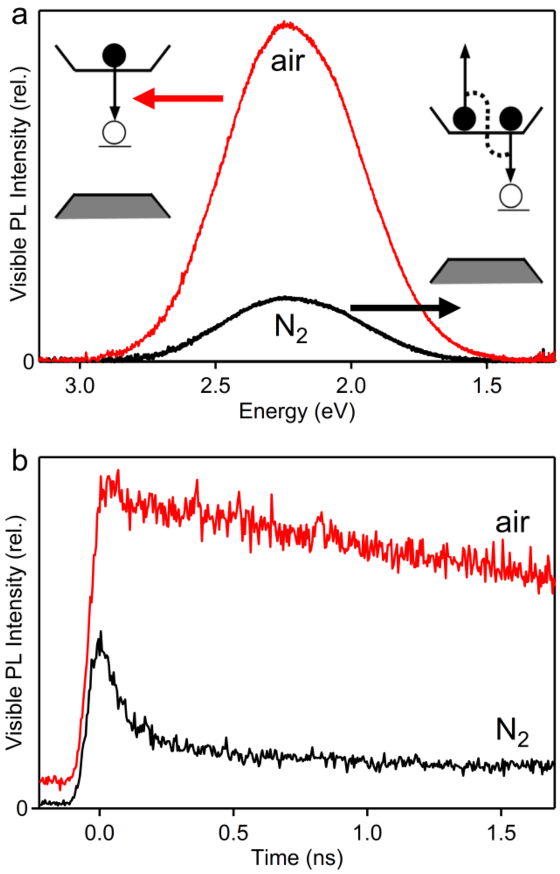

Figure 4.1 Photoluminescence of ZnO nanocrystals. **(a)** CW and **(b)** time-resolved visible PL data collected for the same colloidal suspension of R = 2.8 nm ZnO nanocrystals with 350 nm UV photoexcitation under air (red) and N_2 (black) atmospheres. The insets to (a) depict relaxation of the deep trap state via luminescence (left) or trap-assisted Auger recombination (right).

Multicarrier Auger recombination rates in semiconductor nanocrystals typically depend strongly on crystallite size.[5] For example, biexciton recombination rates universally show an inverse cubic or stronger dependence on nanocrystal radius, R (refs. [5,28,29]). Figure 4.2a plots ZnO trap PL decay curves for nanocrystals of different radii, measured in the low-charging regime (see section 4.2.B) and normalized at t = 0 ns. The Auger rate ($1/\tau_{\text{Auger}}$) slows markedly as R increases. Figure 4.2b presents a double-log plot of τ_{Auger} for nanocrystals from R = 2.1 - 8.0 nm. All data points follow the same linear trend, regardless of whether the nanocrystals are suspended or precipitated. The solid line in Figure 4.2b shows the best fit of these data to a power-law expression (equation 4.1, where A is a scaling factor and n describes the order). The best fit is obtained for n = 2.0, indicating rapidly increasing Auger recombination rates with decreasing nanocrystal radii. Although a strong function of R, this result represents the smallest size dependence reported to date for any Auger process in any nanocrystals (see below).

$$\tau_{\text{Auger}} = AR^n \tag{4.1}$$

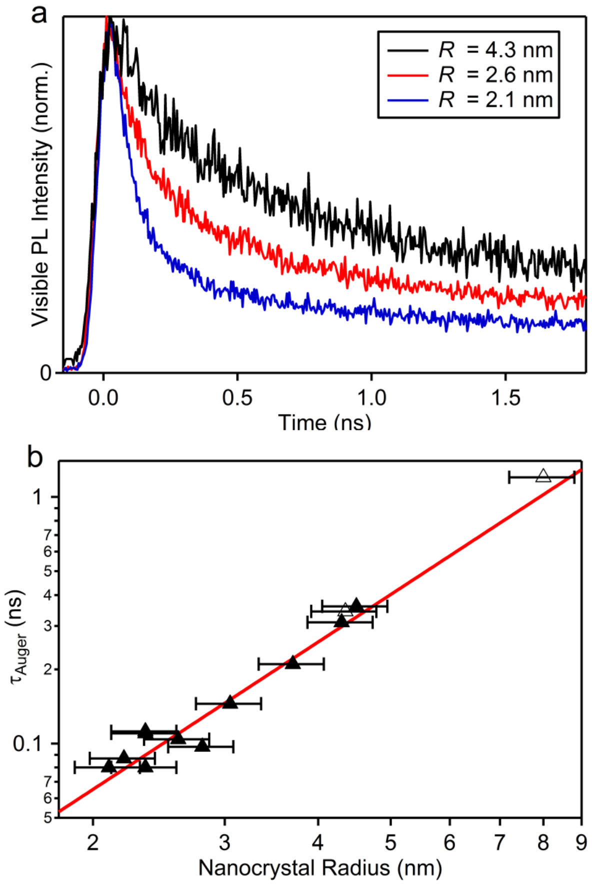

Figure 4.2. Trap-assisted Auger recombination in ZnO nanocrystals. **(a)** Representative PL decay curves measured for the trap emission of colloidal R = 2.1, 2.6, and 4.3 nm ZnO nanocrystals suspended under N_2(g). The decay curves have been normalized at t = 0 ns. **(b)** Electron/trap-state Auger time constants plotted vs ZnO nanocrystal radius. Auger time constants were measured for both colloidal suspensions (▲) and powder samples (Δ). The line shows the best fit of the data to equation (1), obtained with n = 2.0. Error bars illustrate ±10% around the average R.

The closest experimental analog of this electron/trap-state Auger recombination is the negative-trion (electron/exciton) Auger recombination, which has been measured in films of colloidal CdSe quantum dots, and more recently on free-standing colloidal photodoped photodoped CdSe.[13,30] The initial states of these two Auger processes differ only in the location of the hole (deeply trapped here but delocalized for the negative trion). The final states of both processes involve similar highly excited electrons. Figure 4.3 re-plots the data from Figure 2 on a log-log scale, along with CdSe trion Auger recombination rates estimated from ref. 13 and ref 30. For the nanocrystals measured here and in refs 13 and 30 trion Auger recombination is slower than trap-assisted Auger recombination although the trends predict that they will approach the same rate at very small nanocrystal sizes ($R \approx 1$ nm). We can compare the ZnO data with that of biexciton as well as trion Auger recombination in CdSe.[30-33] Overall, the rates of the trap-assisted Auger recombination are closer to the CdSe biexciton rate than the trion rates which is surprising. From Figure 4.3, CdSe biexciton and trion Auger rates show a significantly greater dependence on R than the ZnO trap-assisted Auger data reported here, with a best-fit value of n = 3.1 and n = 4.3 respectively.

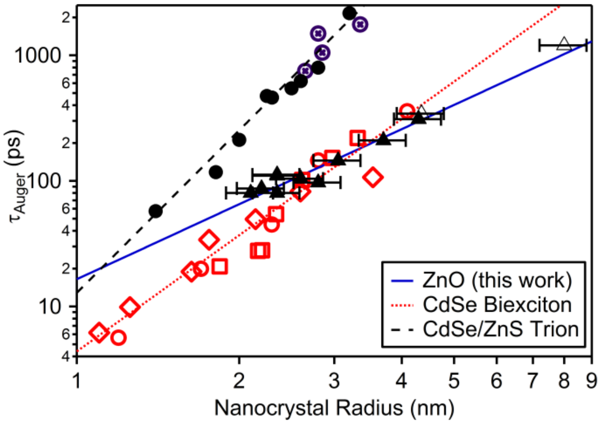

Figure 4.3. Comparison of multicarrier Auger recombination processes. Double-log plot of Auger time constants vs nanocrystal radius from this work (▲, Δ) compared with literature biexciton (○ (ref. 31), ◇ (ref. 32), □ (ref. 33)) and trion (⊗ (ref. 13), ● (ref. 30)) Auger recombination time constants measured for colloidal CdSe nanocrystals. The blue line shows the best fit of equation (1) to the ZnO data (n = 2.0), and the dotted red line shows the best fit of equation (1) to the CdSe biexciton data (n = 3.1). The dashed line shows the best fit of equation (1) to the CdSe/CdS trion data (n = 4.3). Error bars illustrate ±10% around the average R.

Although at first the R^2 dependence in Figure 4.2 may seem to simply reflect scaling of the hole density at the nanocrystal surface in the trap excited state, the Auger recombination rate must reflect the coupling between initial and final states of the multicarrier configuration, and its size dependence is thus more complex. Both electron and hole densities, as well as the multi-electron interaction matrix elements, contribute to the trap-assisted Auger recombination rates,[34] and each of these parameters has a dependence on nanocrystal radius. As with biexciton Auger processes, therefore, the ultimate origin of the unique size dependence in Figure 4.2 is not trivially explained.

Several factors may contribute to the different size dependence of this ZnO trap-assisted Auger recombination and CdSe biexciton Auger recombination. For example, localization in a deep trap makes the hole wavefunction insensitive to R (ref. 24), which may in turn reduce the trap-centered Auger dependence on R. Localization should also strengthen electron-nuclear coupling and may enable more facile momentum conservation than achieved via confinement of CdSe biexcitons, thereby reducing the rate's dependence on R. In addition, the small dielectric constant of ZnO should allow sizeable carrier-carrier Coulomb interactions to be maintained even in the largest nanocrystals, which could dampen the Auger R dependence. The convergence of biexciton Auger rates in nanocrystals of very different dielectric constants and electronic structures[28] argues against explanation of the present data purely in terms of dielectric constants, however. Nevertheless, R in Figure 4.3 extends well beyond the electron (polaron) radius of ZnO ($r_e \sim 1.5$ nm), but not beyond the exciton radius of CdSe ($r_{ex} \sim 5.4$ nm) or other semiconductors that show a stronger Auger size dependence; The Auger size dependence in ZnO may be dampened if electrons do not randomly sample the entire nanocrystal volume because of polarization by the localized hole exacerbated by small dielectric screening. Finally, in contrast with other multicarrier Auger processes studied previously in nanocrystals, this trap-assisted Auger recombination is likely not solely mediated by the Coulomb interaction but also gains allowedness from exchange interactions.[34] The scaling of exchange-mediated Auger rates with wavefunction overlap in addition to charge separation should yield a different R dependence. We note that the R^2 (ZnO) and R^3 (CdSe) slopes in Figure 4.3 are both comparable to those of biexciton Auger rates in nanocrystals estimated from theory ($R^2 - R^4$) (ref. 4).

The absolute rates in Figure 4.3 are also revealing. Surface hole localization might reasonably be expected to slow Auger recombination by increasing electron-hole spatial separation, for example as reported for type II core/shell nanocrystals,[35,36] but this effect apparently is not dominant because this ZnO trap-assisted Auger recombination is faster than CdSe trion Auger recombination on an absolute scale. In fact, data suggest that CdSe biexciton Auger rates are insensitive to surface hole trapping.[33] For $R < \sim 3$ nm, the trap-assisted Auger recombination in reduced ZnO nanocrystals is slower than biexciton Auger recombination in CdSe nanocrystals of the same radius. This difference is largely attributable to the greater probability of a four-particle transition than of a three-particle transition (for example, trion Auger recombination is slower than biexciton Auger recombination in CdSe nanocrystals of the same radius, Figure 4.3). Because of its smaller R dependence, the ZnO trap-assisted recombination curve crosses the CdSe biexciton recombination curve, and at $R > {\sim}3$ nm trap-assisted Auger recombination in reduced ZnO nanocrystals is actually *faster* than biexciton Auger recombination in CdSe nanocrystals of the same radius. Although competitive with other multicarrier recombination processes, this remarkably fast trap-assisted recombination channel has been overlooked in semiconductor nanocrystal research to date.

Finally, we note that the Auger dynamics in Figure 4.2 were monitored by trap PL decay. Auger recombination dynamics are more commonly probed using transient absorption (TA) spectroscopy at the semiconductor absorption edge on the premise that these TA dynamics are correlated with exciton formation and decay. Because extra electrons in ZnO nanocrystals also bleach band-edge absorption,[22,26] we hypothesized that population of the visible-emitting trap excited states (which have conduction-band-like electrons[24]) should also be detected by TA spectroscopy at the ZnO band edge. Figure 4.4 compares data from TA and TRPL measurements on the same suspension of ZnO nanocrystals under low-charging conditions. The trap PL decays with $\tau_{\text{Auger}} \sim 270$ ps and $\tau_{\text{trap}} \sim 2$ μs, and the exciton PL decays with $\tau \sim 80$ ps, consistent with previous measurements.[21] Importantly, the band-edge TA signal shows bleach recovery precisely matching the trap-assisted Auger recombination dynamics seen in the visible PL.

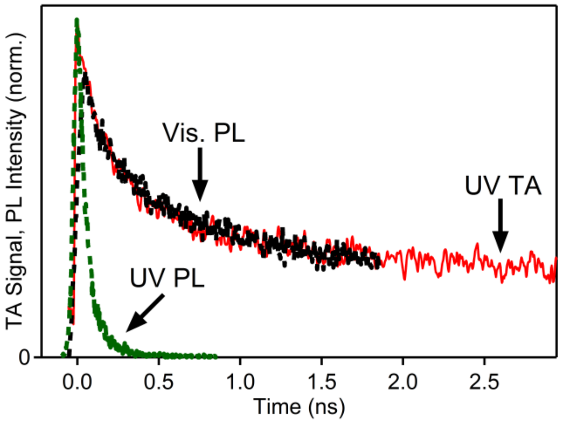

Figure 4.4. Transient absorption. Superposition of intensity-normalized transient-absorption and PL decay signals for R = 3.3 nm ZnO nanocrystals following a 150 fs excitation pulse under the conditions of trap-assisted Auger recombination outlined above. The dotted black curve plots the visible trap-state PL decay ($\lambda_{\mathrm{excitation}}$ = 350 nm, λ_{PL} = 560 nm), showing the characteristic trap-assisted Auger recombination component (τ_{Auger} ~ 270 ps) followed by a slow linear-decay component. The dotted green curve plots the UV near-exciton PL decay ($\lambda_{\mathrm{excitation}}$ = 350 nm, λ_{PL} = 375 nm), showing fast exciton population decay (τ = 80 ps). The solid red curve plots the transient absorption signal measured at the ZnO absorption edge (λ_{pump} = λ_{probe} = 365 nm), which reproduces the trap-state dynamics not the exciton dynamics.

Previous work has already emphasized that band-edge TA measurements of bi- or multiexciton recombination can be complicated by carrier-trapping dynamics[11] and subsequent multicarrier recombination of charged excitons.[37] The data in Figure 4.4 illustrate that TA at the absorption edge is also sensitive to trapped-carrier *decay* dynamics. This sensitivity is particularly evident here because the short single-exciton decay times of ZnO nanocrystals allow facile separation of exciton population and trap-centered Auger dynamics. In cases where single-exciton decay is much slower than multiexciton Auger recombination, such as in CdSe QDs, it will not be as clear when TA signals are influenced by trap dynamics because trap-assisted and other Auger processes may occur on similar timescales. Furthermore, such trap-assisted Auger recombination can contribute to apparent exciton decay dynamics independent of measurement technique. Scheme 4.1 illustrates one specific trap-assisted Auger recombination process that can be anticipated to complicate biexciton recombination dynamics in some cases. Panel (a) illustrates the process investigated here in reduced ZnO nanocrystals for reference. Panels (b) and (c) illustrate what may be observed in biexciton recombination studies when one photoexcitation event has led to trapping of a carrier (a hole in this illustration) at the nanocrystal surface ("photocharging"). It has been widely assumed that photoexcitation of such photocharged nanocrystals yields a charged exciton that undergoes Auger recombination to generate a hot carrier, as illustrated in panel (b). As emphasized in ref. 11, this motif is better characterized as a polarized biexciton, implying that all carriers may participate in Auger recombination. The results presented here suggest that the process in panel (c) is kinetically competitive with that in panel (b) and cannot be neglected. Here, the Auger process involves trap-centered electron-hole recombination and formation of a hot exciton (with electron excitation illustrated for simplicity). For deeply trapped holes like in our ZnO nanocrystals, this trap-centered electron-hole recombination has been considered slow because of severely reduced overlap,[38] but the data in Figure 4.2 demonstrate that it can be surprisingly fast. Given the rapidity and ubiquity of surface carrier trapping in nanocrystals, it is likely that such trap-assisted Auger processes have contributed to multicarrier recombination dynamics measured at the band edges of other semiconductor nanocrystals showing facile carrier trapping.[29,37]

Scheme 4.1

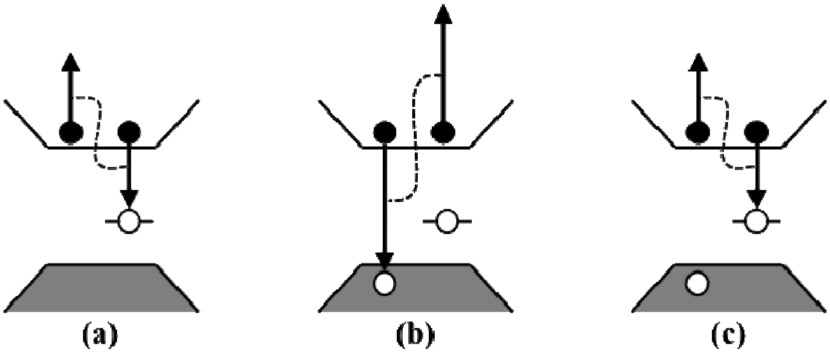

We note, too, that trap-assisted Auger recombination makes the multicarrier excited state of panel (c) involving a surface-trapped charge fundamentally different from biexciton or true trion states, whose relatively slow Auger recombination rates have recently called into question an Auger-based explanation of nanocrystal blinking,[13,14] particularly if Auger kinetics in the former are governed by exchange rather than Coulomb interactions. The revelation here of rapid and size-dependent trap-assisted Auger recombination in semiconductor nanocrystals may be relevant for understanding the discrepancies between the dark states of nanocrystal blinking studies and the experimental Auger recombination rates of biexciton or trion states.

4.4 Conclusion

In summary, we report the first observation of size-dependent trap-assisted Auger recombination in semiconductor nanocrystals. This recombination process is fundamentally distinct from the known size-dependent Auger recombination processes in that it involves deeply trapped charge carriers. It is surprisingly fast, however, having rates comparable to biexciton Auger recombination in CdSe nanocrystals. Like bi- and multiexciton Auger recombination, trap-assisted Auger rates depend strongly on nanocrystal radius, although displaying the weakest radius dependence yet described for any Auger process in any semiconductor nanocrystals. As a consequence, this process remains relatively fast even in bulk-like ZnO crystallites ($R > \sim 8.0$ nm), with potential implications for efficiency droop in high-current white-light LEDs based on nanocrystalline ZnO or related deep-level-emission phosphors.[39,40] Because of these high rates, the ubiquity of surface carrier traps in semiconductor nanocrystals, and the ambiguity of common spectroscopic probes with respect to multicarrier recombination mechanism, trap-assisted Auger recombination is likely more prevalent than previously recognized.

4.5 Notes to Chapter 4

(1) Cohn, A. W.; Schimpf, A. M.; Gunthardt, C. E.; Gamelin, D. R. *Nano Lett.* **2013**, *13*, 1810.

(2) Landsberg, P. T. *Recombination in Semiconductors*; Cambridge University Press: Cambridge, 1991.

(3) Shen, Y. C.; Mueller, G. O.; Watanabe, S.; Gardner, N. F.; Munkholm, A.; Krames, M. R. *Appl. Phys. Lett* **2007**, *91*, 141101.

(4) Efros, A. L. In *Semiconductor Nanocrystals: from Basic Principles to Applications*; Efros, A. L., Lockwood, D. J., Tsybeskov, L., Eds.; Kluwer Academic: New York, 2003, p 52.

(5) Klimov, V. I. *J. Phys. Chem. B* **2006**, *110*, 16827.

(6) Kambhampati, P. *J. Phys. Chem. Lett.* **2012**, *3*, 1182.

(7) Klimov, V. I.; Ivanov, S. A.; Nanda, J.; Achermann, M.; Bezel, I.; McGuire, J. A.; Piryatinski, A. *Nature* **2007**, *447*, 441.

(8) Dang, C.; Lee, J.; Breen, C.; Steckel, J. S.; Coe-Sullivan, S.; Nurmikko, A. *Nature Nanotech.* **2012**, *7*, 335.

(9) Klimov, V. I. *Appl. Phys. Lett.* **2006**, *89*, 123118.

(10) Semonin, O. E.; Luther, J. M.; Choi, S.; Chen, H.-Y.; Gao, J.; Nozik, A. J.; Beard, M. C. *Science* **2011**, *334*, 1530.

(11) Tyagi, P.; Kambhampati, P. *J. Chem. Phys.* **2011**, *134*, 094706.

(12) Chepic, D. I.; Efros, A. L.; Ekimov, A. I.; Ivanov, M. G.; Kharchenko, V. A.; Kudriavtsev, I. A.; Yazeva, T. V. *J. Lumin.* **1990**, *47*, 113.

(13) Jha, P. P.; Guyot-Sionnest, P. *ACS Nano* **2009**, *3*, 1011.

(14) Zhao, J.; Nair, G.; Fisher, B. R.; Bawendi, M. G. *Phys. Rev. Lett.* **2010**, *104*, 157403.

(15) Rosen, S.; Schwartz, O.; Oron, D. *Physical Review Letters* **2010**, *104*, 157404.

(16) Califano, M. *J. Phys. Chem. C* **2011**, *115*, 18051.

(17) Landsberg, P. T. *Appl. Phys. Lett.* **1987**, *50*, 745.

(18) Schwartz, D. A.; Norberg, N. S.; Nguyen, Q. P.; Parker, J. M.; Gamelin, D. R. *J. Am. Chem. Soc.* **2003**, *125*, 13205.

(19) Norberg, N. S.; Gamelin, D. R. *J. Phys. Chem. B* **2005**, *109*, 20810.

(20) Wood, A.; Giersig, M.; Hilgendorff, M.; Vilas-Campos, A.; Liz-Marzán, L. M.; Mulvaney, P. *Aust. J. Chem.* **2003**, *56*, 1051.

(21) Cohn, A.; Janßen, N.; Mayer, J. M.; Gamelin, D. R. *J. Phys. Chem. C* **2012**, *116*, 20633−20642.

(22) Haase, M.; Weller, H.; Henglein, A. *J. Phys. Chem.* **1988**, *92*, 482.

(23) Stroyuk, O. L.; Dzhagan, V. M.; Shvalagin, V. V.; Kuchmiy, S. Y. *J. Phys. Chem. C* **2010**, *114*, 220.

(24) van Dijken, A.; Meulenkamp, E. A.; Vanmaekelbergh, D.; Meijerink, A. *J. Lumin.* **2000**, *90*, 123.

(25) van Dijken, A.; Meulenkamp, E. A.; Vanmaekelbergh, D.; Meijerink, A. *J. Phys. Chem. B* **2000**, *104*, 4355.

(26) Shim, M.; Guyot-Sionnest, P. *J. Am. Chem. Soc.* **2001**, *123*, 11651.

(27) Wood, A.; Giersig, M.; Mulvaney, P. *J. Phys. Chem. B* **2001**, *105*, 8810.

(28) Robel, I.; Gresback, R.; Kortshagen, U.; Schaller, R. D.; Klimov, V. I. *Phys. Rev. Lett.* **2009**, *102*, 177404.

(29) Kobayashi, Y.; Nishimura, T.; Yamaguchi, H.; Tamai, N. *J. Phys. Chem. Lett.* **2011**, *2*, 1051.

(30) Cohn, A. W.; Rinehart, J. D.; Schimpf, A. M.; Weaver, A. L. **2013**, submitted.

(31) Klimov, V. I.; Mikhailovsky, A. A.; McBranch, D. W.; Leatherdale, C. A.; Bawendi, M. G. *Science* **2000**, *287*, 1011.

(32) Achermann, M.; Hollingsworth, J. A.; Klimov, V. I. *Phys. Rev. B* **2003**, *68*, 245302.

(33) Pandey, A.; Guyot-Sionnest, P. *J. Chem. Phys.* **2007**, *127*, 111104.

(34) Landsberg, P. T.; Rhys-Roberts, C.; Lal, P. *Proc. Phys. Soc.* **1964**, *84*, 915.

(35) Nanda, J.; Ivanov, S. A.; Htoon, H.; Bezel, I.; Piryatinski, A.; Tretiak, S.; Klimov, V. I. *J. Appl. Phys.* **2006**, *99*, 034309.

(36) Oron, D.; Kazes, M.; Banin, U. *Phys. Rev. B* **2007**, *75*, 035330.

(37) McGuire, J. A.; Sykora, M.; Joo, J.; Pietryga, J. M.; Klimov, V. I. *Nano Letters* **2010**, *10*, 2049.

(38) Califano, M. *ACS Nano* **2011**, *5*, 3614.

(39) Willander, M.; Nur, O.; Bano, N.; Sultana, K. *New J. Phys.* **2009**, *11*, 125020.

(40) Nannen, E.; Kummell, T.; Ebbers, A.; Bacher, G. *Appl. Phys. Express* **2012**, *5*, 035001.

Chapter 5: Size Dependence of Negative Trion Auger Recombination in Photodoped CdSe Nanocrystals

We report a systematic investigation of the size dependence of negative trion (T^-) Auger recombination rates in free-standing colloidal CdSe nanocrystals. Colloidal *n*-type CdSe nanocrystals of various radii have been prepared photochemically, and their trion decay dynamics have been measured using time-resolved photoluminescence spectroscopy. Trion Auger time constants spanning three orders of magnitude are observed, ranging from 57 ps (radius R = 1.4 nm) to 2.2 ns (R = 3.2 nm). The data reveal a substantially stronger size dependence than found for bi- or multi-exciton Auger recombination in CdSe or other semiconductor nanocrystals, scaling in proportion to $R^{4.3}$. This work was done in collaboration with Dr. Jeffrey Rinehart, Alina Schimpf, and Amanda Weaver and is published in Ref. [1]

5.1 Introduction

Semiconductor nanocrystals possessing one or more "extra" charge carriers are central to many nascent quantum-dot technologies, from quantum computers[2,3] to solar cells.[4,5] In addition to changing the electrical and spin properties of quantum dots, the extra charge carriers have a dramatic impact on nanocrystal excited-state relaxation dynamics. Photoexcitation of an *n*- or *p*-doped nanocrystal with just one extra delocalized carrier creates a trion state (T^- or T^+, respectively) that can relax rapidly via a so-called Auger recombination,[6] in which the energy of the photogenerated electron-hole pair is transferred non-radiatively to the extra carrier.

Trion Auger recombination has long been suspected to play a major role in nanocrystal photoluminescence (PL) intermittency,[7-12] and recent work has suggested that trion Auger recombination in photoionized nanocrystals may have contributed to overestimated carrier-multiplication yields.[13,14] Trion Auger recombination has also been implicated in efficiency droop in nanocrystal light-emitting diodes (LEDs),[15] as proposed for bulk LEDs.[16] Given the enormous scrutiny of photophysical processes linked to trions in these contexts, there has been remarkably little direct characterization of trion Auger recombination in colloidal semiconductor nanocrystals. For example, only recently were any negative-trion decay times of colloidal *n*-type nanocrystals directly measured, in this case for electrochemically reduced CdSe/CdS nanocrystals (*R*(core) = ~2 nm, *R*(core/shell) = ~3 nm) affixed to electrode surfaces.[9] These measurements revealed T^- Auger recombination an order of magnitude slower than biexciton Auger recombination, and hence not sufficiently fast compared to radiative decay to account for nanocrystal intermittent dark states. Transient trion formation has been correlated with the occurrence of “grey” states in PL blinking traces,[17-19] confirming the importance of this motif in nanocrystal PL intermittency.

Where examined, multi-carrier Auger recombination is generally greatly accelerated in nanocrystals,[20-22] likely because of the importance of interfaces for momentum conservation. For example, biexciton Auger recombination rates scale roughly with the inverse nanocrystal volume, the same size dependence has been observed for multi-excitons,[23] and a linear scaling with volume has been assumed for trions as well.[15,18,24] This size dependence can be qualitatively understood in terms of increasing high-*k* components of the charge-carrier wavefunctions with increasing confinement,[25] but systematic data characterizing trion Auger recombination in different sized nanocrystals are not available for quantitative assessment. A thorough and systematic experimental characterization of trion Auger rates in semiconductor nanocrystals would provide valuable input for quantitative theoretical descriptions of the critical factors regulating Auger rates in quantum dots in general. To this end, we report here the size dependence of T^- Auger recombination rates in free-standing colloidal *n*-type CdSe nanocrystals prepared via photochemical oxidation of the sacrificial hole quencher Li[Et_3BH].[26] The resulting data agree well with the literature data[9] for CdSe/CdS nanocrystals at R ~ 3 nm, but show a significantly stronger size dependence than biexciton or multi-exciton Auger recombination when other sizes are considered. The implications of these new data are discussed.

5.2 Experimental

5.2.A Synthesis Colloidal CdSe nanocrystals were synthesized by hot-injection following literature procedures.[27-29] R = 3.2, 2.5, 2.3, and 2.0 nm nanocrystals were synthesized following the procedures detailed in refs. 27,28. R = 2.8, 2.6, 2.5, and 1.8 nm nanocrystals were synthesized by adapting the procedures of ref. 29. For this, 0.05 g CdO and 0.5 g stearic acid were degassed in a three neck flask at 100 °C, after which the temperature was raised to 270 °C and cadmium stearate was formed. The temperature was lowered to 100 °C and 2.5 g hexadecylamine and 2 g trioctylphosphine oxide (TOPO) were added to the flask. This mixture was degassed for 30 min before the temperature was raised to 330 °C and a solution of 0.15 g Se in 1.5 mL trioctylphosphine (TOP) was swiftly injected. The growth time was adjusted to between 1 min and 3 min to reach the desired nanocrystal sizes. Nanocrystals with R = 1.4 nm were obtained following the same procedure but by adding 16 g of octadecene to the cation reaction flask to be degassed along with the CdO and stearic acid. For all nanocrystals, ZnS shells were grown using the SILAR method.[30]

5.2.B Physical methods and photodoping All spectroscopic data were collected at room temperature on colloidal suspensions of nanocrystals. Absorption spectra collected using a Cary 500 spectrophotometer (Varian), and nanocrystal radii were estimated from these spectra using the empirical relationship presented in ref. 31. For photoluminescence measurements, a sealable cuvette containing 2 mL of nanocrystal solution (band gap absorption = 0.1- 0.2) with ~2 mg extra 99% TOPO as well as ~0.1 mL TOP if necessary (see main text) was prepared in a N_2 atmosphere glovebox. This solution was used for neutral-exciton photoluminescence, luminescence decay, and absorption measurements and then brought back into the glovebox. Nanocrystal photodoping was then performed following the procedures detailed in ref. [26]. Briefly, 10 µL of 1 M lithium triethylborohydride ($Li[Et_3BH]$) in THF (used as received from Sigma-Aldrich) was added to 1 mL of toluene, and 10 µL – 20 µL of this 0.01 M $Li[Et_3BH]$ solution was added to the nanocrystal solution. For all nanocrystals, exposure to ambient room lights was sufficient to photodope the nanocrystals within ~3 min, with the exception of the smallest (R = 1.4 nm) nanocrystals, which were instead illuminated using a Hg/Xe arc lamp equipped with a 450 nm cut-off filter for ~5 min. For chemical reduction, 60 µL of ~0.1 M sodium biphenyl radical solution (Na[biphen]) was added instead of $Li[Et_3BH]$. Photoluminescence decay curves were measured by exciting the nanocrystals with the frequency-doubled output of a Ti:sapphire laser at a 500 kHz repetition rate (400 nm, 150 fs pulse, 0.7 nJ/pulse). Decay curves were recorded using a monochromator and streak camera with an instrument response function of ~15 ps. Luminescence spectra were collected using an unfocused 405 nm laser diode (~5 mW) for excitation and an OceanOptics 2000+ spectrometer for detection.

5.3 Results and Discussion

Figure 5.1 plots absorption and PL spectra of representative CdSe nanocrystals used in this study. The dotted curves show features characteristic of high-quality hot-injection CdSe nanocrystals. The solid curves show spectra of the same nanocrystals following growth of thin (~1 monolayer) ZnS shells. The spectra are not significantly altered upon shell growth, as expected. Such ZnS shells eliminate nonradiative decay channels without relaxing carrier confinement, which would complicate analysis of the Auger dependence on nanocrystal radius. The remaining experiments described in this paper were all performed using similar CdSe/ZnS core/shell nanocrystals, and the data were analyzed assuming an effective radius equal to that of the CdSe cores alone.

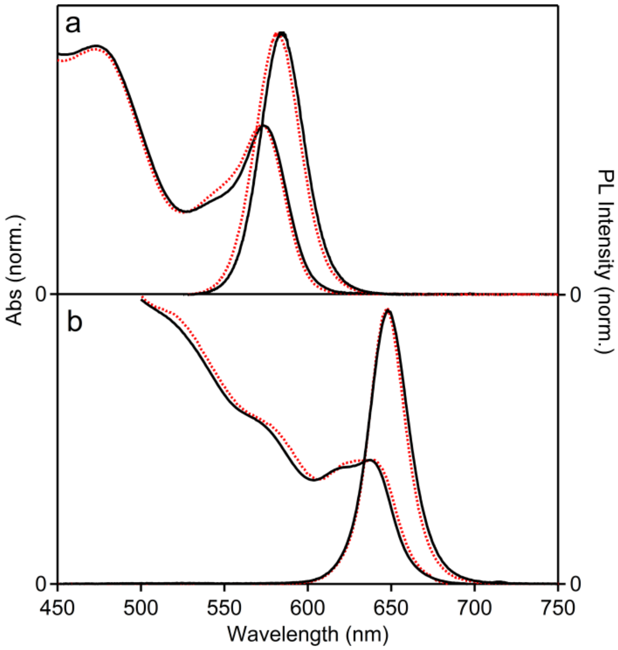

Figure 5.1. Room-temperature absorption and photoluminescence spectra of representative colloidal CdSe core nanocrystals (dotted red) and CdSe/ZnS core/shell nanocrystals (solid black). **(a)** R = 1.8 nm core nanocrystals, and (**b**) R = 3.2 nm core nanocrystals. Spectra have been normalized to facilitate comparison.

Colloidal *n*-type nanocrystals were prepared by photoexcitation of these CdSe/ZnS core/shell nanocrystals in the presence of the hole quencher, Li[Et$_3$BH], as detailed previously[26] (see 5.2.B). Under anaerobic conditions, this photochemical borohydride oxidation yields a stable population of colloidal nanocrystals possessing extra conduction-band electrons compensated by Li$^+$ and H$^+$ cations. These colloidal *n*-type nanocrystals are of high spectroscopic quality, making them well suited for further spectroscopic examination. Figure 5.2 shows a representative set of absorption spectra and PL decay curves measured before photodoping, after photodoping, and after re-oxidation of the CdSe/ZnS nanocrystals in air. The decrease at the first absorption maximum upon photodoping is characteristic of partial occupancy of the conduction band by delocalized electrons.[32] Because the $1S_e$ orbital can be occupied by two electrons, reduction by two electrons per nanocrystal would yield a full absorption bleach.[32] The data in Figure 5.2a show ~20% absorption bleach at the first maximum, indicating an average number of conduction-band electrons per nanocrystal of $\langle n \rangle$ ~ 0.4. For all measurements described here, photodoping was kept at $\langle n \rangle << 1$ to exclude the possibility of doubly reduced nanocrystals. The photodoped nanocrystals are readily re-oxidized upon opening the cuvette to air. Figure 5.2a shows that the absorption spectrum of the re-oxidized nanocrystals nicely overlays that collected prior to photodoping, indicating well-behaved reversible photodoping without sample degradation.[26]

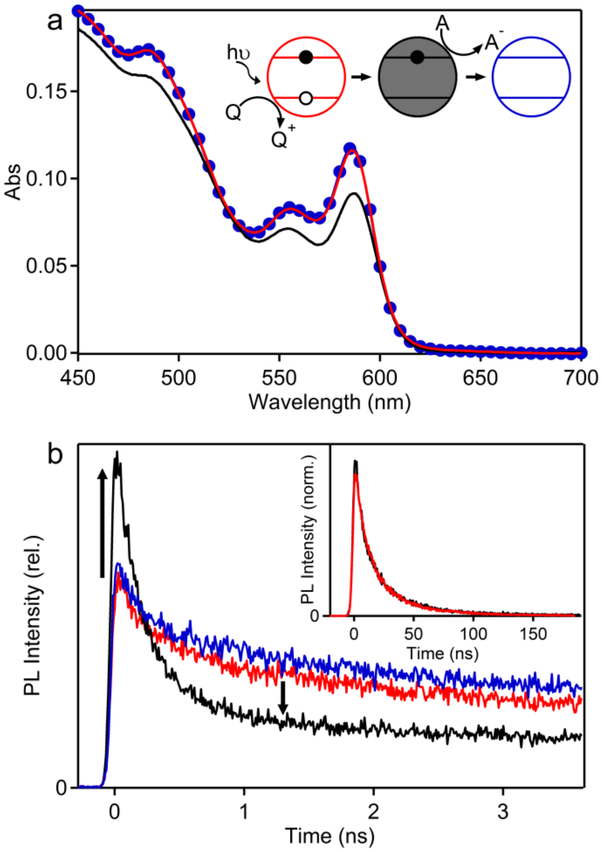

Figure 5.2. (a) Room-temperature absorption spectra of colloidal *R* = 2 nm CdSe/ZnS nanocrystals before photodoping (red), after photodoping (black), and after re-oxidation by exposure to air (blue circles). The inset summarizes the photodoping and re-oxidation processes schematically. **(b)** Room-temperature neutral-exciton and trion PL decay curves associated with the three absorption spectra in (a). The inset shows the complete PL decay curves measured before (red) and after (black) photodoping, normalized at 50 ns. The arrows indicate intensity changes upon photodoping.

In the time domain, the PL decay measured prior to photodoping is dominated by a τ ~ 17 ns component similar to the radiative lifetime expected[33] at room temperature. A small, fast-decay component (τ = 0.57 ns) is also observed, attributable to nonradiative processes. For all samples reported here, the exciton PL decay prior to photodoping is similarly multi-exponential, which is common among CdSe nanocrystals.[34,35] Upon photodoping (confirmed by the exciton bleach in Figure 5.2a), the PL decay of this same sample shows an increase in intensity at short times that decays relatively rapidly (τ = 0.22 ns), followed by a slow decay process. The inset of Figure

5.2b plots the PL decay curves of the neutral and photodoped nanocrystals over a long time window, normalized at t = 50 ns. The two decay curves overlay one another well, confirming that the long time component in the photodoped sample is simply due to decay of neutral nanocrystals in the ensemble having $\langle n \rangle << 1$. To ensure measurement of solely trion decay times, and not decay of nanocrystals containing multiple electrons, all measurements reported here were performed under conditions where neutral nanocrystals were clearly detected in the PL decay. In addition, nanocrystals possessing more than one extra conduction electron have a second PL peak at higher energy than that observed from the neutral exciton or negative trion. This peak is attributed to recombination of electrons from the $1P_e$ conduction level with valence-band holes,[36] and PL spectra were therefore used to verify that this feature was not present under the conditions used for the trion lifetime measurements.

Figure 5.2b also shows that the PL decay of the re-oxidized nanocrystals does not perfectly overlay that of the same nanocrystals prior to photodoping. Frequently, the PL intensity recovers completely only after extended exposure to air, and initial recovery was found to vary from sample to sample. The source of this variability is not clear, but it may arise from slow re-oxidation of deeply trapped electrons, or possibly from surface restructuring of the photodoped nanocrystals. Importantly, even when the PL intensity does not recover fully, the PL decay kinetics do, indicating that the lost PL intensity is associated with nonradiative processes that are faster than our PL instrument response time (~15 ps). We have observed that the intensity irreversibility can be mitigated, if not completely suppressed, by addition of surface-passivating trioctylphosphine ligands to the nanocrystal solution before photodoping. These observations suggest that the intensity irreversibility may relate to creation of new surface traps upon photodoping.

The PL decay data in Figure 5.2b are very similar to those reported for CdSe/CdS nanocrystals reduced electrochemically.[9] The increased intensity at short times upon reduction is attributable to the increased radiative decay rate of the trion (about twice that of the exciton). The much faster decay of this PL is attributable to trion Auger recombination. To quantify the trion lifetimes from these data, we first subtracted the PL decay signal from the neutral nanocrystals present in the ensemble. Here, the PL decay measured before photodoping was fitted at long times with a single-exponential function to give the dominant component of the neutral exciton lifetime (τ_{Xslow}). With τ_{Xslow} held constant, the neutral exciton PL decay at short times was then fitted to a bi-exponential function (eqn 5.1), where τ_{Xfast} accounts for faster nonradiative decay processes of the neutral nanocrystals. This bi-exponential fit reasonably reproduces the experimental multi-exponential decay over all times. The trion lifetime ($\tau_{\mathrm{T^-}}$) was then determined by fitting the PL decay of the photodoped nanocrystals with eqn 5.2, keeping τ_{Xslow}, τ_{Xfast}, and $A_{\mathrm{slow}}/A_{\mathrm{fast}}$ fixed to account for the remaining neutral nanocrystals. This procedure is equivalent to simply subtracting the PL decay of the residual neutral nanocrystals and fitting the trion decay with a single exponential.

$$I(t) = A_{slow}\exp\left(\frac{-t}{\tau_{Xslow}}\right) + A_{fast}\exp\left(\frac{-t}{\tau_{Xfast}}\right) \tag{5.1}$$

$$I(t) = c\left[A_{slow}\exp\left(\frac{-t}{\tau_{Xslow}}\right) + A_{fast}\exp\left(\frac{-t}{\tau_{Xfast}}\right)\right] + A_{T^-}\exp\left(\frac{-t}{\tau_{T^-}}\right) \tag{5.2}$$

As described by eqn 5.3, $\tau_{\mathrm{T^-}}$ is determined by trion radiative decay and Auger recombination dynamics. The trion's radiative decay time constant ($\tau_{\mathrm{T^-rad}}$) can be estimated from τ_{Xslow} based on the empirical ratio of $\tau_{\mathrm{Xrad}}/\tau_{\mathrm{T^-rad}} = 2.2$,[9] and its Auger time constant ($\tau_{\mathrm{A^-}}$) is then determined using eqn 3. This analysis thus assumes that no other nonradiative processes appear upon photodoping, disappear upon reoxidation, *and* occur on the same timescale as the trion Auger recombination, where they would contaminate the Auger recombination dynamics. This assumption is not easily justified *a priori*, but its validity is supported by the collection of data over different nanocrystal radii (*vide infra*) and by comparison with literature data.

$$\frac{1}{t_{T^-}} = \frac{1}{t_{A^-}} + \frac{1}{t_{T^-_{Rad}}} \tag{5.3}$$

Figure 5.3 plots the PL decay of three photodoped ($\langle n \rangle$ << 1) CdSe/ZnS nanocrystal samples with different radii. The curves are all normalized at t = 0 ns to illustrate the increasingly rapid trion decay with decreasing nanocrystal radius (arrow). Following the procedure outlined above, τ_{A^-} was determined for each sample, as well as for several other samples with various radii. The inset shows a double-log plot of τ_{A^-} vs R for the entire set of samples. τ_{A^-} spans three orders of magnitude, ranging from 57 ps (R = 1.4 nm) to 2.2 ns (R = 3.2 nm). The largest CdSe nanocrystals in Figure 5.3 were also reduced using sodium biphenyl (Na[biphen]) as the reductant, and τ_{A^-} determined in the same way is also plotted in the inset. The chemically and photochemically reduced nanocrystals show indistinguishable τ_{A^-} values. These data reveal a strong and well-behaved dependence of the T^- Auger recombination time on nanocrystal radius. For this entire data set, a best fit to eqn 5.4 yields p = 4.3. This exponent is robust with respect to the method of data analysis. For example, very similar results are obtained when $\tau_{\mathrm{Xrad}}/\tau_{\mathrm{T^-rad}}$ is assumed to equal 2.0. Likewise, simply fitting the raw PL decay data of the photodoped nanocrystals (*e.g.*, Figure 3) with a single exponential function and an intensity offset also yields the same result (see Supporting Information). The insensitivity of the exponent (p = 4.3) to the method of data analysis reflects the fact that trion Auger recombination is the dominant feature of the photodoped nanocrystal PL decay data in this time window.

$$t_{Auger} = AR^{p} \tag{5.4}$$

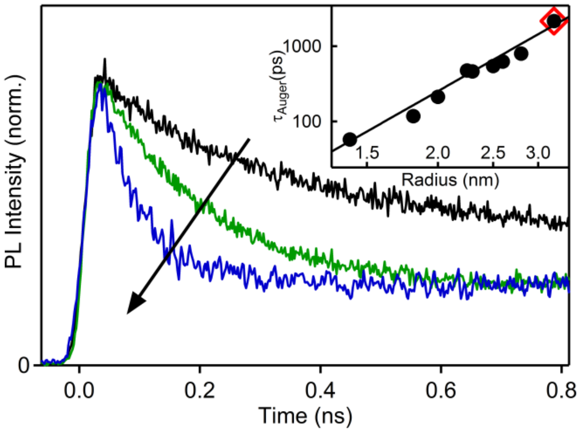

Figure 5.3. Room-temperature photoluminescence decay curves measured for colloidal photodoped CdSe/ZnS nanocrystals of different radii, *R*, normalized at *t* = 0 ns. Decay curves are shown for *R* = 1.4 nm (blue), 2.0 nm (green), and 3.2 nm (black), and the arrow shows the decreasing trion lifetime with decreasing *R*. Note that each sample has a different fraction of nanocrystals with no electrons, so the decay curves do not all approach precisely the same long-time asymptote. The inset shows a double-log plot of τ_{A^-} vs *R* for the entire series of CdSe/ZnS nanocrystals measured here following photodoping (●). The *R* = 3.2 nm nanocrystals were also examined following chemical reduction using Na[biphen] (red ◊). The line in the inset shows the best fit to the data using eqn 4, which yields *p* = 4.3.

There is very little scatter among the data in Figure 5.3(inset), despite having used two different CdSe nanocrystal syntheses and two different methods of nanocrystal *n*-doping (photochemical and chemical), and having samples showing different extents of competing non-radiative neutral-exciton decay. For example, two nanocrystals with $R \approx 2.3$ nm synthesized by the methods of refs. 27,28 and ref. 29 showed significantly different neutral-exciton PL decay dynamics, with τ_{Xslow} = 24 vs 16 ns, respectively, but their τ_{A^-} values differed by only ~5%. Similarly, the τ_{A^-} values measured for the same chemically and photochemically reduced *R* = 3.2 nm nanocrystals were indistinguishable (Figure 5.3, inset). These results provide additional strong support for the robustness of the analysis described above. Specifically, the method of *n*-

doping, and changes in other nonradiative relaxation processes upon *n*-doping, do not significantly impact the trion decay measurements. For example, filling (reduction) of mid-gap traps is known to occur during this photodoping.[26] Although such filling could conceivably introduce competing "trap-assisted" Auger recombination processes,[37] the new trap-centered recombination observed following photodoping of these CdSe nanocrystals occurs much faster than the trion Auger recombination. Consequently, trap reduction causes an overall decrease in PL intensity without obscuring the trion decay dynamics.[26]

The data in Figure 5.3 offer the opportunity to compare the experimental size dependence of a trion's Auger recombination with those of other multi-carrier Auger recombination processes for the first time. Figure 5.4 plots the negative trion τ_{A^-} values from this work together with τ_{A^-} values estimated from analogous literature data.[9] At similar R, the τ_{A^-} values from the present work agree remarkably well with those deduced from trion decay data reported[9] for electrochemically reduced $R \sim 3$ nm CdSe/CdS nanocrystals (assuming the full core/shell radius to be the effective radius, and analyzed as described above). This agreement lends further credence to the analysis applied here. Figure 5.4 also plots literature[23,38,39] biexciton Auger recombination times (τ_A^{xx}) vs R for similar CdSe nanocrystals. As reported previously,[21,23,38,39] fitting these τ_A^{xx} data to eqn 5.4 yields $p = 3.0$.

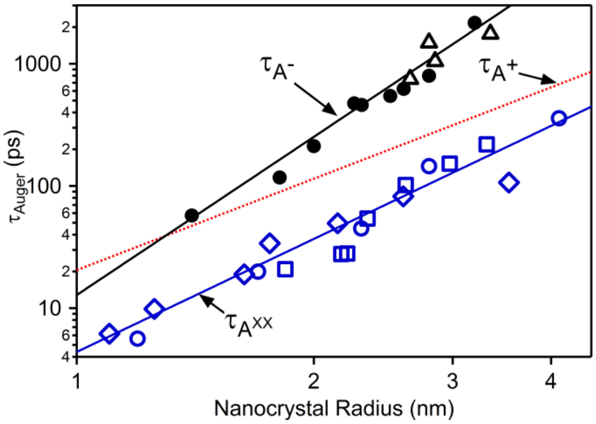

Figure 5.4. Double-log plot of Auger recombination time constants vs CdSe nanocrystal radius, including experimental negative trion (τ_{A}-) and biexciton ($\tau_{\mathrm{A}}^{\mathrm{xx}}$) Auger time constants, and projected positive trion (τ_{A^+}) Auger time constants: τ_{A}- from this work (●); Literature τ_{A}- (Δ, ref. 9); Literature $\tau_{\mathrm{A}}^{\mathrm{xx}}$ (blue symbols: ○ (ref. 23), ◊ (ref. 38), □ (ref. 39)). The size dependence of τ_{A^+} (red dotted line) is calculated from the best fits of eqn 5.4 to the experimental τ_{A}- data (p = 4.3) and the literature $\tau_{\mathrm{A}}^{\mathrm{xx}}$ data (p = 3.0) using eqn 5.5, and yields p = 2.5 from eqn 4.

Just as the precise origins of the p = 3.0 size dependence of $\tau_{\mathrm{A}}^{\mathrm{xx}}$ are not trivially understood,[21] it is not obvious why τ_{A}- scales with p = 4.3. Trion Auger recombination rates are governed by Fermi Golden Rule considerations,[25] and are expected to depend on inter-carrier Coulomb interaction strengths, carrier surface probability densities, shapes of the confinement potentials, confinement-induced state mixing, and densities of states fulfilling the resonance criteria, all of which should vary with nanocrystal size. A stronger size dependence of the resonant density of states for trion vs biexciton Auger recombination, for example, might manifest itself in the observed stronger size dependence of τ_{A}- than of $\tau_{\mathrm{A}}^{\mathrm{xx}}$. It is not known which, if any, of these factors is dominant.

In simple core-only nanocrystals, the biexciton Auger recombination time constant has been related to positive and negative trion Auger recombination time constants based on statistical considerations as described by eqn 5.5.[40] There is still no consensus about the relative magnitudes or size dependence of $\tau_{\mathrm{A}-}$, $\tau_{\mathrm{A}+}$, and $\tau_{\mathrm{A}^{\mathrm{xx}}}$, in CdSe nanocrystals, however. For example, some calculations[40] suggest $\tau_{\mathrm{A}-} \approx \tau_{\mathrm{A}+}$, and hence $\tau_{\mathrm{A}-}/\tau_{\mathrm{A}^{\mathrm{xx}}} \approx 4$ (from eqn 5.5), but others[41] suggest a significantly smaller ratio of $\tau_{\mathrm{A}-}/\tau_{\mathrm{A}^{\mathrm{xx}}} \approx 2.3$. From the experimental size dependence of $\tau_{\mathrm{A}-}$ measured here, it is evident that $\tau_{\mathrm{A}-}$ and $\tau_{\mathrm{A}^{\mathrm{xx}}}$ depend differently on R ($p = 4.3$ vs 3.0), and hence $\tau_{\mathrm{A}-}/\tau_{\mathrm{A}^{\mathrm{xx}}}$ must also be size dependent. From these data, $\tau_{\mathrm{A}-}/\tau_{\mathrm{A}^{\mathrm{xx}}}$ decreases from ~13 at $R = 3.3$ nm to ~5 at $R = 1.4$ nm. A size dependence of $\tau_{\mathrm{A}-}/\tau_{\mathrm{A}^{\mathrm{xx}}}$ in CdSe nanocrystals has been predicted theoretically, in which $\tau_{\mathrm{A}-}/\tau_{\mathrm{A}^{\mathrm{xx}}} = 3.1$ for $R = 1.39$ nm nanocrystals and 2.5 for $R = 1.92$ nm nanocrystals, both in a toluene dielectric.[41] Given literature $\tau_{\mathrm{A}^{\mathrm{xx}}}$ data, these computed ratios imply values of $\tau_{\mathrm{A}-} = 37$ ps and 81 ps, respectively, which represent a somewhat smaller size dependence ($p = 2.4$) than we observe experimentally ($p = 4.3$, Figure 5.3).

$$\frac{1}{t_{A^{XX}}} = \frac{2}{t_{A^-}} + \frac{2}{t_{A^+}} \tag{5.5}$$

Other systematic experimental measurements of the size dependence of trion Auger recombination rates do not exist. The strong trion-Auger size dependence observed here is consistent with previous reports of slow trion Auger recombination in colloidal core/thick-shell nanocrystals,[24,42,43] colloidal dot-in-rod nanocrystals,[44] and self-assembled quantum dots,[45] all possessing much greater internal volumes, but other factors including reduced electron-hole overlap and interface gradation are undoubtedly also important in these more-complex nanostructures. To our knowledge, the only analogous data are available from transient cathodoluminescence decay measurements on nanocrystal films of three CdSe/ZnS samples, and analysis involved deconvolution of overlapping luminescence from multiple species.[46] These data show a smaller size dependence of $\tau_{\mathrm{A}-}$ than observed here, corresponding to $p \sim 1.1$. The origin of this difference is unclear. We note that the simplicity of the photodoping and photoluminescence approach reported in the present study is favorable for allowing unambiguous identification and analysis of negative trions in colloidal CdSe nanocrystals.

If eqn 5.5 is valid, then positive trion Auger times (τ_A+) can also be predicted from the trion and biexciton Auger data, and this result is plotted in Figure 5.4 along with the other data. For all experimental radii investigated here, τ_A+ is predicted to be smaller than τ_A-, but it also shows a smaller size dependence (p = 2.5 from eqn 5.4) than either τ_A- or τ_A^{xx}. Both observations would be consistent with expectations from the greater density of states in the valence bands of II-VI semiconductors than in their conduction bands, assuming a greater density of states results in a lesser sensitivity to changes in the density of states.[1] Because of its strong size dependence, τ_A- may even become faster than τ_A+ at very small R, according to eqn 5.5. As stressed previously,[9] however, eqn 5.5 neglects four-particle processes in biexciton Auger recombination, in which the energy from the recombining exciton is partitioned between the electron and hole of the remaining exciton. Stable *p*-doped colloidal CdSe nanocrystals have not been prepared experimentally, and without independently measuring τ_A+, it is not possible to determine the validity of eqn 5.5. A value of τ_{A+} = 1.1 ns has been reported for CdSe/CdS nanocrystals (core R = 1.8 nm, core/shell R = 4 - 5 nm), however, measured by variable-repetition-rate photoluminescence spectroscopy,[47] and for the same nanocrystals, τ_A^{xx} = 0.40 ns and τ_A- = 2.3 ns were reported. Although a direct comparison of these data with those presented in Figure 5.4 is complicated by the influence of the thick CdS shells in the former, the data are consistent with eqn 5.5.

Finally, the data presented here also imply a strong size dependence of trion PL quantum yields. From analysis of experimental decay dynamics, R ~ 3 nm CdSe/CdS nanocrystals have been predicted to have negative trion PL quantum yields as large as 10 – 15%.[9] The data here support this proposal but also suggest that the maximum PL quantum yields of negative trions should decrease rapidly to < 1% at the smallest radii investigated here (R = 1.4), simply because of the strong size dependence of τ_{A^-}. The strong size dependence of τ_{A^-} may thus cause an order of magnitude variation in the brightness of "grey" states observed during nanocrystal intermittency, depending on nanocrystal radius. Awareness of this τ_{A^-} size dependence may therefore inform interpretations of the microscopic origins of these grey states.

5.4 Conclusion

In summary, the dependence of negative trion Auger recombination on nanocrystal radius has been measured for free-standing colloidal *n*-doped CdSe nanocrystals prepared photochemically. Negative trion Auger recombination accelerates rapidly with decreasing nanocrystal radius, with τ_{A^-} proportional to $R^{4.3}$. This scaling contrasts with the universal[21] R^3 scaling of bi- and multi-exciton Auger recombination, and it implies a weaker size dependence of Auger recombination in the as-yet inaccessible CdSe positive trion. These results provide an experimental basis for the development and testing of theoretical descriptions of trion Auger recombination dynamics in CdSe and related semiconductor nanocrystals. Beyond the specific CdSe results presented here, these findings demonstrate the utility of photodoping[26] as an approach for exploring the unique physical properties of high-quality electronically doped colloidal semiconductor nanocrystals.

5.5 Notes to Chapter 5

(1) Cohn, A. W.; Rinehart, J. D.; Schimpf, A. M.; Weaver, A. L.; Gamelin, D. R. *Nano Lett.* **2014**, *14*, 353
(2) Loss, D.; DiVincenzo, D. P. *Phys. Rev. A* **1998**, *57*, 120.
(3) Awschalom, D. D.; Bassett, L. C.; Dzurak, A. S.; Hu, E. L.; Petta, J. R. *Science* **2013**, *339*, 1174.
(4) Nozik, A. J.; Beard, M. C.; Luther, J. M.; Law, M.; Ellingson, R. J.; Johnson, J. C. *Chem. Rev.* **2010**, *110*, 6873.
(5) Mora-Seró, I.; Giménez, S.; Fabregat-Santiago, F.; Gómez, R.; Shen, Q.; Toyoda, T.; Bisquert, J. *Acct. Chem. Res.* **2009**, *42*, 1848.

(6) Landsberg, P. T. *Recombination in Semiconductors*; Cambridge University Press: Cambridge, 1991.

(7) Chepic, D. I.; Efros, A. L.; Ekimov, A. I.; Ivanov, M. G.; Kharchenko, V. A.; Kudriavtsev, I. A.; Yazeva, T. V. *J. Lumin.* **1990**, *47*, 113.

(8) Efros, A. L. In *Semiconductor Nanocrystals: from Basic Principles to Applications*; Efros, A. L., Lockwood, D. J., Tsybeskov, L., Eds.; Kluwer Academic: New York, 2003, p 52.

(9) Jha, P. P.; Guyot-Sionnest, P. *ACS Nano* **2009**, *3*, 1011.

(10) Zhao, J.; Nair, G.; Fisher, B. R.; Bawendi, M. G. *Phys. Rev. Lett.* **2010**, *104*, 157403.

(11) Rosen, S.; Schwartz, O.; Oron, D. *Phys. Rev. Lett.* **2010**, *104*, 157404.

(12) Califano, M. *J. Phys. Chem. C* **2011**, *115*, 18051.

(13) McGuire, J. A.; Sykora, M.; Joo, J.; Pietryga, J. M.; Klimov, V. I. *Nano Lett.* **2010**, *10*, 2049.

(14) Tyagi, P.; Kambhampati, P. *J. Chem. Phys.* **2011**, *134*, 094706.

(15) Bae, W. K.; Park, Y.-S.; Lim, J.; Lee, D.; Padilha, L. A.; McDaniel, H.; Robel, I.; Lee, C.; Pietryga, J. M.; Klimov, V. I. *Nature Comm.* **2013**, *4*, 2661.

(16) Shen, Y. C.; Mueller, G. O.; Watanabe, S.; Gardner, N. F.; Munkholm, A.; Krames, M. R. *Appl. Phys. Lett* **2007**, *91*, 141101.

(17) Song, N.; Zhu, H.; Jin, S.; Lian, T. *ACS Nano* **2011**, *5*, 8750.

(18) Qin, W.; Guyot-Sionnest, P. *ACS Nano* **2012**, *6*, 9125.

(19) Javaux, C.; Mahler, B.; Dubertret, B.; Shabaev, A.; Rodina, A. V.; Efros, A. L.; Yakovlev, D. R.; Liu, F.; Bayer, M.; Camps, G.; Biadala, L.; Buil, S.; Quelin, X.; Hermier, J.-P. *Nature Nanotechnology* **2013**, *8*, 206.

(20) Klimov, V. I. *J. Phys. Chem. B* **2006**, *110*, 16827.

(21) Robel, I.; Gresback, R.; Kortshagen, U.; Schaller, R. D.; Klimov, V. I. *Phys. Rev. Lett.* **2009**, *102*, 177404.

(22) Kobayashi, Y.; Nishimura, T.; Yamaguchi, H.; Tamai, N. *J. Phys. Chem. Lett.* **2011**, *2*, 1051.

(23) Klimov, V. I.; Mikhailovsky, A. A.; McBranch, D. W.; Leatherdale, C. A.; Bawendi, M. G. *Science* **2000**, *287*, 1011.

(24) Galland, C.; Ghosh, Y.; Steinbrück, A.; Hollingsworth, J. A.; Htoon, H.; Klimov, V. I. *Nature Commun.* **2012**, *3*, 908.

(25) Cragg, G. E.; Efros, A. L. *Nano Lett.* **2010**, *10*, 313.

(26) Rinehart, J. D.; Schimpf, A. M.; Weaver, A. L.; Cohn, A. W.; Gamelin, D. R. *J. Am. Chem. Soc.* **2013**, *135*, 18782

(27) Carbone, L.; Nobile, C.; De Giorgi, M.; Della Sala, F.; Morello, G.; Pompa, P.; Hytch, M.; Snoeck, E.; Fiore, A.; Franchini, I. R.; Nadasan, M.; Silvestre, A. F.; Chiodo, L.; Kudera, S.; Cingolani, R.; Krahne, R.; Manna, L. *Nano Lett.* **2007**, *7*, 2942.

(28) Chen, O.; Zhao, J.; Chauhan, V. P.; Cui, J.; Wong, C.; Harris, D. K.; Wei, H.; Han, H.-S.; Fukumura, D.; Jain, R. K.; Bawendi, M. G. *Nature Materials* **2013**, *12*, 445.

(29) Peng, X.; Qu, L. *J. Am. Chem. Soc.* **2002**, *124*, 2049.

(30) McLaurin, E. J.; Vlaskin, V. A.; Gamelin, D. R. *J. Am. Chem. Soc.* **2011**, *133*, 14978.

(31) Yu, W. W.; Qu, L.; Guo, W.; Peng, X. *Chem. Mater.* **2003**, *15*, 2854.

(32) Shim, M.; Guyot-Sionnest, P. *Nature* **2000**, *407*, 981.

(33) van Driel, A. F.; Allan, G.; Delerue, C.; Lodahl, P.; Vos, W. L.; Vanmaekelbergh, D. *Phys. Rev. Lett.* **2005**, *95*, 236804.

(34) Knowles, K. E.; McArthur, E. A.; Weiss, E. A. *ACS Nano* **2011**, *5*, 2026.

(35) Wang, H.; de Mello Donegá, C.; Meijerink, A.; Glasbeek, M. *J. Phys. Chem. B* **2006**, *110*, 733.

(36) Wang, C.; Wehrenberg, B. L.; Woo, C. Y.; Guyot-Sionnest, P. *J. Phys. Chem. B* **2004**, *108*, 9027.

(37) Cohn, A. W.; Schimpf, A. M.; Gunthardt, C. E.; Gamelin, D. R. *Nano Lett.* **2013**, *13*, 1810.

(38) Achermann, M.; Hollingsworth, J. A.; Klimov, V. I. *Phys. Rev. B* **2003**, *68*, 245302.

(39) Pandey, A.; Guyot-Sionnest, P. *J. Chem. Phys.* **2007**, *127*, 111104.

(40) Wang, L.-W.; Califano, M.; Zunger, A.; Franceschetti, A. *Phys. Rev. Lett.* **2003**, *91*, 056404.

(41) Califano, M. *ACS Nano* **2011**, *5*, 3614.

(42) Spinicelli, P.; Buil, S.; Quélin, X.; Mahler, B.; Dubertret, B.; Hermier, J.-P. *Phys. Rev. Lett.* **2009**, *102*, 136801.

(43) Wang, X.; Ren, X.; Kahen, K.; Hahn, M. A.; Rajeswaran, M.; Maccagnano-Zacher, S.; Silcox, J.; Cragg, G. E.; Efros, A. L.; Krauss, T. D. *Nature* **2009**, *459*, 686.

(44) Rabouw, F. T.; Lunnemann, P.; van Dijk-Moes, R. J. A.; Frimmer, M.; Pietra, F.; Koenderink, A. F.; Vanmaekelbergh, D. *Nano Lett.* **2013**, *13*, 4884.

(45) Patton, B.; Langbein, W.; Woggon, U. *Physical Review B* **2003**, *68*, 125316.

(46) Padilha, L. A.; Bae, W. K.; Klimov, V. I.; Pietryga, J. M.; Schaller, R. D. *Nano Lett.* **2013**, *13*, 925.

(47) Saba, M.; Aresti, M.; Quochi, F.; Marceddu, M.; Loi, M. A.; Huang, J.; Talapin, D. V.; Mura, A.; Bongiovanni, G. *ACS Nano* **2013**, *7*, 229.

Chapter 6: Summary and Outlook

The previous chapters addressed various aspects of the process of photodoping of semiconductor nanocrystals and examined some of the spectroscopic signatures that emerge as a result of adding charge carriers. This final chapter summarizes the conclusions of the previous chapters and suggests for investigations into the properties of photodoped nanocrystals.

6.1 Summary

Chapter 2 examined a series of Mg^{2+}:ZnO nanocrystals using various spectroscopies. Comparison of the shift in trap PL energy with the shift in band-gap absorption energy reveals a change in both the conduction-band and valence-band energies upon Mg^{2+} incorporation. This observation was confirmed by introducing Mn^{2+} dopants to observe shifts in the energy of the transition from Mn^{2+} to the conduction band by MCD. EPR of photodoped Mg^{2+}:ZnO also probed the effects of the Mg^{2+} dopants on the band gap energy of ZnO through changes in the electron g-value. Electron transfer between Mg^{2+}:ZnO nanocrystals and ZnO nanocrystals as monitored by EPR also confirmed the relative positions of the conduction-band energies and highlighted the use of Mg^{2+}:ZnO nanocrystals as tunable reducing agents.

Chapter 3 explored the photodoping process more closely, through study of the hole scavenging reaction between ZnO nanocrystals and ethanol (EtOH). Continuous wave and time resolved PL measurements of the prominent ZnO QD trap emission showed that the reaction between EtOH and ZnO QDs occurs within our instrument response function of 15 ps. This observation rationalizes the ability of ZnO QDs to accumulate more than one electron by the photodoping method despite the competing trion Auger recombination process. Additionally, chapter 3 introduced the trap-assisted Auger process as the mechanism for reversible trap PL quenching upon charging. The increase in band-gap PL intensity upon charging was rationalized as an increase in the exciton lifetime due to a decrease in nonradiative decay rates resulting from hole stabilization.

Chapter 4 examined the trap-assisted Auger process more closely by measuring the size dependence of the trap-assisted Auger rate. The size dependence was found to be smaller than any other reported Auger size dependence in nanocrystals. Possible reasons for the small size dependence were given, although ultimately the variation in Auger rates will be affected by the size dependence of many variables. Picosecond timescale transient absorption measurements showed the influence of trap-assisted Auger process on the dynamics of the band-edge absorption feature.

Chapter 5 took advantage of Li[Et_3BH] as a hole quencher to photodope and examine trion Auger recombination rates in CdSe nanocrystals. Previous work on trion recombination in CdSe QDs lacked a comprehensive size dependence of the negative trion Auger recombination rate. The size dependence of the negative trion Auger recombination rates was found to be greater than the R^3 dependence that was previously assumed based on CdSe biexciton Auger recombination rates. The negative trion Auger recombination rates found in these experiments were used to infer the Auger recombination rates of the positive trion. The quantum yield of charged CdSe of various sizes was also predicted based on the trion Auger recombination rates, which is important to understanding the role of trions in the grey states observed in single particle measurements.

6.2 Outlook

The experiments in chapter 5 took advantage of the ability to photodope colloidal CdSe nanocrystals to report the previously unknown size dependence of negative trion Auger recombination rates in CdSe QDs. As mentioned in Ref.1 the ability to reversibly make previously unattainable *n*-type colloidal QDs opens up many possibilities for future experiments. The interaction between electron and dopant spins in nanocrystals is of interest and photodoping has been a useful tool to probe these interactions in ZnO nanocrystals.[2] This is analogous to exciton magnetic polaron (EMP) formation in CdSe which is due to the exchange interactions of the dopant and the exciton.[3] Additional PL and EPR to probe extra charge carriers in magnetically doped chalcogenide nanocrystals will be a rich area of study.

Charging chalcogenide nanocrystals where fast energy transfer to the dopant is possible seems to be inaccessible by photodoping. Preliminary results show that energy transfer to Mn^{2+} in Mn^{2+}:CdS can out-compete hole scavenging by Li[Et_3BH] and these nanocrystals can-not be charged photochemically whereas undoped (i.e. no Mn^{2+}) CdS QDs can be photochemically charged. It was previously observed that when small charged ZnO are mixed with large uncharged ZnO in an anaerobic environment, electrons will transfer from the conduction band of small ZnO QDs to the conduction band of large ZnO QDs.[4] Preliminary results have also shown that electron transfer can occur from charged CdSe QDs to uncharged ZnO QDs. Using this motif, it should be possible to charge Mn^{2+}:CdS with smaller CdS QDs that contain excess electrons in the conduction and no Mn^{2+}. This system would then allow us to spectroscopically probe the charge transfer process while ensuring that the Mn^{2+}:CdS QDs could only be charged by electron transfer and not by photodoping. The progress of electron transfer could be probed by absorption, Mn^{2+} PL lifetimes, or EPR.

Alternatively, the themes of this thesis can be applied to another aspect of QD photophysics. As mentioned in chapter 1, a breakthrough in suppressing undesired Auger recombination came from a theory paper where it was suggested that alloying at the surface of QDs will slow Auger recombination.[5] It has since been experimentally verified that alloying does indeed suppress both biexciton and trion Auger processes. QD-LED devices made with alloyed quantum dots were shown to have better performance than those made with core/shell quantum dots of the same overall diameter.[6] A similar result should be found with trap-assisted Auger recombination. The Mg^{2+}:ZnO QD synthesis from chapter 2 should be straight forward to adapt to preferentially alloy Mg^{2+} at the surface of the QD instead of doping uniformly within the core, and the effect of alloying Mg^{2+} at the surface of ZnO QDs on the trap-assisted Auger rate can be quantified. ZnO trap emission has been identified as a possible phosphor for QD-LEDs.[7] Incorporating these alloyed dots into devices could lead to improved performance.

6.3 Notes to Chapter 6

(1) Rinehart, J. D.; Schimpf, A. M.; Weaver, A. L.; Cohn, A. W.; Gamelin, D. R. **2013**, submitted.
(2) Ochsenbein, S. T.; Feng, Y.; Whitaker, K. M.; Badaeva, E.; Liu, W. K.; Li, X.; Gamelin, D. R. *Nat. Nanotechnol.* **2009**, *4*, 681.
(3) Beaulac, R.; Archer, P. I.; Liu, X.; Lee, S.; Salley, G. M.; Dobrowolska, M.; Furdyna, J. K.; Gamelin, D. R. *Nano Lett.* **2008**, *8*, 1197.
(4) Hayoun, R.; Whitaker, K. M.; Gamelin, D. R.; Mayer, J. M. *J. Am. Chem. Soc.* **2011**, *133*, 4228.
(5) Cragg, G. E.; Efros, A. L. *Nano Lett.* **2010**, *10*, 313.
(6) Bae, W. K.; Park, Y.-S.; Lim, J.; Lee, D.; Padilha, L. A.; McDaniel, H.; Robel, I.; Lee, C.; Pietryga, J. M.; Klimov, V. I. *Nature Comm.* **2013**, *4*, 2661.
(7) Nannen, E.; Kummell, T.; Ebbers, A.; Bacher, G. *Appl. Phys. Express* **2012**, *5*, 035001.

BIBLIOGRAPHY

Achermann, M.; Hollingsworth, J. A.; Klimov, V. I. *Phys. Rev. B: Condens. Matter* **2003**, *68*, 245302.

Allen, J. W. *J. Phys. C. Solid State* **1986**, *19*, 6287-6295.

Anikeeva, P. O.; Madigan, C. F.; Halpert, J. E.; Bawendi, M. G.; Bulović, V. *Phys. Rev. B: Condens. Matter* **2008**, *78*.

Awschalom, D. D.; Bassett, L. C.; Dzurak, A. S.; Hu, E. L.; Petta, J. R. *Science* **2013**, *339*, 1174-1179.

Awschalom, D. D.; Flatte, M. E. *Nature* **2007**, *3*, 153 - 159.

Badaeva, E.; May, J. W.; Ma, J.; Gamelin, D. R.; Li, X. *J. Phys. Chem. C* **2011**, *115*, 20986–20991.

Bae, W. K.; Padilha, L. A.; Park, Y.-S.; McDaniel, H.; Robel, I.; Pietryga, J. M.; Klimov, V. I. *ACS Nano* **2013**, *7*, 3411-3419.

Bae, W. K.; Park, Y.-S.; Lim, J.; Lee, D.; Padilha, L. A.; McDaniel, H.; Robel, I.; Lee, C.; Pietryga, J. M.; Klimov, V. I. *Nature Comm.* **2013**, *4*, 2661.

Bahnemann, D. W.; Kormann, C.; Hoffmann, M. R. *J. Phys. Chem.* **1987**, *91*, 3789-3798.

Bohle, D. S.; Spina, C. J. *J. Am. Chem. Soc.* **2007**, *129*, 12380-12381.

Bohle, D. S.; Spina, C. J. *J. Am. Chem. Soc.* **2009**, *131*, 4397-4404.

Bowker, M.; Houghton, H.; Waugh, K. C. *J. Chem. Soc., Faraday Trans. 1* **1982**, *78*, 2573-2582.

Bullen, C.; Mulvaney, P. *Langmuir* **2006**, *22*, 3007-3013.

Buonsanti, R.; Llordes, A.; Aloni, S.; Helms, B. A.; Milliron, D. J. *Nano Lett.* **2011**, *11*, 4706-4710.

Caldas, M. J.; Fazzio, A.; Zunger, A. *App. Phys. Lett.* **1984**, *45*, 671-673.

Califano, M. *J. Phys. Chem. C* **2011**, *115*, 18051-18054.

Califano, M. *ACS Nano* **2011**, *5*, 3614.

Califano, M. *ACS Nano* **2011**, *5*, 3614-3621.

Carbone, L.; Nobile, C.; De Giorgi, M.; Della Sala, F.; Morello, G.; Pompa, P.; Hytch, M.; Snoeck, E.; Fiore, A.; Franchini, I. R.; Nadasan, M.; Silvestre, A. F.; Chiodo, L.; Kudera, S.; Cingolani, R.; Krahne, R.; Manna, L. *Nano Lett.* **2007**, *7*, 2942.

Chen, O.; Zhao, J.; Chauhan, V. P.; Cui, J.; Wong, C.; Harris, D. K.; Wei, H.; Han, H.-S.; Fukumura, D.; Jain, R. K.; Bawendi, M. G. *Nature Materials* **2013**, *12*, 445.

Chepic, D. I.; Efros, A. L.; Ekimov, A. I.; Ivanov, M. G.; Kharchenko, V. A.; Kudriavtsev, I. A.; Yazeva, T. V. *J. Lumin.* **1990**, *47*, 113-127.

Chiou, J. W.; Tsai, H. M.; Pao, C. W.; Krishna Kumar, K. P.; Ray, S. C.; Chien, F. Z.; Pong, W. F.; Tsai, M.-H.; Chen, C.-H.; Lin, H.-J.; Wu, J. J.; Yang, M.-H.; Liu, S. C.; Chiang, H. H.; Chen, C. W. *Appl. Phys. Lett.* **2006**, *89*, 043121.

Climente, J. I.; Bertoni, A.; Goldoni, G. *Phys. Rev. B* **2008**, *78*, 155316.

Climente, J. I.; Movilla, J. L.; Planelles, J. *Small* **2012**, *8*, 754-759.

Cohn, A.; Janßen, N.; Mayer, J. M.; Gamelin, D. R. *J. Phys. Chem. C* **2012**, *116*, 20633–20642.

Cohn, A. W.; Janssen, N.; Mayer, J. M.; Gamelin, D. R. *J. Phys. Chem. C.* **2012**, *116*, 20633-20642.

Cohn, A. W.; Kittilstved, K. R.; Gamelin, D. R. *J. Am. Chem. Soc.* **2012**, *134*, 7937-7943.

Cohn, A. W.; Rinehart, J. D.; Schimpf, A. M.; Weaver, A. L. **2013**, submitted.

Cohn, A. W.; Rinehart, J. D.; Schimpf, A. M.; Weaver, A. L.; Gamelin, D. R. *Nano Lett.* **2013**, *ASAP*, DOI: 10.1021/nl4041675.

Cohn, A. W.; Schimpf, A. M.; Gunthardt, C. E.; Gamelin, D. R. *Nano Lett.* **2013**, *13*, 1810-1815.

Cragg, G. E.; Efros, A. L. *Nano Lett.* **2010**, *10*, 313-317.

Cunningham, J.; Hodnett, B. K. *J. Chem. Soc., Faraday Trans. 1* **1981**, *77*, 2777-2801.

Dang, C.; Lee, J.; Breen, C.; Steckel, J. S.; Coe-Sullivan, S.; Nurmikko, A. *Nature Nanotech.* **2012**, *7*, 335-339.

De Trizio, L.; Buonsanti, R.; Schimpf, A. M.; Llordes, A.; Gamelin, D. R.; Simonutti, R.; Milliron, D. J. *Chem. Mater.* **2013**, *25*, 3383-3390.

Dietl, T. *Phys. Rev. B* **2008**, *77*, 085208.

Ding, R.; Xu, C.; Gu, B.; Shi, Z.; Wang, H.; Ba, L.; Xiao, Z. *J. Mater. Sci. Technol.* **2010**, *26*, 601.

Efros, A. L. (2003). Auger Processes in Nanosize Semiconductor Crystals. Semiconductor Nanocrystals: from Basic Principles to Applications. A. L. Efros, D. J. Lockwood and L. Tsybeskov. New York, Kluwer Academic**:** 52-72.

Fathpour, S.; Mi, Z.; Bhattacharya, P.; Kovsh, A. R.; Mikhrin, S. S.; Krestnikov, I. L.; Kozhukhov, A. V.; Ledentsov, N. N. *Appl. Phys. Lett.* **2004**, *85*, 5164.

Feng, Y.; Badaeva, E.; Gamelin, D. R.; Li, X. *J. Phys. Chem. Lett.* **2010**, *1*, 1927–1931.

Galland, C.; Ghosh, Y.; Steinbrück, A.; Hollingsworth, J. A.; Htoon, H.; Klimov, V. I. *Nature Commun.* **2012**, *3*, 908.

Gamelin, D. R.; Güdel, H. U. *Top. Curr. Chem.* **2000**, *214*, 1-56.

Germeau, A.; Roest, A. L.; Vanmaekelbergh, D.; Allan, G.; Delerue, C.; Meulenkamp, E. A. *Phys. Rev. Lett.* **2003**, *90*, 097401.

Gimenez, A. J.; Yáñez-Limón, J. M.; Seminario, J. M. *J. Phys. Chem. C.* **2010**, *115*, 282-287.

Gruber, T.; Krichner, C.; Kling, R.; Reuss, F.; Waag, A. *Appl. Phys. Lett.* **2004**, *84*, 5359.

Guyot-Sionnest, P. *Microchim Acta* **2008**, *160*, 309-314.

Haase, M.; Weller, H.; Henglein, A. *J. Phys. Chem.* **1988**, *92*, 482-487.

Haug, A. *J. Phys. Chem. Solids* **1988**, *49*, 599-605.

Hayoun, R.; Whitaker, K. M.; Gamelin, D. R.; Mayer, J. M. *J. Am. Chem. Soc.* **2011**, *133*, 4228–4231.

Heitsch, S.; Zimmerman, G.; Fritsch, D.; Sturm, C.; Schmidt-Grund, R.; Schulz, C.; Hochmuth, H.; Spermann, D.; Benndorf, G.; Rheinländer, B.; Nobis, T.; Lorenz, M.; Grundmann, M. *J. Appl. Phys.* **2007**, *101*, 083521.

Hoyer, P.; Weller, H. *Chem. Phys. Letters* **1994**, *221*, 379-384.

Hoyer, P.; Weller, H. *J. Phys. Chem.* **1995**, *99*, 14096-14100.

Hsu, N. E.; Hun, W. K.; F., C. Y. *J. Appl. Phys.* **2004**, *96*, 4671.

Javaux, C.; Mahler, B.; Dubertret, B.; Shabaev, A.; Rodina, A. V.; Efros, A. L.; Yakovlev, D. R.; Liu, F.; Bayer, M.; Camps, G.; Biadala, L.; Buil, S.; Quelin, X.; Hermier, J.-P. *Nature Nanotech.* **2013**, *8*, 206-212.

Jha, P., P.; Guyot-Sionnest, P. *ACS Nano* **2009**, *3*, 1011.

Jha, P. P.; Guyot-Sionnest, P. *ACS Nano* **2009**, *3*, 1011-1015.

Johnson, C. A.; Cohn, A.; Kaspar, T. C.; Chambers, S. A.; Salley, G. M.; Gamelin, D. R. *Phys. Rev. B: Condens. Matter* **2011**, *84*, 125203.

Johnson, C. A.; Kittilstved, K. R.; Kaspar, T. C.; Droubay, T. C.; Chambers, S. A.; Salley, G. M.; Gamelin, D. R. *Phys. Rev. B: Condens. Matter* **2010**, *82*, 115202.

Kamat, P. V.; Huehn, R.; Nicolaescu, R. *J. Phys. Chem. B* **2002**, *106*, 788-794.

Kamat, P. V.; Patrick, B. *J. Phys. Chem.* **1992**, *96*, 6829-6834.

Kambhampati, P. *J. Phys. Chem. Lett.* **2012**, *3*, 1182-1190.

Kittilstved, K. R.; Liu, W. K.; Gamelin, D. R. *Nature Materials* **2006**, *5*, 291-297.

Klimov, V. I. *Appl. Phys. Lett.* **2006**, *89*, 123118.

Klimov, V. I. *J. Phys. Chem. B* **2006**, *110*, 16827-16845.

Klimov, V. I.; Ivanov, S. A.; Nanda, J.; Achermann, M.; Bezel, I.; McGuire, J. A.; Piryatinski, A. *Nature* **2007**, *447*, 441-446.

Klimov, V. I.; Mikhailovsky, A. A.; McBranch, D. W.; Leatherdale, C. A.; Bawendi, M. G. *Science* **2000**, *287*, 1011-1013.

Knowles, K. E.; McArthur, E. A.; Weiss, E. A. *ACS Nano* **2011**, *5*, 2026-2035.

Kobayashi, Y.; Nishimura, T.; Yamaguchi, H.; Tamai, N. *J. Phys. Chem. Lett.* **2011**, *2*, 1051-1055.

Kobayashi, Y.; Tamai, N. *J. Phys. Chem. C.* **2010**, *114*, 17550-17556.

Koch, U.; Fojtik, A.; Weller, H.; Henglein, A. *Chem. Phys. Lett.* **1985**, *122*, 507.

Koch, U.; Fojtik, A.; Weller, H.; Henglein, A. *Chem. Phys. Lett.* **1985**, *122*, 507-510.

Koh, W.-k.; Koposov, A. Y.; Stewart, J. T.; Pal, B. N.; Robel, I.; Pietryga, J. M.; Klimov, V. I. *Scientific Reports* **2013**, *3*, 2004.

Kwak, G.; Yong, K. *J. Phys. Chem. C* **2008**, *112*, 3036-3041.

Landsberg, P. T. *Appl. Phys. Lett.* **1987**, *50*, 745-747.

Landsberg, P. T. (1991). Recombination in Semiconductors. Cambridge, Cambridge University Press.

Landsberg, P. T.; Rhys-Roberts, C.; Lal, P. *Proc. Phys. Soc.* **1964**, *84*, 915-931.

Lange, M.; Dietrich, C. P.; Zuniga-Perez, J.; von Wenckstern, H.; Lorenz, M.; Grundmann, M. *J. Vac. Sci. Technol., A* **2011**, *29*, 03A104.

Langer, J. M.; Delerue, C.; Lannoo, M.; Heinrich, H. *Phys. Rev. B* **1988**, *38*, 7723-7739.

Leiter, F. H.; Alves, H. R.; Hofstaetter, A.; Hofmann, D. M.; Meyer, B. K. *Physica Status Solidi B* **2001**, *226*, R4-R5.

Liu, W. K.; Whitaker, K. M.; Kittilstved, K. R.; Gamelin, D. R. *J. Am. Chem. Soc.* **2006**, *128*, 3910-3911.

Liu, W. K.; Whitaker, K. M.; Smith, A. L.; Kittilstved, K. R.; Robinson, B. H.; Gamelin, D. R. *Phys. Rev. Lett.* **2007**, *98*, 186804.

Lommens, P.; Lambert, K.; Loncke, F.; Muynck, D. D.; Balkan, T.; Vanhaecke, F.; Vrielinck, H.; Callens, F.; Hens, Z. *Chem. Phys. Chem.* **2008**, *9*, 484–491.

Loss, D.; DiVincenzo, D. P. *Phys. Rev. A* **1998**, *57*, 120-126.

Luther, J. M.; Jain, P. K.; Ewers, T.; Alivisatos, A. P. *Nat. Matter.* **2011**, *10*, 361-366.

Markham, M. C.; Hannan, M. C.; Paternostro, R.; Rose, C. B. *J. Am. Chem. Soc.* **1958**, *80*, 5394–5397.

Matsumoto, T.; Kato, H.; Miyamoto, K.; Sano, M.; Zhukov, E. A.; Yao, T. *Appl. Phys. Lett.* **2002**, *81*, 1231-1233.

McGuire, J. A.; Sykora, M.; Joo, J.; Pietryga, J. M.; Klimov, V. I. *Nano Lett.* **2010**, *10*, 2049-2057.

McLaurin, E. J.; Vlaskin, V. A.; Gamelin, D. R. *J. Am. Chem. Soc.* **2011**, *133*, 14978.

Meulenkamp, E. A. *J. Phys. Chem. B* **1998**, *102*, 5566-5572.

Minemoto, T.; Negami, T.; Nishiwaki, S.; Takakura, H.; Hamakawa, Y. *Thin Solid Films* **2000**, *372*, 173.

Mohamed, H. H.; Mendive, C. B.; Dillert, R.; Bahnemann, D. W. *J. Phys. Chem. A* **2011**, *114*, 2139.

Mora-Seró, I.; Giménez, S.; Fabregat-Santiago, F.; Gómez, R.; Shen, Q.; Toyoda, T.; Bisquert, J. *Acct. Chem. Res.* **2009**, *42*, 1848-1857.

Munro, A. M.; Ginger, D. S. *Nano Lett.* **2008**, *8*, 2585-2590.

Nagao, M.; Morimoto, T. *J. Phys. Chem.* **1980**, *84*, 2054-2058.

Nanda, J.; Ivanov, S. A.; Htoon, H.; Bezel, I.; Piryatinski, A.; Tretiak, S.; Klimov, V. I. *J. Appl. Phys.* **2006**, *99*, 034309.

Nannen, E.; Kummell, T.; Ebbers, A.; Bacher, G. *Appl. Phys. Express* **2012**, *5*, 035001.

Norberg, N. S.; Dalpian, G. M.; Chelikowsky, J. R.; Gamelin, D. R. *Nano Lett.* **2006**, *6*, 2887-2892.

Norberg, N. S.; Gamelin, D. R. *J. Phys. Chem. B* **2005**, *109*, 20810-20816.

Norberg, N. S.; Kittilstved, K. R.; Amonette, J. E.; Kukkadapu, R. K.; Schwartz, D. A.; Gamelin, D. R. *J. Am. Chem. Soc.* **2004**, *126*, 9387-9398.

Nozik, A. J.; Beard, M. C.; Luther, J. M.; Law, M.; Ellingson, R. J.; Johnson, J. C. *Chem. Rev.* **2010**, *110*, 6873-6890.

Ochsenbein, S. T.; Feng, Y.; Whitaker, K. M.; Badaeva, E.; Liu, W. K.; Li, X.; Gamelin, D. R. *Nature Nanotech.* **2009**, *4*, 681–687.

Ohtomo, A.; Kawasaki, M.; Koida, T.; Masubuchi, K.; Koinuma, H.; Sakurai, Y.; Yoshida, Y.; Yasuda, T.; Segawa, Y. *Appl. Phys. Lett.* **1998**, *72*, 2466.

Olson, D. C.; Shaheen, S. E.; White, M. S.; Mitchell, W. J.; van Hest, M. F. A. M.; Collins, R. T.; Ginley, D. S. *Adv. Funct. Mater.* **2007**, *17*, 264.

Orlinskii, S. B.; Schmidt, J.; Baranov, P. G.; Hofmann, D. M.; de Mello Donegá, C.; Meijerink, A. *Phys. Rev. Lett.* **2004**, *92*, 047603.

Orlinskii, S. B.; Schmidt, J.; Baranov, P. G.; Lorrmann, V.; Riedel, I.; Rauh, D.; Dyakonov, V. *Phys. Rev. B* **2008**, *77*, 115334.

Orlinskii, S. B.; Schmidt, J.; Groenen, E. J. J.; Baranov, P. G.; de Mello Donegá, C.; Meijerink, A. *Phys. Rev. Lett.* **2005**, *94*, 097602.

Oron, D.; Kazes, M.; Banin, U. *Phys. Rev. B* **2007**, *75*, 035330.

Padilha, L. A.; Bae, W. K.; Klimov, V. I.; Pietryga, J. M.; Schaller, R. D. *Nano Lett.* **2013**, *13*, 925-932.

Pandey, A.; Guyot-Sionnest, P. *J. Chem. Phys.* **2007**, *127*, 111104.

Park, W. I.; Yi, G.-C.; Kim, M. Y.; Pennycook, S. J. *Adv. Mater.* **2003**, *15*, 526.

Patton, B.; Langbein, W.; Woggon, U. *Physical Review B* **2003**, *68*, 125316.

Peng, B.; Liang, W.; White, M. A.; Gamelin, D. R.; Li, X. *J. Phys. Chem. C* **2012**, *116*, 11223-11231.

Peng, X.; Qu, L. *J. Am. Chem. Soc.* **2002**, *124*, 2049.

Pollnau, M.; Gamelin, D. R.; Lüthi, S. R.; Güdel, H. U.; Hehlen, M. P. *Phys. Rev. B* **2000**, *61*, 3337-3346.

Qin, W.; Guyot-Sionnest, P. *ACS Nano* **2012**, *6*, 9125–9132.

Qui, X.; Li, L.; Zheng, J.; Liu, J.; Sun, X.; Li, G. *J. Phys. Chem. C.* **2008**, *112*, 12242.

Rabani, J.; Behar, D. *J. Phys. Chem.* **1989**, *93*, 2559-2563.

Rabouw, F. T.; Lunnemann, P.; van Dijk-Moes, R. J. A.; Frimmer, M.; Pietra, F.; Koenderink, A. F.; Vanmaekelbergh, D. *Nano Lett.* **2013**, *13*, 4884-4892.

Ramakrishna, G.; Ghosh, H. N. *Langmuir* **2003**, *19*, 3006-3012.

Rinehart, J. D.; Schimpf, A. M.; Weaver, A. L.; Cohn, A. W.; Gamelin, D. R. *J. Am. Chem. Soc.* **2013**, *135*, 18782 - 18785.

Robbins, D. J. *J. Phys. C. Solid State* **1983**, *16*, 3825-3840.

Robel, I.; Gresback, R.; Kortshagen, U.; Schaller, R. D.; Klimov, V. I. *Phys. Rev. Lett.* **2009**, *102*, 177404.

Roest, A. L.; Germeau, A.; Kelly, J. J.; Vanmaekelbergh, D.; Allan, G.; Meulenkamp, E. A. *Chem. Phys. Chem.* **2003**, *4*, 959-966.

Roest, A. L.; Houtepen, A. J.; Kelly, J. J.; Vanmaekelbergh, D. *Faraday Discuss.* **2004**, *125*, 55–62.

Roest, A. L.; Kelly, J. J.; Vanmaekelbergh, D. *Appl. Phys. Lett* **2003**, *83*, 5530-5532.

Roest, A. L.; Kelly, J. J.; Vanmaekelbergh, D.; Meulenkamp, E. A. *Phys. Rev. Lett.* **2002**, *89*, 036801.

Rosen, S.; Schwartz, O.; Oron, D. *Phys. Rev. Lett.* **2010**, *104*, 157404.

Saba, M.; Aresti, M.; Quochi, F.; Marceddu, M.; Loi, M. A.; Huang, J.; Talapin, D. V.; Mura, A.; Bongiovanni, G. *ACS Nano* **2013**, *7*, 229-238.

Schimpf, A. M.; Gunthardt, C., E.; Rinehart, J. D.; Mayer, J. M.; Gamelin, D. R. *J. Am. Chem. Soc.* **2013**, *135*, 16569-16577.

Schimpf, A. M.; Ochsenbein, S. T.; Buonsanti, R.; Milliron, D. J.; Gamelin, D. R. *Chem. Commun.* **2012**, *48*, 9352-9354.

Schrauben, J. N.; Hayoun, R.; Valdez, C. N.; Braten, M.; Fridley, L.; Mayer, J. M. *Science* **2012**, *336*, 1298-1301.

Schwartz, D. A.; Norberg, N. S.; Nguyen, Q. P.; Parker, J. M.; Gamelin, D. R. *J. Am. Chem. Soc.* **2003**, *125*, 13205-13218.

Semonin, O. E.; Luther, J. M.; Choi, S.; Chen, H.-Y.; Gao, J.; Nozik, A. J.; Beard, M. C. *Science* **2011**, *334*, 1530-1533.

Shan, F. K.; Kim, B. I.; Liu, G. X.; Liu, Z. F.; Sohn, J. Y.; Lee, W. J.; Shin, B. C.; Yu, Y. S. *J. Appl. Phys.* **2004**, *95*, 4772.

Shannon, R. D. *Acta Crystallogr. Sect. A: Found. Crystallogr.* **1976**, *32*, 751-767.

Shen, Y. C.; Mueller, G. O.; Watanabe, S.; Gardner, N. F.; Munkholm, A.; Krames, M. R. *Appl. Phys. Lett* **2007**, *91*, 141101-141103.

Shim, M.; Guyot-Sionnest, P. *Nature* **2000**, *407*, 981 - 983.

Shim, M.; Guyot-Sionnest, P. *J. Am. Chem. Soc.* **2001**, *123*, 11651-11654.

Shim, M.; Guyot-Sionnest, P. *Phys. Rev. Lett.* **2003**, *91*, 169703.

Shim, M.; Wang, C. J.; Guyot-Sionnest, P. *J. Phys. Chem. B* **2001**, *105*, 2369.

Sokolov, V. I.; Druzhinin, A. V.; Gruzdev, N. B.; Dejneka, A.; Churpita, O.; Hubicka, Z.; Jastrabik, L.; Trepakov, V. *Phys. Rev. B* **2010**, *81*, 153104.

Song, N.; Zhu, H.; Jin, S.; Lian, T. *ACS Nano* **2011**, *5*, 8750-8759.

Spinicelli, P.; Buil, S.; Quélin, X.; Mahler, B.; Dubertret, B.; Hermier, J.-P. *Phys. Rev. Lett.* **2009**, *102*, 136801.

Stroyuk, O. L.; Dzhagan, V. M.; Shvalagin, V. V.; Kuchmiy, S. Y. *J. Phys. Chem. C* **2010**, *114*, 220-225.

Su, S. C.; Lu, Y. M.; Zhang, Z. Z.; Shan, C. X.; Li, B. H.; Shen, D. Z.; Yao, B.; Zhang, J. Y.; X., Z. D.; Fan, X. W. *Appl. Phys. Lett.* **2008**, *93*, 082108.

Subramanian, V.; Wolf, E. E.; Kamat, P. V. *J. Phys. Chem. B* **2003**, *107*, 7479-7485.

Subramanian, V. W., E. E.; Kamat, P. V. *J. Phys. Chem. B* **2003**, *107*, 7479-7485.

Thu, T. V.; Maenosono, S. *J. Appl. Phys.* **2010**, *107*, 014308.

Tyagi, P.; Kambhampati, P. *J. Chem. Phys.* **2011**, *134*, 094706-094710.

Valdez, C. N.; Braten, M.; Soria, A.; Gamelin, D. R.; Mayer, J. M. *J. Am. Chem. Soc.* **2013**, *135*, 8492-8495.

van Dijken, A.; Makkinje, J.; Meijerink, A. *J. Lumin.* **2001**, *92*, 323-328.

van Dijken, A.; Meulenkamp, E. A.; Vanmaekelbergh, D.; Meijerink, A. *J. Lumin.* **2000**, *90*, 123-128.

van Dijken, A.; Meulenkamp, E. A.; Vanmaekelbergh, D.; Meijerink, A. *J. Phys. Chem. B* **2000**, *104*, 4355-4360.

van Dijken, A.; Meulenkamp, E. A.; Vanmaekelbergh, D.; Meijerink, A. *J. Phys. Chem. B* **2000**, *104*, 1715-1723.

van Dijken, A.; Mulenkamp, E. A.; Vanmaekelbergh, D.; Meijerink, A. *J. Phys. Chem. B* **2000**, *104*.

van Driel, A. F.; Allan, G.; Delerue, C.; Lodahl, P.; Vos, W. L.; Vanmaekelbergh, D. *Phys. Rev. Lett.* **2005**, *95*, 236804.

Vanheusden, K.; Warren, W. L.; Seager, C. H.; Tallant, D. R.; Voigt, J. A.; Gnade, B. E. *J. Appl. Phys.* **1996**, *79*, 7983-7990.

Vohs, J. M.; Barteau, M. A. *Surf. Sci.* **1989**, *221*, 590-608.

Wang, C.; Shim, M.; Guyot-Sionnest, P. *Science* **2001**, *291*, 2390-2392.

Wang, C.; Wehrenberg, B. L.; Woo, C. Y.; Guyot-Sionnest, P. *J. Phys. Chem. B* **2004**, *108*, 9027-9031.

Wang, H.; de Mello Donegá, C.; Meijerink, A.; Glasbeek, M. *J. Phys. Chem. B* **2006**, *110*, 733-737.

Wang, L.-W.; Califano, M.; Zunger, A.; Franceschetti, A. *Phys. Rev. Lett.* **2003**, *91*, 056404.

Wang, T.; Radovanovic, P. V. *J. Phys. Chem. C.* **2011**, *115*, 406-413.

Wang, X.; Ren, X.; Kahen, K.; Hahn, M. A.; Rajeswaran, M.; Maccagnano-Zacher, S.; Silcox, J.; Cragg, G. E.; Efros, A. L.; Krauss, T. D. *Nature* **2009**, *459*, 686-689.

Wang, Y. S.; Thomas, P. J.; O'Brien, P. *J. Phys. Chem. B* **2006**, *110*, 21412.

Wassner, T. A.; Laumer, B.; Althammer, M.; Goennenwein, S. T. B.; Stutzmann, M.; Eickhoff, M.; Brandt, M. S. *Appl. Phys. Lett.* **2010**, *97*, 092102.

Wehrenberg, B. L.; Guyot-Sionnest, P. *J. Am. Chem. Soc.* **2003**, *125*, 7806-7807.

West, A. R. (1992). Solid State Chemistry and Its Applications. New York, John Wiley and Sons.

Whitaker, K. M.; Ochsenbein, S. T.; Polinger, V. Z.; Gamelin, D. R. *J. Phys. Chem. C* **2008**, *112*, 14331-14335.

Whitaker, K. M.; Ochsenbein, S. T.; Smith, A. L.; Echodu, D. C.; Robinson, B. H.; Gamelin, D. R. *J. Phys. Chem. C* **2010**, *114*, 14467–14472.

White, M. A. (2012). Electronic Strucuture and Auger Interactions in Semiconductor Nanocrystals. Ph.D Ph.D Thesis, University of Washington.

White, M. A.; Weaver, A. L.; Beaulac, R.; Gamelin, D. R. *ACS Nano* **2011**, *5*, 4158–4168.

Willander, M.; Nur, O.; Bano, N.; Sultana, K. *New J. Phys.* **2009**, *11*, 125020.

Wood, A.; Giersig, M.; Hilgendorff, M.; Vilas-Campos, A.; Liz-Marzán, L. M.; Mulvaney, P. *Aust. J. Chem.* **2003**, *56*, 1051-1057.

Wood, A.; Giersig, M.; Mulvaney, P. *J. Phys. Chem. B* **2001**, *105*, 8810-8815.

Wood, A.; Giersig, M.; Mulvaney, P. *J. Phys. Chem. B* **2001**, *105*, 8810-8815.

Xu, J.; Han, J.; Zhang, Y.; Sun, Y.; Xie, B. *Sens. Act. B* **2008**, *132*, 334-339.

Yamamoto, S. *J. Phys. Chem. C* **2011**, *115*, 21635-21640.

Yamamoto, S. *J. Appl. Phys.* **2012**, *111*, 094310.

Yamamoto, S.; Mishina, T. *J. Lumin.* **2011**, *131*, 620-XX.

Yang, Y.; Jin, Y.; He, H.; Wang, Q.; Tu, Y.; Lu, H.; Ye, Z. *J. Am. Chem. Soc.* **2010**, *132*, 13381-13394.

Yu, D.; Wang, C.; Guyot-Sionnest, P. *Science* **2003**, *300*, 1277-1280.

Yu, P.; Tang, Z. K.; Wong, G. K. L.; Kawasaki, M.; Ohtomo, A.; Koinuma, H.; Segawa, Y. *Solid State Commun.* **1997**, *103*, 459.

Yu, W. W.; Qu, L.; Guo, W.; Peng, X. *Chem. Mater.* **2003**, *15*, 2854.

Yue, Q.; Cheng, J.; Li, G.; Zhang, K.; Zhai, Y.; Wang, L.; Liu, J. *Journal of Fluorescence* **2011**, *21*, 1131-1135.

Zhang, M.; Bhattacharya, P.; Singh, J.; Hinckley, J. *Appl. Phys. Lett.* **2009**, *95*, 201108.

Zhang, X. D.; Guo, M. L.; Liu, C. L.; Zhang, L. A.; Zhang, W. Y.; Ding, Y. Q.; Wu, Q.; Feng, X. *European Physical Journal B* **2008**, *62*, 417.

Zhao, J.; Nair, G.; Fisher, B. R.; Bawendi, M. G. *Phys. Rev. Lett.* **2010**, *104*, 157403.

Zhou, H.; Alves, H.; Hofmann, D. M.; Kriegseis, W.; Meyer, B. K.; Kaczmarczyk, G.; Hoffmann, A. *App. Phys. Lett.* **2002**, *80*, 210-212.

Zippel, J.; Heitsch, S.; Stölzel, M.; Müller, A.; von Weckstern, H.; Benndorf, G.; Lorenz, M.; Hochmuth, H.; Grundmann, M. *J. Lumin.* **2010**, *130*, 520.